

2011

# Multiwavelength Studies of gamma-ray Binaries

Christina Aragona  
*Lehigh University*

Follow this and additional works at: <http://preserve.lehigh.edu/etd>

---

## Recommended Citation

Aragona, Christina, "Multiwavelength Studies of gamma-ray Binaries" (2011). *Theses and Dissertations*. Paper 1262.

This Dissertation is brought to you for free and open access by Lehigh Preserve. It has been accepted for inclusion in Theses and Dissertations by an authorized administrator of Lehigh Preserve. For more information, please contact [preserve@lehigh.edu](mailto:preserve@lehigh.edu).

# Multiwavelength Studies of $\gamma$ -ray Binaries

by

Christina Aragona

A Dissertation  
Presented to the Graduate Committee  
of Lehigh University  
in Candidacy for the Degree of  
Doctor of Philosophy  
in  
Physics

Lehigh University  
September 2011

Copyright  
Christina Aragona

Approved and recommended for acceptance as a dissertation in partial fulfillment of the requirements for the degree of Doctor of Philosophy.

Christina Aragona  
Multiwavelength Studies of  $\gamma$ -ray Binaries

---

**Date**

---

**Prof. M. Virginia McSwain**, Dissertation Director, Chair  
**(Must Sign with Blue Ink)**

---

**Accepted Date**

Committee Members

---

**Prof. George McCluskey**

---

**Prof. John Huennekens**

---

**Prof. Peet Hickman**

---

**Prof. Steve Goldman**

## Acknowledgments

I would like to thank my dissertation advisor Dr. Ginny McSwain for encouraging me to pursue my research interests, take advantage of opportunities for collaboration, propose new projects of my own design, and present my work to the astronomy community at large. She has pushed me to undertake challenges that I would have been too timid to seek on my own and these risks have helped me mature as a scientist. I would also like to thank my committee members: Dr. George McCluskey, Dr. John Huennekens, Dr. A. Peet Hickman, and Dr. Steve Goldman.

Dr. Mallory Roberts was an invaluable resource in pursuing the radio analysis of LS 5039. I would like to thank him for providing me with the raw radio observations, teaching me the data reduction techniques, and helping me formulate an approach for analyzing the source of the radio emission. I would also like to thank Dr. Michaël De Becker for providing échelle spectra of HD 259440 and collaborating on the paper constraining the orbital parameters of that system.

I am grateful to my groupmates Amber Marsh and Rachael Roettenbacher for their support on observing runs, in classes, and tackling research problems. I also owe thanks to Dr. Erika Grundstrom and Dr. Tabitha Boyajian for their help on the Kitt Peak Coudé Feed observing run in 2008.

This dissertation would not have been possible without the various telescope facilities and online databases which provided data for my projects. These include the staff of the Cerro Tololo Inter-American Observatory (CTIO), the Southern Astrophysical Research (SOAR) telescope, and the Kitt Peak National Observatory (KPNO), for their help in planning and executing observing runs. The Australia Telescope Compact Array (ATCA) is funded by the Commonwealth of Australia for operation as a National Facility managed by CSIRO. This research has made use of the SIMBAD database and the VizieR catalogue access tool, operated at CDS, Strasbourg, France.

I also appreciate the financial support provided to me by Lehigh University, the GAANN program, and NASA, without which this work would not have been possible.

Finally, I would like to thank my family for always encouraging and supporting my interest in science, especially my parents, David and Netta Aragona. They introduced me to

astronomy as a child, gave me my first telescope, encouraged me to start an astronomy club at my high school, and attended local research talks by astronomers with me in college. In graduate school, they always showed an interest in my research and encouraged me to keep going even when I felt overwhelmed and ready to give up. I could not have made it through the physics PhD program without the support of my friends and fellow graduate students at Lehigh. I would like to extend a special thanks to Amber Marsh, Ruthie Malenda, Laura Kelly and Massooma Pirbhai. They always had a ready ear to discuss research pitfalls, career questions, provide moral support, or simply have a bit of fun when I needed to decompress.

# Contents

<b>Acknowledgements</b>	<b>iv</b>
<b>List of Tables</b>	<b>viii</b>
<b>List of Figures</b>	<b>ix</b>
<b>Abbreviations</b>	<b>xv</b>
<b>Abstract</b>	<b>1</b>
<b>1 Introduction</b>	<b>3</b>
1.1 Massive Stars . . . . .	4
1.2 Compact Objects: Neutron Stars and Black Holes . . . . .	6
1.3 High Mass X-ray Binaries and $\gamma$ -ray Binaries . . . . .	8
1.4 Radiation Sources in $\gamma$ -ray Binaries . . . . .	12
1.4.1 High Energy Continuum Processes . . . . .	13
1.4.2 The Stellar Spectral Energy Distribution . . . . .	16
1.4.3 Spectral Lines: Bound-Bound Transitions . . . . .	18
<b>2 Observations</b>	<b>22</b>
2.1 Introduction . . . . .	22
2.2 Optical Spectroscopy . . . . .	23
2.3 Radio Observations . . . . .	28
2.4 Observations of $\gamma$ -ray binaries . . . . .	32

<b>3</b>	<b>HD 259440: The Proposed Optical Counterpart of HESS J0632+057</b>	<b>34</b>
3.1	Introduction . . . . .	34
3.2	Constraints on the Orbital Period of HD 259440 . . . . .	36
3.3	Stellar Parameters of HD 259440 . . . . .	39
3.4	Spectral Energy Distribution of HD 259440 . . . . .	48
<b>4</b>	<b>Optical Spectroscopic Studies of LS 5039</b>	<b>51</b>
4.1	Introduction . . . . .	51
4.2	Calculating the Orbital Parameters of LS 5039 . . . . .	52
4.3	Probing the Structure of the O Star Wind . . . . .	59
<b>5</b>	<b>LS 5039 at Radio Wavelengths</b>	<b>64</b>
5.1	Radio Emission from the Stellar Wind of LS 5039 . . . . .	64
5.2	The Colliding Wind Scenario in LS 5039 . . . . .	70
5.2.1	Orbital Geometry . . . . .	72
5.2.2	The Stagnation Point of the Shock Front . . . . .	74
5.2.3	Estimating Spin Down Energy . . . . .	76
5.2.4	Opening Angle of the Shock Front . . . . .	77
5.3	Effects of Geometry and Optical Depth . . . . .	81
<b>6</b>	<b>Closing Remarks</b>	<b>86</b>
<b>A</b>	<b>Radio Data Reduction for LS5039 using MIRIAD and KARMA</b>	<b>90</b>
A.1	Anatomy of an Observation . . . . .	90
A.2	Calculating Field of View . . . . .	91
A.3	KARMA and <b>kvis</b> . . . . .	92
A.4	MIRIAD . . . . .	93
<b>B</b>	<b>Programs Used in Analyzing the Radio Observations of LS 5039</b>	<b>115</b>
B.1	Wind Speed . . . . .	115
B.2	Orbital Separation . . . . .	118
B.3	Shock Geometry . . . . .	120



B.4 Optical Depth . . . . .	124
<b>Bibliography</b>	<b>133</b>
<b>Vita</b>	<b>141</b>

# List of Tables

2.1	Journal of Spectroscopy for HD 259440 . . . . .	26
2.2	Journal of Spectroscopy for LS 5039 . . . . .	28
3.1	OHP $V_R$ Measurements of HD 259440 . . . . .	37
3.2	Stellar Parameters of HD 259440 . . . . .	43
4.1	Orbital Elements for LS 5039 . . . . .	55
4.2	Radial Velocity Measurements of LS 5039 . . . . .	56
5.1	Radio flux expected from a thermally emitting stellar wind compared to our mean observed fluxes. . . . .	67
5.2	Radio Fluxes for LS 5039 . . . . .	68

# List of Figures

- 2.1 A schematic drawing showing how a radio interferometer functions. In the upper portion of the drawing, light from a source hits two antennas separated by a baseline,  $b$ . The light induces a voltage in each detector. The two voltages are multiplied and averaged in a correlator, producing interference fringes. The output of the interferometer can be improved by adding more baselines. This can be accomplished by either building more telescopes or using the rotation of the earth. The lower telescope shows the changing orientation of a pair of telescopes as the earth rotates. The projection of any pair of telescopes on the sky is plotted on the  $uv$ -plane. Over a twelve hour period of time, the projected baselines of the two telescopes will trace an ellipse on the  $uv$ -plane. More complete coverage of the  $uv$ -plane results in a narrower response function with smaller sidelobes. 29
- 3.1 Probability of having missed the binary companion because of a too low inclination angle as a function of the orbital period, for eccentricities equal to 0.0, 0.2, 0.4, and 0.6, respectively. In each panel, secondary masses of  $1.5 M_{\odot}$ ,  $2.0 M_{\odot}$  and  $2.5 M_{\odot}$  have been assumed. The diamonds indicate inclinations from  $10^{\circ}$  to  $80^{\circ}$ , spaced at intervals of  $10^{\circ}$ . . . . . 38
- 3.2 The mean spectra from the KPNO 2.1m (bottom) and CF (top) telescopes are plotted for comparison. The CF spectrum is offset by 0.2 for clarity. . . 41

3.3	A contour plot of the $1\sigma$ , $2\sigma$ , and $3\sigma$ errors from the spectral fits using $N = 0.7$ and $V \sin i = 500 \text{ km s}^{-1}$ . The discontinuity between the OSTAR2002 and BSTAR2006 models is marked by the vertical dashed line. The square represents the model with the lowest $\chi^2$ value for both model fits. . . . .	44
3.4	The mean KPNO 2.1m spectrum, adjusted for $N = 0.7$ , is shown as a solid line. The dashed line shows the Tlusty BSTAR2006 model spectrum with $T_{\text{eff}} = 30000 \text{ K}$ , $\log g = 4.0$ , and $V \sin i = 500 \text{ km s}^{-1}$ . The residuals from the fit are plotted below the spectrum, shifted by 0.6 for easier comparison. . . . .	45
3.5	The He I $\lambda 4471$ line from the mean KPNO 2.1m spectrum is shown in the same format as Figure 3.4. . . . .	46
3.6	Evolutionary tracks from Schaller et al. (1992). The initial mass for each track is indicated by numbers 7 through 40. Our best fit value for $T_{\text{eff}}$ and $\log g$ in the $N = 0.7$ case is plotted as a diamond with error bars. . . . .	47
3.7	The Tlusty BSTAR2006 model SED normalized to $\theta_R = 24.3 \mu\text{as}$ ( $1.13 \times 10^{-10}$ radians) is plotted as a solid line. The diamonds indicate the observed broadband photometric fluxes. The triangles represent the estimated stellar flux assuming $N = 0.7$ . . . . .	50
4.1	The mean spectrum of LS 5039 from the night of 2007 August 29, taken near the time of inferior conjunction of the optical star. We used this mean spectrum as a reference to determine the relative $V_R$ by cross correlation with each spectrum of LS 5039. . . . .	53
4.2	Radial velocity curve of LS 5039. Periastron corresponds to $\phi = 0$ in this plot. Points plotted as open diamonds are from McSwain et al. (2001, 2004), crosses are from Casares et al. (2005), and filled circles are from this work. . . . .	56

4.3	Orbital geometry of LS 5039, looking down on the orbital plane, showing the relative orbits ( $r/a$ ) of the optical star ( $23 M_{\odot}$ ; Casares et al. 2005) and the compact companion, which is either a $3.7 M_{\odot}$ black hole (Casares et al. 2005) or a $1.4 M_{\odot}$ neutron star.. The relative orbit of the compact object is shown as a solid line, while the O star's relative orbit depends on the mass of the companion. The dashed line indicates the O star's orbit assuming a $4 M_{\odot}$ black hole, while the dotted line assumes a $1.4 M_{\odot}$ neutron star. The phases of periastron, apastron, and conjunctions are marked along the orbit of the compact companion. The center of mass is indicated with a cross, and the thin solid line is the orbital major axis. . . . .	59
4.4	A close up view of the O star orbit (assuming a $1.4 M_{\odot}$ companion) to highlight the orientation of the system during our SOAR observations. The gray shaded regions indicate the phases of our observations. The diamonds mark the phases of inferior and superior conjunction. . . . .	61
4.5	The $H\alpha$ line from the SOAR observations. Consecutive pairs of spectra were coadded to reduce the S/N ratio. We shifted each spectrum to the rest wavelength to highlight any variations in the line profile due to structure in the stellar wind. . . . .	62
4.6	The mass loss rate of LS 5039 plotted as a function of orbital phase. The variations originate from error in measuring $W_{H\alpha}$ rather than any real variation in the mass loss rate of the system over the orbital period. . . . .	63
5.1	Radio flux measurements of LS 5039. . . . .	67
5.2	Ratio of fluxes for 3 cm/6 cm and 6 cm/13 cm plotted with respect to orbital phase. . . . .	69

5.3	The basic geometry of a wind-wind collision. The O star and the pulsar are represented by filled circles, where $D$ is the distance between them. The stagnation point is marked by an open square. The shockfront is the solid hyperbola opening to the left. $R_p(\theta)$ represents the distance from the pulsar to the shockfront, While $R_{stag}$ represents the location of the stagnation point with respect to the pulsar. $\theta_\infty$ is the opening angle of the shock. Units are arbitrary. . . . .	71
5.4	Diagram of an elliptical orbit. The large dot represents the focus of the ellipse from which the true anomaly, $\xi$ , is measured. The small dot represents the orbiting object. The eccentric anomaly, $E$ , is determined by the projection of the location of the object onto a circle with a radius equal to ellipse's semi-major axis, $a$ . The line marked $b$ represents the semi-minor axis of the ellipse. . . . .	72
5.5	The distance of the compact object from the O star, $D$ , is indicated by the dotted line, while the location of the stagnation point, $R_O$ , is represented by the solid line. . . . .	74
5.6	The ratio of $v_O$ to $v_{O,\infty}$ at the location of the compact object in LS 5039, assuming a $1.4 M_\odot$ neutron star and $23 M_\odot$ for the O star. . . . .	80
5.7	The optical depth at the location of the stagnation point of the shock for 3 cm, 6 cm, and 13 cm wavelengths. The dotted line indicates $\tau_\nu = 1$ . . . . .	82
5.8	The optical depth as seen by an observer looking into the O star wind. Each open contour represents the distance from the O star at which the optical depth of the O star wind along the line of sight goes to 1 for radio waves at 20 cm, 13 cm, 6 cm, and 3 cm. The arrow indicates the direction towards the observer. The solid line represents the orbit of the compact object with respect to the O star. The dashed closed contour represents the location of the stagnation point as calculated in Section 5.2.2. The solid circle represents the O star. . . . .	83

6.1 (Left) The upper portion of the plot shows the  $H\alpha$  line of HD 259440 as observed on 35 consecutive nights with the KPNO CF telescope from 2008 October to November, sorted by HJD. The lower portion of the plot shows a gray scale image produced by a linearly interpolating between the observed spectra. Since no period was known at the time of our publication, the “Arbitrary Phase” goes from 0 at the start of the observing run to 1.0 at the end of the run. The intensity at each velocity in the gray-scale image is assigned one of 16 gray levels based on its value between the minimum (bright) and maximum (dark) observed values. (Right) The upper panel shows the  $H\alpha$  residual spectra of HD 259440, and the bottom panel shows a grayscale plot of the same residuals. The residual spectra were calculated by creating a reference spectrum from the average of all 35 nights of observations and subtracting this average from each individual observation. The residual spectra reveal variations in the  $H\alpha$  line with a  $\sim 60$  d period that we attribute to a spiral density wave in the circumstellar disk. . . . . 88

# Abbreviations

ATCA	Australia Telescope Compact Array
Be/XRB	Be/X-ray binary
CCD	charge coupled device
CF	Coudé Feed
CTIO	Cerro Tololo Inter-American Observatory
FWHM	full width half max
EGRET	Energetic Gamma-Ray Experiment Telescope
GHTS	Goodman High Throughput Spectrograph
HESS	High Energy Stereoscopic System
HJD	Helio-centric Julian Date
HMXB	high mass X-ray binary
IDL	Interactive Data Language
IRAF	Image Reduction and Analysis Facility
JD	Julian Date
KPNO	Kitt Peak National Observatory
OHP	Observatoire Haute-Provence
SOAR	Southern Astrophysical Research Telescope
SED	spectral energy distribution
S/N	signal-to-noise
ThAr	Thorium Argon
VERITAS	Very Energetic Radiation Imaging Telescope Array System



# Abstract

High mass X-ray binaries (HMXBs) consist of an O or B star orbited by either a neutron star or a black hole. Their high-energy emission is produced by an interaction between the compact object and the stellar wind. Of the 114 known Galactic HMXBs, a handful of these objects, dubbed  $\gamma$ -ray binaries, have been observed to produce MeV-TeV emission. Their unusual behavior is typically explained by one of two scenarios. If the compact object is a black hole, it can accrete material from the stellar wind, forming an accretion disk and relativistic jets which produce emission from  $\gamma$ -ray to radio wavelengths. Systems with this geometry are known as microquasars, since they resemble stellar-scale versions of active galactic nuclei. High mass X-ray binaries (HMXBs) consist of an O or B star orbited by either a neutron star or a black hole. If the compact object is a pulsar, it will produce its own relativistic wind. This wind will collide with the massive star wind, resulting in a shock region where the high energy emission is produced. Both these scenarios make  $\gamma$ -ray binaries valuable nearby systems for studying the physics of shocks and jets.

$\gamma$ -ray binaries represent a rare class of objects displaying interesting physics, highlighting the importance of understanding the mechanisms which drive very high energy emission in these systems. Currently, the nature of the compact object and the high energy production mechanism is unknown or unconfirmed in over half of these systems. My goal for this dissertation is to constrain the parameters describing two of these systems: LS 5039

and HD 259440.

LS 5039 exhibits  $\gamma$ -ray emission modulated with its orbital period. The system consists of an ON6.5V((f)) star and an unidentified compact companion. We have used optical spectra of LS 5039 from the CTIO 1.5m telescope and the SOAR telescope to examine the system's orbital parameters and the stellar wind strength of the O star. We found LS 5039 to have an orbital period of 3.90608 d and an eccentricity of 0.337. Spectra of the  $H\alpha$  line as observed by SOAR indicate a mass loss rate of  $\sim 1.9 \times 10^{-8} M_{\odot} \text{ yr}^{-1}$ . Interferometric radio observations of LS 5039 were obtained at 13 cm, 6 cm, and 3 cm using the Australia Telescope Compact Array (ATCA) between 2008 February and 2009 July. The reduced radio fluxes are between 10-40 mJy and show variability with time, indicating a source other than thermal emission from the stellar wind.

HD 259440 is a B0pe star that was proposed as the optical counterpart to the  $\gamma$ -ray source HESS J0632+057. Here we present optical spectra of HD 259440 acquired to investigate the stellar parameters, the properties of the Be star disk, and evidence of binarity in this system. Emission from the  $H\alpha$  line shows evidence of a spiral density wave in the nearly edge-on disk. We find a best fit stellar effective temperature of 27500–30000 K and a log surface gravity of 3.75–4.0, although our fits are somewhat ambiguous due to scattered light from the circumstellar disk. We derive a mass of 13.2–19.0  $M_{\odot}$  and a radius of 6.0–9.6  $R_{\odot}$ . By fitting the spectral energy distribution, we find a distance between 1.1–1.7 kpc. We do not detect any significant radial velocity shifts in our data, ruling out orbital periods shorter than one month. If HD 259440 is a binary, it is likely a long period ( $> 100$  d) system.

# Chapter 1

## Introduction

The broad field of astronomy attempts to answer questions about the origin of the universe, the nature of its structure, and our place in it. In order to answer these broad questions, we first need to gain understanding of the pieces that make up this structure. Before we can accurately model the evolution of galaxies, we need to have a firm handle on the nature and evolution of their stellar populations. Among any stellar population, the vast majority of members will be low mass stars, about or less than the mass of the sun. While massive stars are rare compared to their lower mass counterparts, they play an important role in the composition of the interstellar medium and star formation. Their strong winds enrich the interstellar medium from which younger stars are formed. Massive stars end their lives in violent explosions, called supernova, which can trigger new star formation events. They are often found in binary systems, where their strong winds can interact with the companion object creating regions of shocked material or accretion streams and disks. These systems act as natural particle accelerators, which can be used to probe fundamental physics.

## 1.1 Massive Stars

Astronomers classify objects based on similar observational characteristics. Nearly all stars are too far away to obtain resolved images, so the information we can gather on these objects is based on how they emit light of various wavelengths. Spectra of stars can reveal details about a star's temperature, surface gravity, winds, and structure, which are discussed further in Section 1.4.3.

Stars are classified by the characteristics of the strong absorption lines in their spectra. Spectral classes are designated by a series of letters: O, B, A, F, G, K, M, L, and T, with O being the hottest and T being the coolest. Each spectral class is subdivided into ten categories labeled 0 through 9, with lower numbers corresponding to hotter temperatures. For example, the Sun is a G2 type star, with a temperature of about 5,700 K. It is hotter than a G3 star and cooler than a G0 star. In the case of two stars of the same temperature where one is larger in radius, the larger star will emit more flux and appear brighter in observations. Luminosity classes, designated by Roman numerals I through V, are used to differentiate between stars of the same temperature but different sizes. Supergiant stars are represented by I, bright giants are represented by II, giant stars are class III, subgiants are class IV, and class V are dwarf or main sequence stars. A star's luminosity class can also be identified through spectral features. Giants and supergiants represent later stages of stellar evolution, where the outer layers of the stellar atmosphere have expanded. Due to the lower density of this material, the effects of interactions between ions in the atmosphere are weaker than in main sequence stars. Energy levels within an atom will be shifted due to perturbations by nearby ions and electrons, which broaden the observed spectral lines as a function of the gas pressure in a star's atmosphere. As a result, strong spectral lines from supergiants exhibit less pressure broadening than those from a comparable main sequence

star. Comparing the relative strengths of closely spaced spectral lines can also be used to determine luminosity class. The spectral types and luminosity classes are used together to create the Morgan-Keenan classification system.

HD 259440 and the O star in LS 5039 are members of the two hottest classes of stars, with temperatures upwards of six times that of the Sun. Stars this large distribute heat convectively in their cores and radiatively through their outer layers. O stars are the hottest of all stars, with temperatures above 30,000 K and masses that can be 15 to 100 times that of the Sun. Their optical spectra show strong hydrogen Balmer lines, which represent the transitions from the  $n = 2$  level in the hydrogen atom. Strong absorption lines from singly ionized and neutral helium (designated He II and He I, respectively) are also present in O star spectra. B stars represent the second hottest spectral class, typically exhibiting temperatures between 10,000 K and 30,000 K and masses about 2 to 15 times that of the Sun. These spectra show stronger hydrogen lines than the O stars and strong He I absorption lines. The latter peak in the spectra of B2 stars.

A classical Be star is a non-supergiant B star that has exhibited emission in one or more of its photospheric lines that is generated by hot gas in a circumstellar disk (Porter & Rivinius 2003). Be star emission lines often have a distinctive double peaked shape. The Be star disks are comprised of hot, diffuse gas. An observer will see a portion of the circumstellar disk extending beyond the optical star. This gas is not backlit by the hotter B star, and will produce emission lines. The material in the disks orbit the star with Keplerian motion. As the disk rotates, part of the emitting material is traveling towards the observer, while another portion is traveling away. This causes part of the emission line to be blue shifted, while another portion is red shifted. This emission is superimposed on the photospheric absorption line from the star, creating a distinctive double peaked emission

feature. Be star disks differ from the debris disks which can lead to planet formation, as they are fed by material ejected from the surface of the star and composed primarily of hydrogen gas instead of dust. Therefore, emission is usually observed in the hydrogen Balmer lines. The contribution of the disk emission is strongest in  $H\alpha$  and weakens towards the Balmer jump. Occasionally, emission features can be seen in helium and iron lines as well. Be star disks are geometrically thin, meaning that they have a small scale height in comparison with their radius, and are supported by the angular momentum of the gas ejected from the star. The disks can form and dissipate on timescales from months to years (Porter & Rivinius 2003). Be stars comprise about 18% of field B-type stars and 2-7% of cluster B-type stars (Abt 1987; McSwain & Gies 2005).

## **1.2 Compact Objects: Neutron Stars and Black Holes**

The following discussion of basic neutron star properties is based on information from *An Introduction to Modern Astrophysics* by Carroll & Ostlie (2007). In order to maintain their stability, stars must exist in or evolve towards hydrostatic equilibrium. This simply means that in any given location in the star, the forces of gravity and gas pressure balance to zero. Stars are not actually in a perfect state of hydrostatic equilibrium throughout their structure: they expand as they evolve off of the main sequence, lose material through the stellar wind, etc. However, this condition must hold approximately true in general, or the star would either collapse or explode. Stars produce the energy that supports their layers through nuclear fusion in their cores. Massive stars can fuse material up through iron; fusing heavier elements will require energy to be absorbed. At this point the condition of hydrostatic equilibrium can no longer be satisfied: the core of the star collapses and the outer layers of the star are ejected in a supernova explosion.

If the core of the star is greater than  $1.4 M_{\odot}$  when the star explodes into a supernova, the electron degeneracy pressure of the core will not be sufficient to counteract the force of gravity and the core will collapse. If the remaining mass is less than about  $2.6 M_{\odot}$  (Walecka 2007), the result of this collapse will be a neutron star. A  $1.4 M_{\odot}$  neutron star will have a typical radius of about 10 km and is supported by neutron degeneracy pressure. In order for a neutron star to remain dynamically stable and maintain hydrostatic equilibrium, it must be able to adjust its pressure to account for small changes in its structure. The rate of this adjustment is constrained by the speed of sound within the object. A rotating neutron star of  $2.9 M_{\odot}$  or a static neutron star of  $2.2 M_{\odot}$  will not be able to adjust to disturbances in its structure and it will collapse into a black hole. Neutron stars typically exhibit rapid rotation rates on the order of second to millisecond timescales and harbor strong magnetic fields.

Pulsars are rapidly rotating neutron stars which were first discovered by Jocelyn Bell in 1967. They produce regular pulses of light timed on the order of seconds to milliseconds which can range in energy from radio to  $\gamma$ -ray wavelengths. Their strong dipole magnetic fields are inclined with respect to the rotational axis. This creates areas of changing magnetic field around the pulsar, which induces an electric field. The energy radiated away from the pulsar through this process will increase the rotation period of the pulsar, a phenomenon known as spindown. The powerful induced electric field can also pull ions or electrons away from the pulsar's surface, creating a magnetosphere around the pulsar. These particles will co-rotate with the pulsar until they reach the edge of the light cone. The light cone is the radius at which a point co-rotating with the pulsar will be travelling at the speed of light. As this is not physically possible, the particles at this radius will be spun away, resulting in the pulsar wind. These charged particles will continue to interact with the pulsar's magnetic field and the induced electric field to create the pulses we observe.

The electric field accelerates the particles to relativistic speeds and the particles interact with the magnetic field lines to produce highly-polarized curvature radiation. The resulting emission is highly-beamed and composed of  $\gamma$ -rays which undergo pair production. This creates a cascade effect of electron and positrons forming and annihilating over the neutron star's magnetic poles. Particles moving outwards along the magnetic field lines continue to emit curvature radiation at lower wavelengths. The pulses are created as this beamed radiation over the magnetic poles is swept around by the neutron star's rapid rotation.

If the core of a star undergoing a supernova is more than about  $2.6 M_{\odot}$ , neutron degeneracy pressure is no longer strong enough to counteract the force of gravity and the mass will collapse into a black hole. Black holes are collections of matter so dense that they deform space time in their immediate vicinity. They can be described by three independent parameters: mass, angular momentum, and charge. The mass of a black hole determines the Schwarzschild radius (also known as the event horizon),  $R_s = \frac{2M_{BH}G}{c^2}$ , where  $M_{BH}$  is the mass of the black hole. All of the mass from the black hole is contained in an area smaller than this radius. At distances larger than  $R_s$ , the black hole will behave as a spherically symmetric gravitational source with mass  $M_{BH}$ . We cannot observe the structure of a black hole at radii smaller than  $R_s$ , since light cannot escape from beyond the event horizon (Walecka 2007).

### **1.3 High Mass X-ray Binaries and $\gamma$ -ray Binaries**

X-ray binaries consist of a star interacting with either a neutron star or a black hole to produce high energy radiation. High mass X-ray binaries (HMXBs) typically contain O or B stars as the optical companion and mostly exist in two subclasses. Supergiant X-ray binaries have luminosity class I or II stars as the optical counterpart. Remember from the



discussion in Section 1.1 that this indicates a companion star in the later stages of stellar evolution. Systems with a Be star optical counterpart are commonly referred to as Be/X-ray binaries (Be/XRBs; Coe 2000). Of the 114 known Galactic HMXBs, about 60% contain a Be star as the optical counterpart and 32% contain a supergiant O or B type star (Liu et al. 2006).

Within a binary system, we can calculate an equipotential surface from the two gravitational fields and the centrifugal force due to the orbital motion, known as the Roche-lobe. If the donor star is larger than this surface, the outer layers of the star will overlap a region where gravity of the companion dominates. This material will be accreted onto the companion star in a process known as Roche-lobe overflow. The X-ray production in HMXBs can either be powered by Roche-lobe overflow or an interaction between the compact object and the stellar wind.

Be/XRBs were first discovered in 1974. They display a wide range of orbital periods, from several weeks to several years. Between 100 and 1000 are predicted to exist in the Milky Way Galaxy. The Be/XRBs can be divided into two classes. Type I systems experience regular, periodic outbursts at periastron: at this phase, the compact object has reached its point of closest approach and can interact with the Be star disk. Type II systems exhibit giant outbursts that are not correlated with the orbital phase of the binary. Since Be star disks change in size and structure over time, these events could be due to disk expansion. For all Be/XRBs, the phases of outbursts can shift as the disk features change. The equivalent width of the  $H\alpha$  line, which probes the size of the circumstellar disk (Grundstrom & Gies 2006), has been linked to observed X-ray emission, supporting this conclusion (Coe 2000).

The Be stars in Be/XRBs are most commonly between spectral classes B0 and B2.

The systems are thought to begin as close binaries involving two massive stars and mass transfer. Through conservation of angular momentum, the mass transfer slowly widens the orbit. At the time of the supernova explosion, the large separation distances between the stars will make the orbit easier to disrupt. If the less evolved companion in the system is more massive, the binary is more likely to survive the supernova explosion. This scenario favors Be/XRBs with early-type B stars and compact companions in an eccentric orbit (Coe 2000).

HMXBs that also produce very high energy radiation on the order of MeV-TeV ( $\gamma$ -ray binaries) are a rare and interesting class of objects. Of the 114 Galactic HMXBs, only a handful have been observed to produce  $\gamma$ -ray emission, including LS 5039 (Aharonian et al. 2005a), LS I +61 303 (Albert et al. 2006), PSR B1259–63 (Aharonian et al. 2005b), and HESS J0632+057 (Aharonian et al. 2007; Hinton et al. 2009). For most of these objects, the source of their high energy radiation is not yet understood. Each of these systems likely consists of a compact object interacting with a massive O- or B-type stellar companion to create the high energy radiation.

Some  $\gamma$ -ray binaries may fit a microquasar model, where matter accreting onto a neutron star or black hole is accelerated to high velocities and produces relativistic jets. The name microquasar was assigned because at first, these objects seemed to resemble quasars. Quasars are the highest energy examples of active galactic nuclei, or AGN. In these systems, large amounts of matter are accreted onto supermassive black holes at the centers of galaxies, producing relativistic jets. This class of objects can be seen to cosmological distances and offers insight into the evolution of galaxies. The  $\gamma$ -ray binary PSR B1259–63 produces  $\gamma$  radiation in a shock region formed by the relativistic wind from a non-accreting pulsar and a dense stellar wind (Cominsky et al. 1994). This object is the prototype for the

colliding wind scenario, the second leading theory explaining very high energy emission in  $\gamma$ -ray binaries.

LS 5039 consists of an ON6.5V((f)) primary (McSwain et al. 2004) and an unknown compact companion. This object is currently of great interest across the entire electromagnetic spectrum. The detection of extended radio emission from LS 5039, resembling the jets found in quasars, implies a microquasar scenario (Paredes et al. 2000, 2002). However, no evidence of an accretion disk has been found thus far in the optical or X-ray data (McSwain et al. 2004; Bosch-Ramon et al. 2007). An alternative theory (Dubus 2006) proposed that the high energy emission could be produced by a relativistic wind from a pulsar colliding with the O-star wind. The X-ray emission from LS 5039 does appear to be correlated with the stellar wind strength, consistent with stellar wind accretion (McSwain et al. 2004; Bosch-Ramon et al. 2005). A radio pulsar search was conducted by our research collaboration in the fall of 2008, but did not yield conclusive results (McSwain et al. 2011). The compact companion remains unidentified. I present my investigation of the optical and radio properties of LS 5039 in Chapters 4 and 5.

HD 259440 is a Be star which has been associated with the proposed  $\gamma$ -ray binary HESS J0632+057 (Hinton et al. 2009). The high energy source was first observed by the High Energy Spectroscopic System (HESS) array. This telescope consists of a collection of ground based telescopes that detect the Čerenkov radiation generated by  $\gamma$ -rays entering Earth's atmosphere and trace the detected emission back to a region of the sky. Since then, HESS J0632+057 has been associated with X-ray sources XMMU J063259.3+0548011, RXS J063258.3+054857, and 3EG J0634+0521 (Hinton et al. 2009; Aharonian et al. 2007;

Skilton et al. 2009) and a radio source (Skilton et al. 2009; see Section 3.1). The multi-wavelength observations support the classification of this system as a  $\gamma$ -ray binary. SIMBAD<sup>1</sup> gives a spectral type of B0pe for HD 259440. A search of the literature reveals that prior to the HESS detection, optical observations of the Be star had not searched for signatures of a binary system (Turner 1976; Morgan et al. 1955; Gutiérrez-Soto et al. 2007). To address this lack of information, we collected optical observations of HD 259440 to determine the stellar parameters and constrain the orbital parameters for the system. The details of this investigation are presented in Chapter 3.

## 1.4 Radiation Sources in $\gamma$ -ray Binaries

Astronomers use the term “optical depth,” typically denoted by  $\tau$ , to quantify the ability of light to pass through a material. Consider a source (perhaps a core of a star) with some initial intensity  $I_0$ . As the light from this source passes through layers of gas, some of it will be absorbed and scattered off ions and electrons. Optical depth is frequency dependent and can be calculated based on the properties of the atoms, molecules, or ions in the material. The optical depth contains information on the mean free path of the photons, and so it is related to the thickness of the layer of gas. Layers of material with an optical depth  $> 1$  are opaque to light. An optical depth of  $< 1$  is considered to be transparent to radiation. Therefore, the light we observe from a star is being emitted from above the radius where  $\tau \approx 1$ . All the absorption lines that we observe in stellar spectra are generated in these layers of the star’s upper atmosphere with  $\tau < 1$ , commonly referred to as the photosphere.

---

<sup>1</sup><http://simbad.u-strasbg.fr/simbad/sim-fid>

### 1.4.1 High Energy Continuum Processes

Free-free absorption or emission is a common continuum process in astrophysical systems. As a free electron passes near an ion, it can either absorb a photon as it accelerates or emit a photon as it decelerates. The latter case is called *Bremsstrahlung*, or braking radiation. The interaction between an electron moving at some speed,  $v$ , and an ion with an impact parameter,  $b$ , can be described by a typical duration of the interaction,  $l = b/v$  and a typical frequency,  $\omega_c = 1/l$ . Electron-ion interactions will produce little to no radiation above  $\omega_c$ . This formulation can be applied to a collection of electrons with some velocity distribution, and will typically produce a spectrum that is relatively flat up to some cut off frequency. Above this frequency, the flux will rapidly fall off (Rosswog & Brüggen 2007). Bremsstrahlung is an efficient emission process for thermal populations of electrons. This emission is partly responsible for the continuum emission from the Be star disk of HD 259440 as discussed in Chapter 3. Free-free absorption is also assumed to be the primary source of opacity from O star winds in the models discussed in Chapter 5.

If the compact object has a strong magnetic field, synchrotron emission can arise from charged particles in the winds spiraling around the magnetic field lines. While populations of particles with thermal velocity distributions can produce synchrotron emission, the effect is typically weak and difficult or impossible to detect. As a result, we most commonly observe synchrotron emission from populations of particles with non-thermal velocity distributions (e.g. particles traveling at relativistic speeds; Melia 2009). We can begin by assuming a non-thermal power-law distribution

$$N(E)dE = KE^{-x}dE \tag{1.1}$$

where  $N(E)$  is the number of particles with energy  $E$ ,  $K$  is a normalization constant, and

$x$  is typically between 2.0 and 2.5 (Melia 2009). We expect the emission from a single particle in a magnetic field to be highly peaked at some critical frequency,  $\nu_c$ , such that

$$\nu_c = \left( \frac{E}{m_e c^2} \right) \nu_{gyr} \quad (1.2)$$

$$\nu_{gyr} \equiv \frac{eB}{2\pi m_e c} \quad (1.3)$$

where  $B$  is the magnetic field acting on the electron,  $e$  is the charge of the electron,  $m_e$  is the mass of the electron,  $c$  is the speed of light, and  $\nu_{gyr}$  is the gyration frequency. In order to calculate the power of radiation as a function of frequency,  $P_{tot}$ ,

$$dE \approx \frac{m_e c^2}{2(\nu_{gyr} \nu)^{1/2}} d\nu \quad (1.4)$$

$$P_{tot}(\nu) = \int \left( -\frac{dE}{dt} \right) N(E) dE \propto B^{(x+1)/2} \nu^{-(x-1)/2} \quad (1.5)$$

If we set  $\Gamma = -(x - 1)/2$ , the shape of a synchrotron spectrum can be described by a power-law equation of the form

$$F = C\nu^\Gamma \quad (1.6)$$

where  $F$  is the flux,  $\Gamma$  and  $C$  are constants, and  $\nu$  is the frequency of the radiation. At low energies, electrons will reabsorb the synchrotron emission emitted from their neighbors, resulting in a distinctive spectrum following a power law of  $\Gamma = \frac{5}{2}$  (Melia 2009; Rosswog & Brüggen 2007).

Compton scattering occurs when a photon collides with an electron, resulting in the deflection of the electron and the photon and decreasing the energy of the photon. Inverse Compton scattering involves a high energy electron colliding with a low energy photon and increasing the photon's energy. This effect can distort the spectral energy distribution from the object by shifting low energy photons in the black body curve to higher energies.

The mechanism for both of these processes is the same except for the direction of energy transfer. Compton scattering involves highly energetic photons, so we need to consider the effects of special relativity. In this interaction, we start in the rest frame of the electron. The initial momenta of the electron,  $p_{e,i}$ , and the photon,  $p_{\gamma_i}$ , are

$$p_{e,i} = (m_e c^2, \vec{0}) \quad (1.7)$$

$$p_{\gamma_i} = \left( \frac{\epsilon}{c}, \frac{\epsilon}{c} \hat{\mathbf{z}} \right) \quad (1.8)$$

where  $\epsilon$  is the initial energy of the photon. After the collision,

$$p_{e,f} = (m_e c^2, \vec{\mathbf{p}}) \quad (1.9)$$

$$p_{\gamma_f} = \left( \frac{\epsilon'}{c}, \frac{\epsilon'}{c} \hat{\mathbf{z}}' \right) \quad (1.10)$$

Through conservation of energy and momentum,

$$\epsilon' = \frac{\epsilon}{1 + (\epsilon/m_e c^2)(1 - \cos \theta)} \quad (1.11)$$

where  $\theta$  is the change in angle of the photon's path. This scattering process is most effective in non-thermal populations of electrons. For a single electron, the radiated power,  $P_{comp}$ , is given by

$$P_{comp} = \frac{4}{3} \sigma_T c \beta^2 \gamma^2 u_{rad} \quad (1.12)$$

where  $\sigma_T$  is the Thompson scattering cross section,  $\beta$  is the speed of the electron over the speed of light,  $\gamma$  is the Lorentz factor, and  $u_{rad}$  is the energy density of the radiation field. We can describe the non-thermal population of electrons in terms of their Lorentz factors

$$N(\gamma) d\gamma = K \gamma^{-x} d\gamma \quad (1.13)$$

to find the total power emitted due to the population of electrons

$$P_{tot} = \int_1^{\gamma_{max}} P_{comp}(\gamma) N(\gamma) d\gamma \approx \frac{4}{3} \sigma_T c u_{rad} \frac{K}{3-x} \gamma_{max}^{3-x} \quad (1.14)$$

This expression is similar in form to the total power expected from synchrotron radiation, except that it is dependent on the energy density of the radiation field rather than the magnetic field. Since the  $P_{sync}$  and  $P_{comp}$  have such similar forms, their ratio (obtained from observations) can be used to determine the strength of a magnetic field in the system, if the energy density of the incident photons are known (Melia 2009).

### 1.4.2 The Stellar Spectral Energy Distribution

In order to describe the spectral energy distribution (SED) of the star, we can start by considering the effect of light with some intensity,  $I_\nu$ , incident on a surface area,  $A$ , at some angle,  $\theta$ . The flux,  $F_\nu$ , is defined as the net energy flowing through some surface per unit time per unit frequency and can be written as

$$F_\nu = \int_A I_\nu \cos \theta d\Omega \quad (1.15)$$

where  $\Omega$  represents the solid angle subtended by  $A$  as seen by an observer. To first order, we can approximate  $I_\nu$  from a star with a blackbody at some effective temperature,  $T_{\text{eff}}$ . The Planck function for the blackbody is

$$B_\nu(T_{\text{eff}}) = \frac{2h\nu^3}{c^2} \frac{1}{e^{h\nu/kT_{\text{eff}}} - 1} \quad (1.16)$$

where  $k$  is Boltzmann's constant,  $\nu$  is the frequency, and  $h$  is Planck's constant. Assuming that the blackbody is emitting an isotropic (spherically symmetric) radiation field,  $F_\nu$  will reduce to

$$F_\nu = \pi I_\nu \quad (1.17)$$

We can derive total power per unit area at the surface of the star by integrating  $F_\nu$  over all frequencies, such that

$$\int_0^\infty F_\nu d\nu = \frac{2\pi^5 k^4}{15h^3 c^2} T_{\text{eff}}^4 = \sigma T_{\text{eff}}^4 \quad (1.18)$$



where  $F_\nu$  is the stellar flux as a function of frequency and  $\sigma$  is the Stefan-Boltzman constant. Luminosity,  $L$ , is the total power radiated from the surface of the star and can be written as

$$L = 4\pi R^2 \int_0^\infty F_\nu d\nu \quad (1.19)$$

where  $R$  is the radius of the spherical star (Gray 2005).

We can use the observed flux of the star to determine its angular size,  $\theta_R$ , and distance,  $d$ . If  $F_{\nu,\oplus}$  is the flux observed from earth and  $F_{\nu,\star}$  is the flux at the surface of the star, then

$$4\pi d^2 F_{\nu,\oplus} = 4\pi R^2 F_{\nu,\star} \quad (1.20)$$

where  $R_\star$  is the radius of the star. Integrating both sides of the equation over  $\nu$  and rearranging the terms yields

$$\int_0^\infty F_{\nu,\oplus} d\nu = \left(\frac{R}{d}\right)^2 \int_0^\infty F_{\nu,\star} d\nu = \theta_R^2 \sigma T_{\text{eff}}^4 \quad (1.21)$$

where  $\theta_R = R/d$  is the angular radius of the star. Observing the total flux output by a star at all frequencies is impractical, so we can modify the technique to use observations at specific frequencies. We can rewrite Equation 1.21 without the integrals as

$$\theta_R = \frac{R}{d} = \left(\frac{F_{\nu,\oplus}}{F_{\nu,\star}}\right)^{1/2} \quad (1.22)$$

Using this equation, the distance to the star can be determined by determining  $F_{\nu,\star}$  from a model SED and fitting it to observations of  $F_{\nu,\oplus}$  (Gray 2005).

The blackbody function can provide a reasonable first order estimate for the shape of a massive star's SED. Continuum and bound-bound processes in the star's photosphere will alter this basic shape. In the photospheres of O and early B type stars, electron scattering represents a significant source of continuum absorption (Gray 2005). This process is

independent of wavelength, with an absorption coefficient given by

$$\alpha(e) = \frac{8\pi}{3} \left( \frac{e^2}{mc^2} \right) \quad (1.23)$$

In F-type stars and hotter, the absorption of photons by neutral hydrogen atoms is another strong effect altering the shape of the SED. At ultraviolet wavelengths, this effect is observed at the Balmer jump, which occurs at the wavelength where photons are energetic enough to ionize a hydrogen atom with an electron in the  $n = 2$  energy level. The central wavelength for any bound-bound transition from the  $n = 2$  energy level is

$$\frac{1}{\lambda} = \mathcal{R}_\lambda \left( \frac{1}{2^2} - \frac{1}{m^2} \right) \quad (1.24)$$

where  $\mathcal{R}_\lambda$  is the Rydberg constant. As  $m \rightarrow \infty$ , the spectral lines will become closer together. The overlapping line wings will lower the level of the continuum. Photons with  $\lambda < 3646 \text{ \AA}$  will be energetic enough to ionize the atom and the continuum flux of the star will drop off suddenly at this wavelength. This bound-free transition is referred to as the Balmer jump. The effect of the Balmer jump is the most extreme in A type stars and plays an important role in shaping B star SEDs as well (Gray 2005).

### 1.4.3 Spectral Lines: Bound-Bound Transitions

As noted above, stars are characterized by their spectral line features. These lines are formed in the outer layers of the star, called the photosphere, and are shaped by several microscopic and macroscopic processes. Spectral lines are the result of bound-bound transitions within an atom. Either an atom absorbs a photon, shifting an electron to a higher energy level, or emits a photon when an electron falls into a lower energy level. Since the photosphere is illuminated by the radiation generated from deeper in the star, we expect to see absorption lines from this layer. If the energy of the absorbed photon could simply be

determined by the difference in energy between the two energy levels, we would expect a narrow line centered on that wavelength. The spectral lines of stars are broader than this due to a variety of processes.

Broadening due to the Heisenberg Uncertainty Principle is called natural broadening. The energy of an electron in a given level is uncertain by

$$\Delta E = \frac{h}{2\pi\Delta t} \quad (1.25)$$

where  $\Delta t$  is the lifetime of that energy level. This effect is minor, compared to the other sources of stellar line broadening discussed below, and does not have a significant effect on the line shape.

The atoms surrounding a star are also heated to some temperature,  $T$ , which determines the thermal distribution of velocities within the gas. Atoms in a hot gas have a Maxwellian velocity distribution,

$$\frac{dN}{N} = \left(\frac{m}{2\pi kT}\right)^{1/2} e^{-(\frac{1}{2}v_r^2/kT)} dv_r \quad (1.26)$$

where  $v_r$  is the radial velocity with respect to the observer with an expectation value for the speed of  $\langle v_r \rangle = \left(\frac{2kT}{m}\right)^{1/2}$ , where  $k$  is Boltzmann's constant,  $T$  is the temperature of the gas, and  $m$  is the mass of the atom. Atoms moving at different speeds will see the starlight Doppler shifted by different amounts. In the frame of reference of each atom, the light from the star is Doppler shifted as given by the equation

$$\frac{\Delta\lambda}{\lambda_0} = \frac{v_r}{c} \quad (1.27)$$

where  $\Delta\lambda$  is the wavelength observed by the atom minus the rest wavelength,  $\lambda_0$  is the rest wavelength,  $v_r$  is the radial velocity of the atom, and  $c$  is the speed of light. Using the most probable atomic velocity for  $v_r$  yields

$$\Delta\lambda_D = \frac{\lambda_0}{c} \left(\frac{2kT}{m}\right)^{1/2} \quad (1.28)$$

Finally, we can use this relationship to rewrite the equation describing the distribution of velocities per particle in terms of  $\Delta\lambda_D$ . This yields an expression for the line shape due to thermal processes of

$$\alpha(\Delta\lambda) = \frac{\pi^{1/2}e^2}{mc} f \frac{\lambda_0^2}{c} \frac{1}{\Delta\lambda_D} e^{-(\Delta\lambda/\Delta\lambda_D)^2} \quad (1.29)$$

where  $\frac{\pi^{1/2}e^2}{mc} f \frac{\lambda_0^2}{c}$  describes the energy absorbed from the incident radiation per unit of intensity and  $\alpha$  defines the absorption coefficient for Doppler broadening. As is evident from Equation 1.29, the Doppler broadening produces lines with a Gaussian profile (Gray 2005).

Finally, the line width will be affected by pressure broadening. Higher pressure results in denser material. An increase in density means that the ions and electrons in the stellar atmosphere are closer together and therefore more likely to interact. Collisions of an atom with another particle will distort the energy levels in the atom, changing the frequency of light needed to cause a given bound-bound transition. The change in energy is a function of the distance between the particles,  $R$ , which describes the shift in frequency,  $\Delta\nu$ , by a power law of the form

$$\Delta\nu = \frac{C_n}{R^n} \quad (1.30)$$

$C_n$  is a constant that must be calculated or measured for each specific combination of energy levels, particles, and interaction. The value of  $n$  varies depending on the type of interaction. Hydrogen lines are heavily affected by the linear Stark effect, where the perturbing particle is a proton or electron and  $n = 2$ . In hot stars, the quadratic Stark effect will also be significant. In this case,  $n = 4$  and the atoms are perturbed by both ions and electrons (Gray 2005). Ultimately, a line that is purely pressure broadened would have a Lorentz profile (Carroll & Ostlie 2007).

In order to fully describe the line profile produced by a star, the contributions to the line

profile from each process must be convolved. The resulting function is the Voigt profile.

$$\phi(\lambda - \lambda_0) = \frac{a}{\pi^{3/2} \Delta \nu_D} \int_{-\infty}^{\infty} \frac{e^{-y}}{(u - y)^2 + a^2} dy \quad (1.31)$$

$$y = \frac{v_0 \lambda_0}{c \Delta \lambda_D} \quad (1.32)$$

$$u = \frac{\lambda - \lambda_0}{\Delta \lambda_D} \quad (1.33)$$

$$a = \frac{\lambda^2 \gamma}{4\pi c \Delta \lambda_D} \quad (1.34)$$

Here,  $\lambda_0$  is the rest wavelength of the line and  $\gamma$  is a constant determined by the natural broadening and collisional damping constant. Doppler broadening dominates near the line center, and the line core can be accurately described with a Gaussian profile. The Lorentzian component from the pressure broadening dominates in the line wings.

Further complicating the situation, macroscopic processes can also have an effect on the line profile. The movement of the star through space will Doppler shift the line. Line broadening will occur due to the rotation of the star. The motion of clumps of gas within a system, such as in a stellar wind or Be star disk, will result in a distorted line profile. The light these clumps absorb or emit will be Doppler shifted and superimposed on the line profile from the actual star (Carroll & Ostlie 2007).

# Chapter 2

## Observations

### 2.1 Introduction

Astronomical objects are located at very large distances from earth. To gather any information on their properties, we need to collect the light they produce and analyze its features. Two common methods for obtaining useful information are photometry and spectroscopy. Photometry involves measuring the radiation flux of an object within a specific wavelength range. In optical telescopes, this is achieved by placing a standardized filter in front of the camera, usually a charge-coupled device (CCD). For radio observations, the detectors attached to the telescope are constructed to be sensitive to certain wavelengths.

By comparing photometric observations from a variety of filters or instruments, astronomers can understand the broadband energy distribution of an object's observed flux (see Section 1.4). The continuum processes described in Chapter 1 each produce a SED with a different shape; comparing model SEDs with photometric measurements is one way to determine the types of emission mechanisms responsible for astronomical phenomena. In Chapter 3, we use a model stellar SED fit to observed photometric fluxes to determine the distance to the star HD 259440.

Spectroscopy is a more powerful method for studying stars. Light collected by the telescope is separated by wavelength before reaching the detector. Spectra of an astronomical object contain a wealth of information about the physical properties, geometry, and chemical composition of the source. As discussed in Chapter 1, the shapes of absorption lines in stellar spectra are strongly affected by the temperature and surface gravity of the star. Rotation rates, wind velocities, and wind structure can also be measured from spectral features. Thus, spectroscopy is a powerful tool for studying systems too distant to resolve with imaging techniques.

## **2.2 Optical Spectroscopy**

In order to obtain optical spectra of a star, we attach an instrument called a spectrograph to the telescope. Spectrographs typically consist of a mask with a slit in it, a collimating mirror, slots for filters, a diffraction grating, and a CCD. The image of the star is placed over the slit, and the light travels through the slit to hit the collimating mirror. This mirror refocuses the light into plane parallel waves that are incident on the diffraction grating. The diffraction grating will reflect light of different wavelengths at different angles. However, for any given wavelength, several angles exist at which light reflected off the grating will constructively interfere. Each of these angles represents a different order of diffraction. As a consequence of multiple orders of diffraction, the third order diffraction of light at wavelengths in the red part of the spectrum may cover the same range of angles as the second order diffraction of light in the blue range. Filters between the diffraction grating and the CCD can remove these higher order diffraction patterns to isolate the wavelength range of interest. Once the diffraction grating separates the light into a spectrum, a second mirror focuses the light onto the CCD chip.

In order to have a usable spectrum, the instrumental effects of the chip must be removed and the wavelength range and dispersion of the spectrum must be calibrated. During the course of a night of observing, we begin by taking bias images. These images read the charge pattern on the chip for an exposure time of zero. When the data are reduced, the bias images are averaged into a master bias that is subtracted from each observation. Next, we take a series of flat field images. Spectrographs are typically equipped with a quartz lamp which provides even illumination across the chip. The flat field images taken with this lamp are used to measure how the chip's response to light varies from pixel to pixel. The flat field images from each night are used to create a master flat by which the object and comparison spectra are divided. Finally, observations of stars are interspersed with comparison lamp spectra. These lamps are filled with a combination of gases for which the wavelengths of emission lines are well known. Light from the comparison lamp, typically a tube filled with a mixture of noble gases, is directed through the spectrograph to create an emission spectrum. Line lists and sample spectra are available on the observatory websites and are used in conjunction with the comparison spectra to calculate the wavelength dispersion,  $\delta\lambda$ , and the instrumental resolution of the spectrograph,  $\Delta\lambda$ . This calibration can change with temperature and telescope orientation, so these measurements often need to be repeated several times over the course of a night. Finally, the emission lines in the comparison spectra can be identified from catalogs, allowing the spectra to be wavelength calibrated.

We observed HD 259440 using the Kitt Peak National Observatory (KPNO) Coudé Feed (CF) telescope with the F3KB detector between 2008 October 17 and November 21. Each night, we used both blue and red spectral setups and generally obtained two spectra of HD 259440 in each. The blue spectra were taken using grating B in the third order with the 4–96 order sorting filter. These spectra have a resolving power  $R = \lambda/\Delta\lambda \sim 9500$ , cover



a wavelength range 4130 – 4570 Å, and have exposure times ranging from 20–30 minutes, giving a signal-to-noise ratio, S/N, of 50–140. The red spectra were obtained using grating B in the second order and the OG550 order sorting filter. They have  $R \sim 12000$ , span a wavelength range of 6400 – 7050 Å, and have exposure times of 20 minutes giving a S/N ratio of 100–250. ThAr (Thorium Argon) comparison lamp spectra were taken every 2–3 hours for wavelength calibrations. We zero corrected, flatfielded, and wavelength calibrated each spectrum using standard procedures in IRAF<sup>1</sup>. All spectra were interpolated to a common wavelength grid and corrected for heliocentric radial velocity variations. The blue spectra were written to a common log wavelength scale for radial velocity analysis. The spectra were rectified in IRAF using emission line free continuum regions.

Two blue optical spectra of HD 259440 were obtained at the KPNO 2.1m telescope using the GoldCam Spectrograph on 2008 December 12 – 13. Grating G47 was used in the second order with a CuSO<sub>4</sub> blocking filter and a slit width of 1.3" to achieve  $R \sim 2100 - 3100$ . These observations cover a wavelength range of 3700 – 4900 Å. The two spectra have exposure times of 15–20 minutes, resulting in a S/N ratio of 125–150. Comparison spectra were taken using a HeNeAr (Helium Neon Argon) lamp to wavelength calibrate the data. The spectra were zero corrected, flatfielded, and wavelength calibrated using the standard procedures in IRAF. We corrected the spectra for heliocentric radial velocity variations and rectified them in IRAF using emission line free continuum regions.

We also observed HD 259440 seven times, twice in 2009 March and five times in 2009

---

<sup>1</sup>IRAF is distributed by the National Optical Astronomy Observatory, which is operated by the Association of Universities for Research in Astronomy, Inc., under cooperative agreement with the National Science Foundation.

**Table 2.1:** Journal of Spectroscopy for HD 259440

UT Dates	Telescope	$\lambda$ Range (Å)	Resolving Power ( $\lambda/\Delta\lambda$ )	Grating/ Order	Filter	Number of Spectra
2007 Oct–2008 Feb	OHP 1.93m	3872 – 6943	40000	R2/50–88	...	16
2008 Oct 17–Nov 21	KPNO CF	4130 – 4570	9500	B/3	4-96	68
2008 Oct 17–Nov 21	KPNO CF	6400 – 7050	12000	B/2	OG550	62
2008 Dec 12–13	KPNO 2.1m	3700 – 4900	2100–3100	G47/2	CuSO <sub>4</sub>	2
2009 Mar	OHP 1.93m	3872 – 6943	40000	R2/50–88	...	2
2009 Oct	OHP 1.93m	3872 – 6943	40000	R2/50–88	...	5

October, with the SOPHIE cross-dispersed échelle spectrograph at the Observatoire Haute-Provence (OHP) 1.93m telescope<sup>2</sup>. These observations used the  $52.65 \text{ l mm}^{-1}$  R2 échelle grating to cover 39 orders in the high efficiency mode ( $R = 40000$ ) covering a wavelength range of 3872 – 6943 Å. The exposure times were between 45–90 minutes long, yielding a S/N of 80–220. Additional spectra were obtained from the OHP archive<sup>3</sup>, which were taken between 2007 October and 2008 February. These spectra had shorter exposure times of 5–15 minutes, and S/N as low as 40. The spectra were corrected for blaze, flatfielded, wavelength calibrated using ThAr lamp spectra taken within 2 hours of each observation, and corrected for heliocentric radial velocity variations. The observations of HD 259440 are summarized in Table 2.1 and their analysis is discussed in Chapter 3.

Spectra of LS 5039 were taken at the Cerro Tololo Inter-American Observatory (CTIO) 1.5m telescope between 2007 August and 2008 April in service mode. We used grating 47 in the second order, a 200 micron slit, the BG39 filter, and the Loral 1K CCD detector. Spectra were wavelength calibrated using HeAr comparison lamp spectra generally taken before and after each exposure. The observed wavelength region was about 4050–4700 Å,

<sup>2</sup>These observations were obtained by Michaël DeBecker, an author on Aragona et al. (2010) where these results are published.

<sup>3</sup>We would like to thank Yves Gallant, Bertrand Plez, and Guillaume Dubus for obtaining these archival spectra.

with  $R = 2500 - 3150$  across the chip.

For each night that we had service time available in fall 2007, we obtained 4-6 spectra, each with an exposure time of 30 minutes. During the spring of 2008, we obtained 2 spectra each night of observations, each of 22 minutes duration. Thus we obtained a total of 98 blue spectra of LS 5039. The images were zero corrected, flat fielded, and wavelength calibrated onto a log wavelength scale using standard procedures in IRAF, and all spectra were interpolated onto a common heliocentric wavelength grid. The spectra were rectified to a unit continuum using line-free regions.

Since the S/N ratio was somewhat low for our CTIO spectra of LS 5039, we chose to coadd pairs of consecutive spectra from each night. The total elapsed time during two consecutive observations is only one hour, about 1% of the orbital period, so coadding the spectra does not significantly affect the measured radial velocity,  $V_r$ . On two nights we collected an odd number of spectra, and in these cases the last spectrum of each set was examined individually. Therefore, we had 50 new spectra from which to obtain  $V_r$  measurements and improve the orbital elements.

Observations of the  $H\alpha$  line of LS 5039 were obtained using the Goodman High Throughput Spectrograph (GHTS) on the Southern Astrophysical Research Telescope (SOAR) from 2–4 June 2010. We used the 1200 l/mm grating in first order to obtain a wavelength range of 5550–6850 Å and  $R = 6000 - 7000$ . Exposure times ranged from 10 to 15 minutes. A flat field and a Ne (Neon) comparison lamp spectrum were taken after each exposure, and spectra were zero-corrected, flatfielded, and wavelength calibrated using standard procedures in IRAF. Our observations were taken between orbital phases 0.38–0.92, calculated using the orbital ephemeris from Aragona et al. (2009). A summary of the optical observations of LS 5039 are outlined in Table 2.2 and we present our analysis in Chapter 4.

**Table 2.2:** Journal of Spectroscopy for LS 5039

UT Dates	Telescope	$\lambda$ Range (Å)	Resolving Power ( $\lambda/\Delta\lambda$ )	Grating/ Order	Filter	Number of Spectra
2007 Aug–2007 Sep	CTIO 1.5m	4050 – 4700	2500–3150	47/2	BG39	44
2008 Apr	CTIO 1.5m	4050 – 4700	2500–3150	47/2	BG39	6
2009 Jun 2–Jun 4	SOAR 4.1m	5550 – 6850	6000–7000	1200 l/mm/1	–	14

## 2.3 Radio Observations

The Australia Telescope Compact Array (ATCA) is located about 25 miles west of Narrabri, Australia. It consists of six radio dishes arranged in roughly a straight line. The array includes several north-south tracks to allow two dimensional configurations for millimeter wavelength observing. The first five telescopes are contained in a 3 km strip, with the sixth telescope sitting another 3 km distant. This makes 6 km the longest baseline in the array. Each radio dish is 22 m in diameter.

In order to understand the nature of observations taken with radio interferometry, consider two antennas as illustrated in Figure 2.1. Light from a source will reach one antenna before the other, creating a lag time between the two observations. Flux incident on each telescope will induce a voltage in the detector, and the voltages from two detectors can be combined in a correlator. As the object moves across the sky, the geometry of the two telescopes in relation to the radio source will change: the light waves observed by the two antennas will move in and out of phase. This will create a sinusoidal variation in the output from the correlator, an effect called fringing. For an array of telescopes, the signal from any combination of two antennas can be measured. The output of each combination is called a visibility, and these measurements are mapped onto a space called the  $uv$ -plane. A fourier transform of these visibilities will convert them into fluxes in the plane of the sky. For a continuous distribution of baselines, the coverage of the  $uv$ -plane is perfect and will result

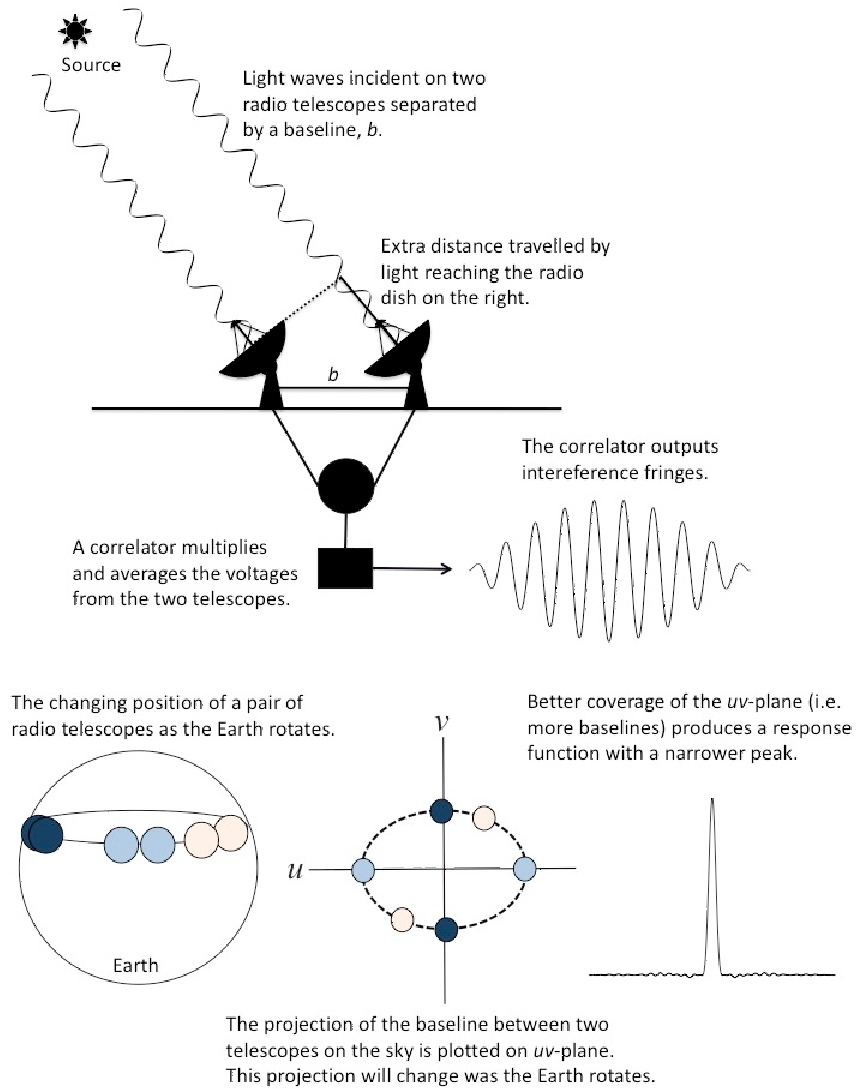


**Figure 2.1:** A schematic drawing showing how a radio interferometer functions. In the upper portion of the drawing, light from a source hits two antennas separated by a baseline,  $b$ . The light induces a voltage in each detector. The two voltages are multiplied and averaged in a correlator, producing interference fringes. The output of the interferometer can be improved by adding more baselines. This can be accomplished by either building more telescopes or using the rotation of the earth. The lower telescope shows the changing orientation of a pair of telescopes as the earth rotates. The projection of any pair of telescopes on the sky is plotted on the  $uv$ -plane. Over a twelve hour period of time, the projected baselines of the two telescopes will trace an ellipse on the  $uv$ -plane. More complete coverage of the  $uv$ -plane results in a narrower response function with smaller sidelobes.

in a perfect reconstruction of the radio sky. In reality, the number of baselines is finite and their distribution discrete, resulting in an imperfect fourier transform. If the array of telescopes observes a point source, the fourier transform of the visibilities will not result in a point source, but rather a two dimensional, sinusoidally varying distribution of flux that falls off exponentially across the field of view. Peaks in the flux outside the location of the original point source are referred to as sidelobes. The reduction process for radio data corrects for this imperfect fourier transform by removing flux from the sidelobes and returning it to the location of the point source.

Radio observations of LS 5039 were taken using ATCA between 2008 February and 2009 June. Each observation spanned a 2–3 hour period in total. Radio observations consist of a primary calibrator, a secondary calibrator, and the target. The primary calibrator is a bright, well observed object for which the radio properties are very well known. For our observations, we used the active galactic nucleus ICRF J193925.0-634245 as the primary calibrator. This object is observed at the beginning and/or end of the observation and is used to calibrate the gain, and in our case, the bandpass of the telescope. The gain describes the overall response of the telescope to radiation, while the bandpass quantifies how the detector response depends on frequency. The bandpass correction is applied by copying the calibrations from the primary calibrator to the secondary calibrator before performing the telescope calibration routine on the latter. The gain correction from the primary calibrator is used to scale the calibrated fluxes from the secondary calibrator. The secondary calibrator is a bright point source located near the target, in our case PMN J1825-1718. Observations of the secondary calibrator are interspersed with observations of LS 5039, allowing us to correct for changes in the telescope properties and atmospheric variations as the telescopes slew across the sky over the course of a full observation.

We obtained radio observations at four wavelengths: 3 cm, 6 cm, 13 cm and 20 cm. The set of detectors for the ATCA array could collect data either 3 cm and 6 cm or 13 cm and 20 cm simultaneously. We switched between the 3 cm/6 cm detector and the 13 cm/20 cm detector 2–3 times over each observation to ensure that the mid-exposure times at each wavelength were approximately the same. The data taken after June 1, 2009 (HJD = 2454983.31) were obtained using the new CABB back ends. With this instrumental set up, the 13 cm and 20 cm observations could not be taken simultaneously, and the observing cycle was split between 3 cm/6 cm, 13 cm, and 20 cm detector set-ups. The 20 cm are not presented in this dissertation, as the reduction process did not produce usable fluxes.

We used MIRIAD, the standard data reduction package for ATCA, to obtain a set of fluxes at each wavelength. The primary calibrator and secondary calibrator were examined and data contaminated with noise were removed. These calibrations were applied to LS 5039. MIRIAD creates an image of the source by taking a fourier transform of the observed power from each baseline. However, since the observations do not not comprise a continuous distribution of baselines, the results are imperfect. In order to fix this, we defined the location of bright sources in our field and used a module in MIRAD called *clean* to model the observed radio flux in each wavelength band. *Clean* places flux in each marked region to create a model of the sky brightness and correct for imperfections due to the incomplete coverage of the *uv*-plane. After each cycle of using *clean*, the *selfcal* module can be run to improve the calibration of the target data.

Our observations have limited *uv* coverage, and there are two fairly bright ( $\sim 400$  mJy) sources within half a 20 cm beamwidth to the west of LS 5039. Since LS 5039 is a point source to the ATCA and the position is very well known, we precisely defined the position of each source to create the region file used by *clean* and only used the long baselines

containing the 6 km antenna. The long baselines are not sensitive to diffuse emission from the other nearby sources, making the data easier to clean. The north-south elongation of the beam results in very little of the sidelobes from the bright sources to the west mingling with the LS 5039 sidelobes. In this way, we have been able to *clean* the source down to near theoretical rms levels despite the rather messy beam and northerly location (to ATCA) of the source. After five iterations of cleaning and self calibration, we created an image of the LS 5039 from which we obtained flux measurements. Our data reduction procedure is described more thoroughly in Appendix A.

## 2.4 Observations of $\gamma$ -ray binaries

Optical spectroscopic studies of  $\gamma$ -ray binaries yield valuable information, such as the orbital parameters of the system and the properties of the massive star. When the Be star HD 259440 was proposed to be the optical counterpart to the  $\gamma$ -ray source HESS J0632+057, it had not been studied extensively with optical spectroscopy. There is no clear evidence as to whether the star is part of a binary system. We obtained a large set of optical spectra in order to measure radial velocity shifts and perform a period search. These observations also allowed us to calculate detailed stellar parameters for the optical star, which aided us in placing constraints on the orbit. These results are presented in Chapter 3.

In the case of LS 5039, several papers had been published with discrepant orbital solutions (McSwain et al. 2004; Casares et al. 2005). We obtained further spectroscopic observations of the system to measure orbital radial velocity shifts and calculate a new orbital solution. Since the high energy emission in LS 5039 is the result of an interaction between the compact object and the stellar wind, we used  $H\alpha$  spectra to search for variations in the wind strength and evidence of structure. Furthermore, the nature of the compact object in



LS 5039 is still under debate. We obtained interferometric radio observations of LS 5039 with ATCA which provide photometry of the system at three different wavelengths. By searching this data set for correlations between the radio flux and spectral slope with orbital phase, we have studied the source of the radio emission. The results for LS 5039 are presented in Chapters 4 and 5.

# Chapter 3

## HD 259440: The Proposed Optical Counterpart of HESS J0632+057

### 3.1 Introduction

HD 259440 (=MCW 443, BD +05 1291), which lies between the edge of the Monoceros Loop supernova remnant and the star forming region of the Rosette Nebula, is classified as a B0pe star by Morgan et al. (1955) and a B0ne star by Turner (1976). Gutiérrez-Soto et al. (2007) assign it a projected rotational velocity,  $V \sin i$ , of  $430 \text{ km s}^{-1}$ . Otherwise, no detailed optical study of this star had been performed prior to our investigation (Aragona et al. 2010). HD 259440 has been proposed as the optical counterpart to a possible new  $\gamma$ -ray binary, HESS J0632+057 (Aharonian et al. 2007).  $\gamma$ -ray binaries are a subset of high-mass X-ray binaries which also emit radiation in the MeV-TeV range. The very high energy emission in such objects is expected to originate from an interaction between the massive star's wind and the compact object, although the physical processes that produce this radiation are under debate (see e.g. Dubus 2006).

Observations taken with the HESS telescope array between 2004 March and 2006

March revealed the TeV point source HESS J0632+057 (Aharonian et al. 2007). Hinton et al. (2009) followed up this detection with a 26 ks observation of the field using *XMM-Newton* on 2007 September 17. XMMU J063259.3+054801, the brightest source in the field, was positionally coincident with the HESS observation and centered on HD 259440. The X-ray source showed a gradual decline in flux over the course of the observation. X-ray observations obtained with *Swift* showed flux variations on a variety of timescales, from several days to a month (Falcone et al. 2010). While the data did not show a clear periodicity, Falcone et al. (2010) determined that periods of 35–40 days or  $\geq 54$  days are possibilities. HESS J0632+057 has also been associated with the *ROSAT* source 1RXS J063258.3+054857 and the EGRET source 3EG J0634+0521 (Aharonian et al. 2007; Skilton et al. 2009). The source has not yet been detected by *Fermi* (Abdo et al. 2010). A non-detection by VERITAS indicates a decrease in  $\gamma$ -ray flux from the time of the original HESS detection as well (Acciari et al. 2009). Radio observations revealed the source to have a mean flux of 0.3 mJy at 5 GHz, with variations on the timescale of a month (Skilton et al. 2009). The multiwavelength detections and the flux variations of this system are consistent with the class of  $\gamma$ -ray binaries.

At the time of our study, six systems were known or proposed  $\gamma$ -ray binaries: LS 5039, LS I +61 303 (Abdo et al. 2010), PSR B1259–63 (Aharonian et al. 2005b), Cyg X-1 (Albert et al. 2007), Cyg X-3 (Abdo et al. 2009), and HESS J0632+057 (see above). Optical spectroscopy can provide useful information about the stellar properties and orbital parameters of these systems, which aid in the analysis of observations at other wavelengths. We have undertaken a study of the optical properties of HD 259440 to complement ongoing work in X-ray,  $\gamma$ -ray, and radio to determine the nature of this system.

## 3.2 Constraints on the Orbital Period of HD 259440

We performed a cross-correlation of the He I  $\lambda 4471$  line in our CF data with a mean spectrum from that run to search for radial velocity,  $V_R$ , shifts. Due to the low S/N of those spectra, the  $V_R$  measurements had a standard deviation,  $\sigma_{RV}$ , of  $20.1 \text{ km s}^{-1}$ , and no significant shifts in  $V_R$  were found. We also did not detect any gradual trend of increasing or decreasing  $V_R$ . The CF dataset rules out orbital periods of  $\sim 35 \text{ d}$  or less.

The He I  $\lambda 5876$  line in the échelle spectra from OHP was also examined for  $V_R$  variations, of which the results are presented in Table 3.1. These measurements had a  $\sigma_{RV}$  of  $6.7 \text{ km s}^{-1}$ , which is close to the precision that we would expect to achieve due to the natural line width and line shape. Again, no significant shifts in  $V_R$  were detected in this set of observations. Due to the significant instrumental differences and wavelength coverage between the CF, KPNO 2.1m, and OHP runs, we hesitate to combine the  $V_R$  over these combined datasets to investigate  $V_R$  shifts. Crampton (1968) gives a radial velocity measurement of  $7.6 \text{ km/s}$ ; however, the measurement is flagged for poor quality. Thus we use only the sparsely sampled OHP spectra to constrain the orbital period further.

We cannot rule out the possibility that HD 259440 is a binary until we determine the probability that the system has an orbit with  $V_R$  shifts too small for our observations to detect. We use a method similar to that outlined in Garmany et al. (1980). For a binary system, the mass function of the primary is

$$f(m) = \frac{M_\star \sin^3 i}{q (1 + q)^2} = 1.0355 \times 10^{-7} K_\star^3 P (1 - e^2)^{3/2} \quad (3.1)$$

with

$$q = \frac{M_\star}{M_X} \quad (3.2)$$

where  $M_\star$  is the mass of the optical star in solar units,  $M_X$  is the mass of the compact

**Table 3.1:** OHP  $V_R$  Measurements of HD 259440

UT Date	Mid-exposure HJD-2450000	$V_R$ km s <sup>-1</sup>
2007 Oct 02	4375.1714	43.78
2007 Oct 22	4395.1686	47.55
2007 Oct 22	4395.1744	46.69
2007 Nov 01	4405.1763	47.96
2007 Nov 02	4406.1672	46.48
2007 Nov 03	4407.1905	44.90
2007 Nov 04	4408.1886	47.04
2007 Nov 05	4409.1474	41.74
2007 Nov 10	4414.0348	47.81
2007 Dec 27	4461.9402	41.99
2007 Jan 19	4484.8059	38.06
2008 Jan 21	4486.8267	28.88
2008 Feb 06	4502.9462	30.41
2008 Feb 12	4508.8925	36.28
2008 Feb 19	4515.8693	31.02
2008 Feb 25	4521.8527	27.09
2009 Mar 10	4900.8138	33.11
2009 Mar 14	4904.7721	45.97
2009 Oct 13	5117.6426	39.85
2009 Oct 15	5119.6701	43.57
2009 Oct 17	5121.6604	41.69
2009 Oct 27	5131.6605	42.96
2009 Oct 28	5132.6867	47.04

object in solar units,  $K_*$  is the velocity semi-amplitude of the optical star in km s<sup>-1</sup>,  $P$  is the orbital period in days,  $e$  is the orbital eccentricity, and  $i$  is the system inclination angle. If we knew the orbital parameters for the system, plotting the radial velocity of the optical star as a function of orbital phase would result in a distorted sinusoid. The velocity semi-amplitude is half the amplitude of this curve. Assuming an upper limit for  $K_*$  of  $2\sigma_{RV}$ , we can find the upper limit for  $i$  at a given value of  $P$  at which we would fail to detect  $V_R$

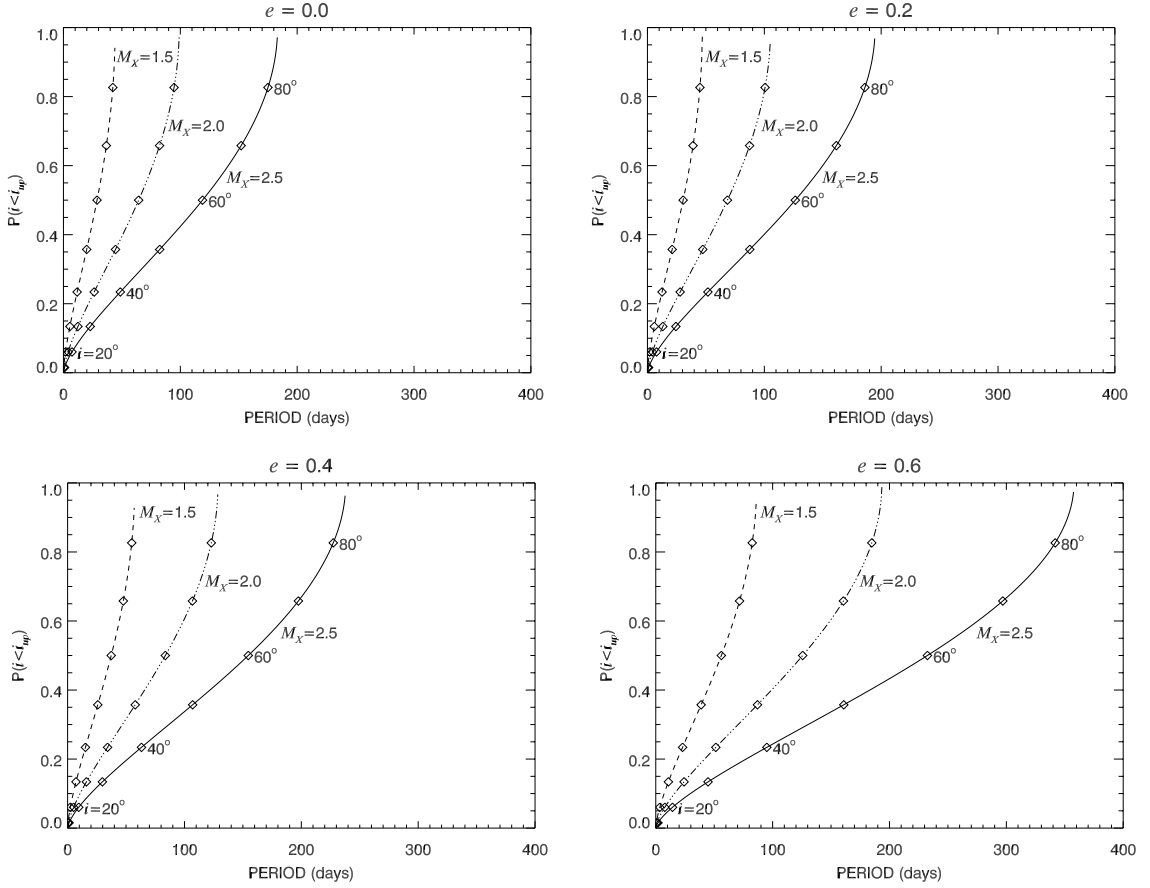


**Figure 3.1:** Probability of having missed the binary companion because of a too low inclination angle as a function of the orbital period, for eccentricities equal to 0.0, 0.2, 0.4, and 0.6, respectively. In each panel, secondary masses of  $1.5 M_{\odot}$ ,  $2.0 M_{\odot}$  and  $2.5 M_{\odot}$  have been assumed. The diamonds indicate inclinations from  $10^{\circ}$  to  $80^{\circ}$ , spaced at intervals of  $10^{\circ}$ .

variations in our dataset:

$$\sin i \leq 9.392 \times 10^{-3} \sigma_{RV} \left( \frac{Pq(1+q)^2(1-e^2)^{3/2}}{M_{\star}} \right)^{1/3}. \quad (3.3)$$

If we assume a random distribution of orbital inclinations, the probability that  $V_R$  is lower than our detection limit is

$$P(i < i_{up}) = \int_0^{i_{up}} \sin i \, di = 1 - \cos i_{up}. \quad (3.4)$$

We used the lower  $\sigma_{RV}$  obtained from the OHP spectra and our measured mass of the Be star,  $M_\star = 16 M_\odot$  (see Section 3.3). Secondary masses of 1.5, 2.0, and 2.5  $M_\odot$ , consistent with a low mass companion, and eccentricities of 0.0, 0.2, 0.4, and 0.6 were considered. The results are plotted in Figure 3.1. For a compact companion of 1.5  $M_\odot$ , we would be unable to detect  $V_R$  shifts for an orbital period greater than 50 days. The chance of detection improves for higher values of the secondary mass. However, for a 100 day orbit, there is still only a 50% probability that the system will have an inclination favorable for detecting  $V_R$  shifts in our data. The chances of detection also decrease with orbital eccentricity. Our method does not take into account that we would need to observe the system close to periastron to detect the radial velocity shifts for an eccentric orbit. The system would only spend a small fraction of its orbit with  $V_R$  shifts high enough for us to detect, decreasing our chances of observing  $V_R$  shifts in systems of higher eccentricity. Therefore, we cannot rule out HD 259440 as a binary system with a long period.

### 3.3 Stellar Parameters of HD 259440

Accurately determining the stellar parameters of HD 259440 is a challenging process due to the prevalence of emission features in the spectra. In order to minimize the impact of the disk emission on our analysis, we chose to focus on the He I and H Balmer lines with  $\lambda \leq 4000 \text{ \AA}$ , where the lines are predominantly in absorption. This approach required our analysis to use the lower resolution KPNO 2.1m telescope spectra, as these covered a broader wavelength range than the KPNO CF data (Figure 3.2). In order to improve the S/N, we created a mean spectrum from the two observations. We then compared this spectrum to *TLUSTY* OSTAR2002 (Lanz & Hubeny 2003) and *BSTAR*2006 (Lanz & Hubeny 2007) model grids, corrected for instrumental broadening, to obtain values for the effective

temperature,  $T_{\text{eff}}$ , surface gravity,  $\log g$ , and  $V \sin i$  of the optical star.

The Tlusty BSTAR2006 and OSTAR2002 model grids are publicly available synthetic spectra and SEDs generated from model stellar atmospheres. These models assume a plane-parallel stellar atmosphere. The BSTAR2006 models are available with temperatures ranging from 15000 K to 30000 K, with a grid spacing of 1000 K, and  $\log g$  ranging from 1.75 to 4.75 where  $g$  is the surface gravity of the star in  $\text{cm s}^{-2}$ , with a grid spacing of 0.25. The OSTAR2002 models exist for temperatures between 27500 K and 55000 K with a grid spacing of 2500 K. These models are available for  $\log g$  between 3.0 and 4.75, with a grid spacing of 0.25. The OSTAR2002 models assume a microturbulence velocity of  $10 \text{ km s}^{-1}$ , while the BSTAR2006 models assume a microturbulence velocity of  $2 \text{ km s}^{-1}$ . We used models with solar abundances.

Initially, we tried fitting the mean spectrum of HD 259440 over the 3750–3950 Å range for  $T_{\text{eff}}$ ,  $\log g$ , and  $V \sin i$  simultaneously.  $T_{\text{eff}}$  was varied between 20000 K and 40000 K in increments of 1000 K (2500 K) to match the spacing of the BSTAR2006 (OSTAR2002) grid. We varied  $\log g$  from 2.50 to 4.75 (3.0 to 4.75) in increments of 0.25 according to the BSTAR2006 (OSTAR2002) grid spacings. We also increased  $V \sin i$  from  $300 \text{ km s}^{-1}$  to  $500 \text{ km s}^{-1}$  in steps of  $50 \text{ km s}^{-1}$ . We computed the  $\chi^2$  value for each combination of  $T_{\text{eff}}$ ,  $\log g$ , and  $V \sin i$ . However, none of the trials produced a satisfactory fit to the observed spectrum. The best fits from the two model grids produced divergent solutions for  $T_{\text{eff}}$  and  $\log g$ . Furthermore, a visual inspection comparing the model to the observed spectrum revealed the poor quality of these fits and they could not be used to constrain a  $T_{\text{eff}}$  and  $\log g$  for the system.

The unusually shallow yet broad absorption lines seen in the spectra of HD 259440 are indicative of flux dilution, in that the continuum emission and scattering from the disk



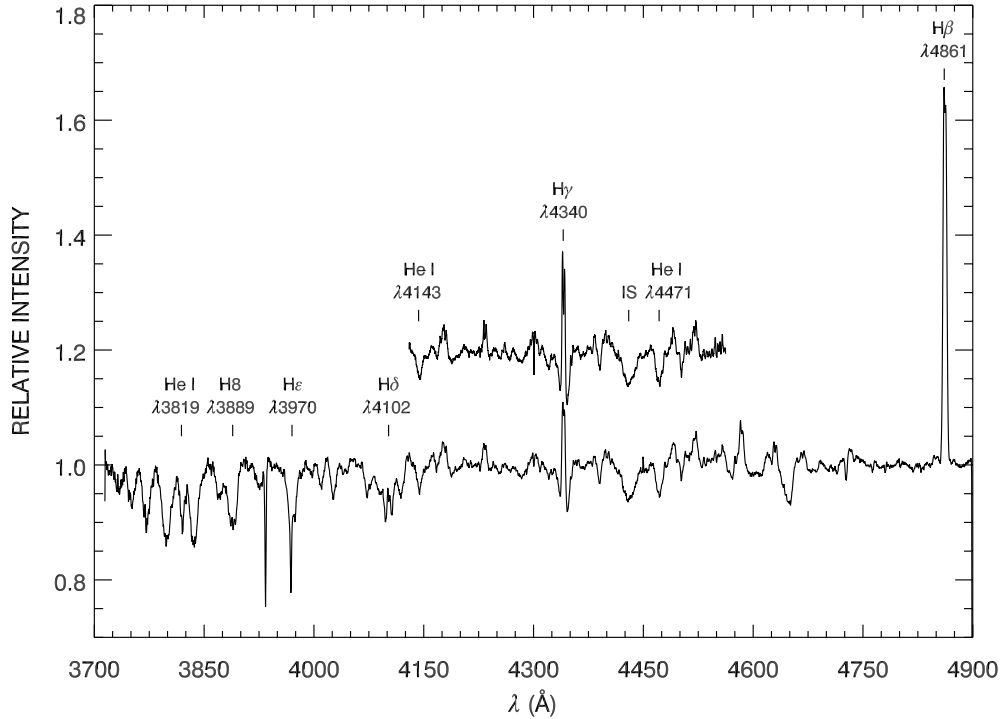


**Figure 3.2:** The mean spectra from the KPNO 2.1m (bottom) and CF (top) telescopes are plotted for comparison. The CF spectrum is offset by 0.2 for clarity.

have effectively decreased the relative strength of absorption lines in the rectified spectra. In order to rectify a spectrum, a function is fit to the level of the continuum with respect to wavelength and the spectrum is divided by this function at each wavelength. The result is a rectified spectrum with the continuum normalized to a value of 1 at each wavelength. The total observed flux is the sum of the flux from the disk,  $F_{disk}$ , and the star,  $F_{star}$ . Over a small wavelength range, we can assume a constant ratio  $N = F_{disk}/F_{star}$ . Using this assumption, we can correct for the disk continuum emission by adjusting the rectified spectrum:

$$F_{R,star} = F_R(1 + N) - N \quad (3.5)$$

where  $F_R$  is the rectified observed spectrum and  $F_{R,star}$  is the rectified spectrum of the

star corrected for the disk continuum emission. Since the relative disk flux is unknown, we adjusted the observed spectrum for values of  $N = 0.1 - 0.9$  and repeated the fitting procedure at each value.

The absorption lines in the spectrum of HD 259440 are fairly broad, so we expect the star to have a high rotational velocity. At all values of  $T_{\text{eff}}$  and  $\log g$ , a  $V \sin i$  of  $500 \text{ km s}^{-1}$  provided the best agreement with the line profiles. Therefore, we chose to fix  $V \sin i$  at this value. We then repeated our fits using the OSTAR2002 and BSTAR2006 models over the  $3750\text{--}3950 \text{ \AA}$  region. At each  $N$ , we determined the best fit  $T_{\text{eff}}$  and  $\log g$  by minimizing the  $\chi^2$  from the model fits. Our quoted errors for  $T_{\text{eff}}$  and  $\log g$  represent the  $1\sigma$  significance levels from our best fit. For values of  $N$  between 0.0 and 0.4,  $T_{\text{eff}}$  and  $\log g$  are not well constrained, but the fit quality and agreement between the BSTAR2006 and OSTAR2002 models improve significantly for higher values of  $N$ . Therefore, we chose to focus on the results with  $N \geq 0.5$ , which are summarized in columns 1–5 of Table 3.2.

**Table 3.2: Stellar Parameters of HD 259440**

$N$	$T_{\text{eff}}$ (K)	$\Delta T_{\text{eff}}$ (K)	$\log g$ ( <i>dex</i> )	$\Delta \log g$ ( <i>dex</i> )	$M_{\star}$ ( $M_{\odot}$ )	$\Delta M_{\star}$ ( $M_{\odot}$ )	$R_{\star}$ ( $R_{\odot}$ )	$\Delta R_{\star}$ ( $R_{\odot}$ )	$V_{\text{crit}}$ ( $\text{km s}^{-1}$ )	$\theta_D$ ( $\mu\text{as}$ )	$\Delta \theta_D$ ( $\mu\text{as}$ )	$d$ (kpc)	$\Delta d$ (kpc)
<b>BSTAR2006 Model Fitting Results</b>													
0.5	30,000	+1,000 -7,000	3.75	+0.90 -0.85	19.0	+1.5 -8.2	9.6	+44.8 -6.9	501	25.1	$\pm 1.1$	1.78	$\pm 0.08$
0.6	29,000	+4,000 -3,000	3.75	+0.80 -0.30	17.6	+6.7 -4.0	9.3	+5.9 -6.4	491	25.2	$\pm 1.2$	1.71	$\pm 0.09$
0.7	30,000	+3,000 -5,000	4.00	+0.50 -0.50	16.0	+3.6 -5.0	6.6	+8.1 -3.3	555	23.7	$\pm 1.1$	1.30	$\pm 0.06$
0.8	30,000	+2,000 -5,000	4.00	+0.50 -0.55	16.0	+2.5 -5.0	6.6	+9.7 -3.3	555	23.1	$\pm 1.1$	1.33	$\pm 0.06$
0.9	29,000	+2,000 -6,000	4.00	+0.45 -0.60	14.5	+2.9 -5.3	6.3	+7.7 -2.9	541	23.4	$\pm 1.2$	1.26	$\pm 0.07$
<b>OSTAR2002 Model Fitting Results</b>													
0.5	30,000	+1,000 -7,000	4.00	+0.65 -1.10	16.0	+1.4 -6.8	6.6	+47.8 -3.9	555	24.5	$\pm 1.0$	1.25	$\pm 0.05$
0.6	30,000	+3,000 -4,000	4.00	+0.55 -0.55	16.0	+3.6 -4.4	6.6	+9.7 -3.5	555	23.7	$\pm 0.9$	1.30	$\pm 0.05$
0.7	30,000	+3,000 -5,000	4.00	+0.50 -0.50	16.0	+3.6 -5.0	6.6	+8.1 -3.3	555	23.0	$\pm 0.9$	1.34	$\pm 0.05$
0.8	27,500	+4,500 -2,500	3.75	+0.60 -0.30	15.3	+7.2 -2.8	8.6	+5.5 -5.6	476	24.5	$\pm 1.2$	1.64	$\pm 0.08$
0.9	27,500	+3,500 -4,500	4.00	+0.45 -0.60	13.2	+4.2 -4.0	6.0	+9.4 -2.8	529	24.1	$\pm 1.3$	1.16	$\pm 0.06$

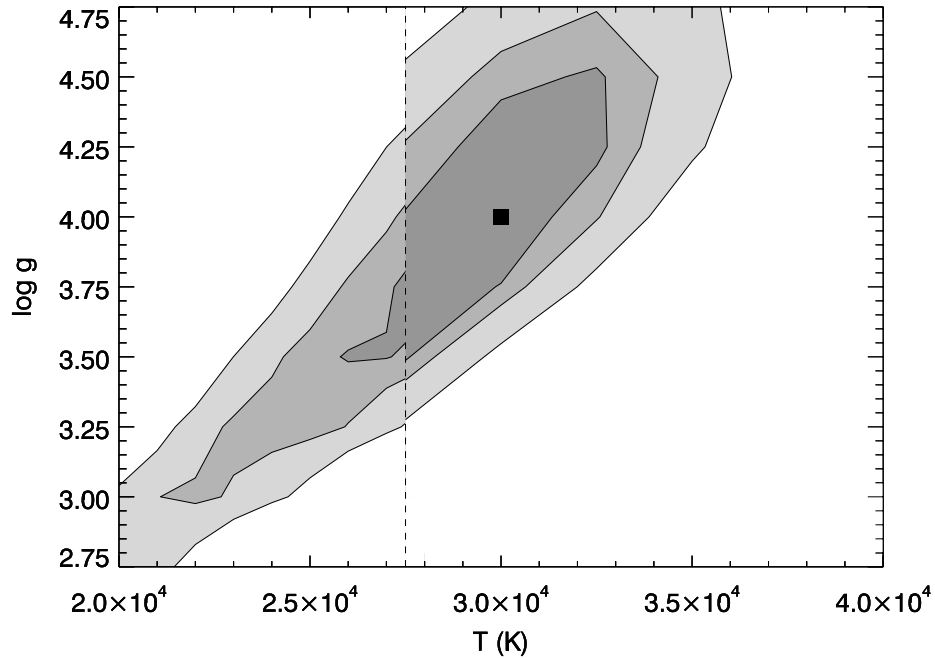


**Figure 3.3:** A contour plot of the  $1\sigma$ ,  $2\sigma$ , and  $3\sigma$  errors from the spectral fits using  $N = 0.7$  and  $V \sin i = 500 \text{ km s}^{-1}$ . The discontinuity between the OSTAR2002 and BSTAR2006 models is marked by the vertical dashed line. The square represents the model with the lowest  $\chi^2$  value for both model fits.

A contour plot illustrating the  $1\sigma$ ,  $2\sigma$ , and  $3\sigma$  significance errors for the combined OSTAR2002 and BSTAR2006 model fits in the  $N = 0.7$  case is shown in Figure 3.3. As can be seen from this figure and Table 3.2, the best values of  $T_{\text{eff}}$  for both the OSTAR2002 and BSTAR2006 models lie near the boundaries of the model grids. Furthermore, the  $1\sigma$  significance contours are not closed at the boundary between the models. Therefore, we determined the lower limit of  $T_{\text{eff}}$  from the  $1\sigma$  contour of the BSTAR2006 models and the upper limit from the  $1\sigma$  contour of the OSTAR2002 models.

A Tlusty BSTAR2006 model spectrum with  $T_{\text{eff}} = 30000 \text{ K}$ ,  $\log g = 4.0$ , and  $V \sin i = 500 \text{ km s}^{-1}$  plotted against the mean spectrum of HD 259440 with  $N = 0.7$  is shown in Figure 3.4. We generally find good agreement between the model and observed spectrum

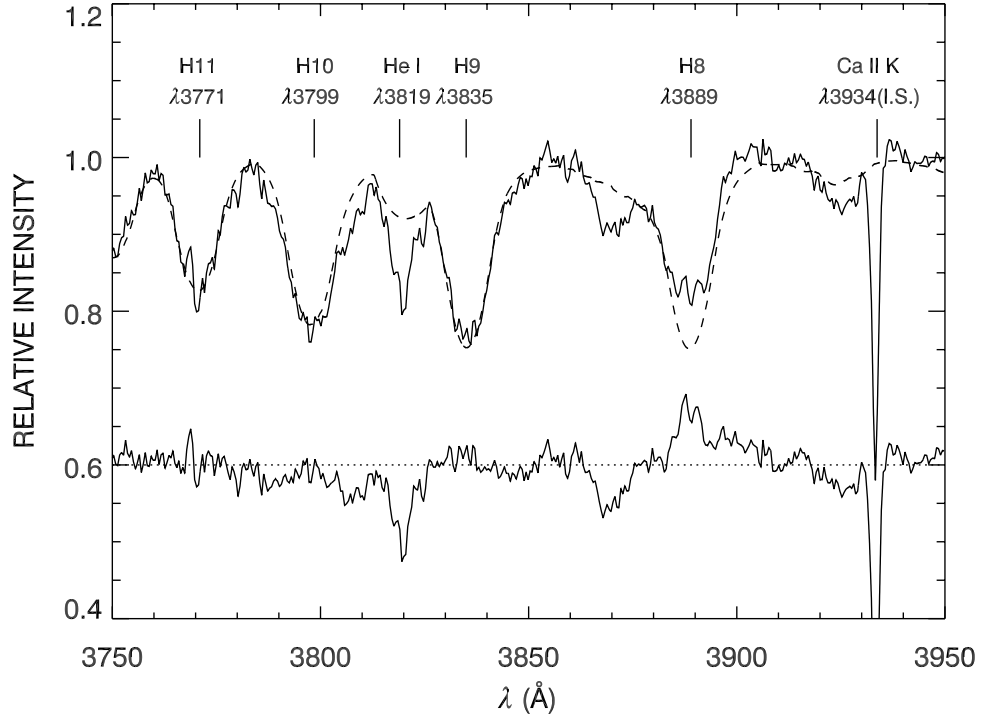


**Figure 3.4:** The mean KPNO 2.1m spectrum, adjusted for  $N = 0.7$ , is shown as a solid line. The dashed line shows the Tlusty BSTAR2006 model spectrum with  $T_{\text{eff}} = 30000$  K,  $\log g = 4.0$ , and  $V \sin i = 500$  km s $^{-1}$ . The residuals from the fit are plotted below the spectrum, shifted by 0.6 for easier comparison.

in the H Balmer lines, although the He I  $\lambda 3819$  line appears stronger than all of our model fits. HD 259440 has been classified as a star with peculiar abundances. It was marked as nitrogen rich by Turner (1976) and may also be a helium-strong star. We cannot distinguish significant differences between the model fits with different values of  $N$ , which remains a source of ambiguity in determining the physical parameters of this system.

As a further test of the validity of the fit, we compared the model fits to one of the few other photospheric absorption lines in our blue spectra, the flux-corrected He I  $\lambda 4471$  line. Figure 3.5 shows good agreement over the core of the line with the BSTAR2006 fit

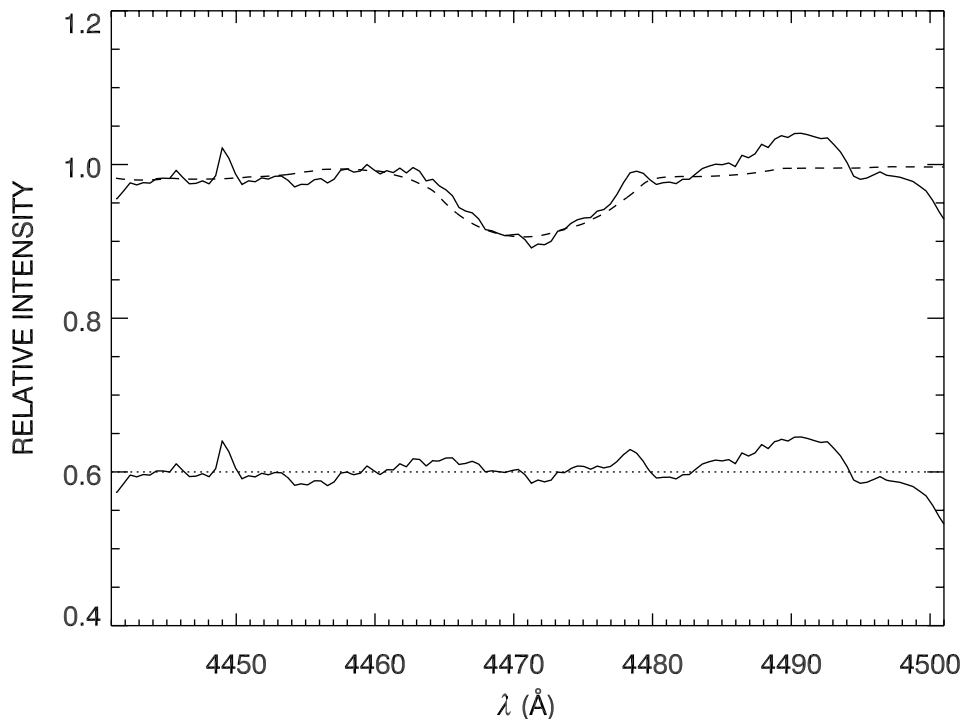


**Figure 3.5:** The He I  $\lambda 4471$  line from the mean KPNO 2.1m spectrum is shown in the same format as Figure 3.4.

and  $N = 0.7$ . There may be some excess emission in the line wings from the higher velocity regions of the disk, narrowing the line slightly. Using the OSTAR2002 fits, the flux-corrected He I  $\lambda 4471$  line is again stronger than the model, a result of the difference in microturbulent velocity between the two sets of models. Since HD 259440 may be helium strong, the fit of the He I  $\lambda 4471$  line does not help constrain the best fit any further. The quality of the fits for the values of  $N$  considered in this paper were equally good, so we also cannot constrain the flux contribution from the disk any further.

We determined the mass,  $M_*$ , and radius,  $R_*$ , of the star using our best fit values for  $T_{\text{eff}}$  and  $\log g$  and interpolating between the evolutionary tracks of Schaller et al. (1992).

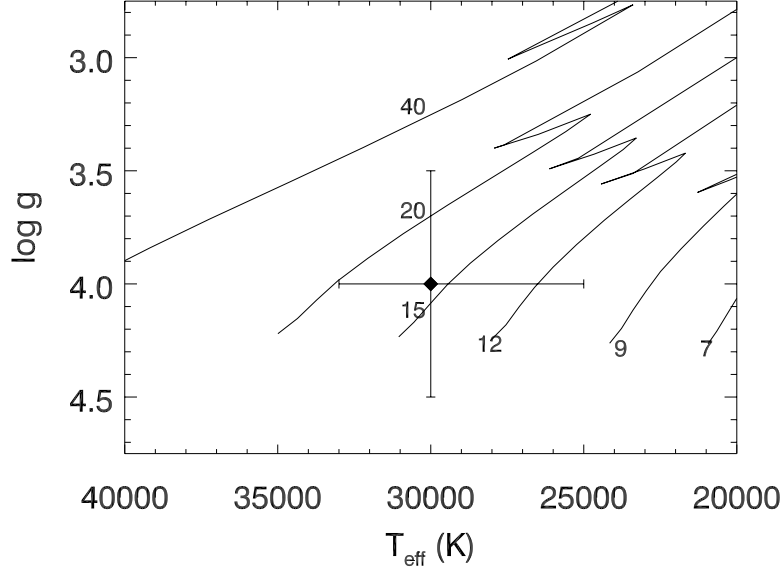


**Figure 3.6:** Evolutionary tracks from Schaller et al. (1992). The initial mass for each track is indicated by numbers 7 through 40. Our best fit value for  $T_{\text{eff}}$  and  $\log g$  in the  $N = 0.7$  case is plotted as a diamond with error bars.

Figure 3.6 displays a sample for the  $N = 0.7$  case. The evolutionary tracks were published for non-rotating stars with solar metallicity and masses ranging from  $0.8$  to  $120 M_{\odot}$ . The errors for  $M_{\star}$  were calculated using the best value of  $\log g$  and using the  $1\sigma$  limits for  $T_{\text{eff}}$ , while the errors for  $R_{\star}$  were calculated using the best fit values for  $T_{\text{eff}}$  and using the  $1\sigma$  limits for  $\log g$ . Our measurements of  $M_{\star}$  and  $R_{\star}$  are presented in columns 6–9 of Table 3.2. The rapid rotation of HD 259440 may result in an underestimation of the mass and introduce an additional systematic error into our measurements. Ekström et al. (2008) calculated evolutionary tracks for rapidly rotating stars. Comparing these models to the tracks from Schaller et al. (1992), we conclude that any discrepancy in the mass of HD 259440 would be about  $5 M_{\odot}$ . We also calculated the critical velocity,  $V_{\text{crit}}$ , at the stellar

equator for each  $N$ . Since HD 259440 is a rapid rotator, the stellar radius at the equator is  $1.5R_*$  in the standard Roche model. Therefore,

$$V_{crit} = \sqrt{\frac{GM_*}{1.5R_*}}. \quad (3.6)$$

The results are listed in column 10 of Table 3.2. These results indicate that HD 259440 is rotating close to  $V_{crit}$ , which is plausible for Be stars and thought to contribute to the formation of the circumstellar disk (Townsend et al. 2004).

### 3.4 Spectral Energy Distribution of HD 259440

We compared the observed SED of HD 259440 with the model SEDs from the Tlusty BSTAR2006 and OSTAR2002 models to measure the distance to the star. We obtained ultraviolet broadband photometric fluxes from Wesselius et al. (1982), Johnson  $UBV$  magnitudes from Neckel & Chini (1980), Johnson  $I$  magnitude from Droege et al. (2007), 2MASS  $JHK_S$  magnitudes from Skrutskie et al. (2006), and mid-infrared fluxes from Egan et al. (2003). The Johnson magnitudes were converted to fluxes according to Bessel et al. (1998), while the 2MASS photometry were converted to fluxes using Cohen et al. (2003).

The Tlusty model spectra were binned in 50 Å bins to eliminate small scale line features and simplify comparison with the observed fluxes. The SEDs must be corrected for reddening and extinction. The interstellar medium affects light passing through it differently depending on wavelength. Blue light passing through this material is attenuated more than red light, causing the observed the light from an object to appear redder in observations from earth than at the source. This effect is called reddening. The total extinction,



$A_V$ , describes the attenuation of light from the source in the photometric V band, and selective extinction is defined as  $R = \frac{A_V}{E(B-V)}$  (Krelowski & Papaj 1993). A reddening of  $E(B - V) = 0.85$  (Friedemann 1992) and selective extinction of  $R = 3.1$  were applied to the model SEDs using the extinction model of Fitzpatrick (1999). The observed photometric fluxes were corrected for disk emission using each value of  $N$  and compared with the best fit OSTAR2002 and BSTAR2006 models.

In our spectral fitting, we assumed that the disk flux ratio  $N$  is constant over a small wavelength range. Therefore, we compared the observed fluxes between 3000 – 5000 Å, corrected for  $N$ , to the model SEDs to determine the angular radius (or size),  $\theta_R$ :

$$\theta_R = \frac{R_\star}{d} = \sqrt{\frac{F_{\star,obs}}{F_{\star,surf}}} = \sqrt{\frac{F_{tot,obs}}{F_{\star,surf}(1 + N)}} \quad (3.7)$$

where  $F_{\star,obs}$  is the observed flux produced by the star,  $F_{\star,surf}$  is the flux at the stellar surface,  $F_{tot,obs}$  is the combined flux of the star and disk, and  $d$  is the distance to the star. Using our derived  $R_\star$  with the calculated  $\theta_R$ , we find that HD 259440 lies within the distance range  $d = 1.1 - 1.7$  kpc. The errors in the distance presented in Table 3.2 give the standard deviation between the model SED and the broadband photometric flux points in the 3000 – 5000 Å range. As the quality of all our best fits were similar for values of  $N$  between 0.5 and 0.9, the actual error in  $d$  is more accurately reflected by the range of values presented. HD 259440 is listed by Voroshilov et al. (1985) as a member of the open cluster NGC 2244. A recent study by Bonatto & Bica (2009) places the cluster at  $1.6 \pm 0.2$  kpc from the Sun, a value consistent with previous studies and our measurements for HD 259440 (Ogura & Ishida 1981; Pérez et al. 1987; Park & Sung 2002).

We expect to see exorbitant infrared emission in the SED of HD 259440 due to the nearly edge-on circumstellar disk. This infrared excess can clearly be seen in Figure 3.7, which shows the observed broadband photometric fluxes with the BSTAR2006 model SED

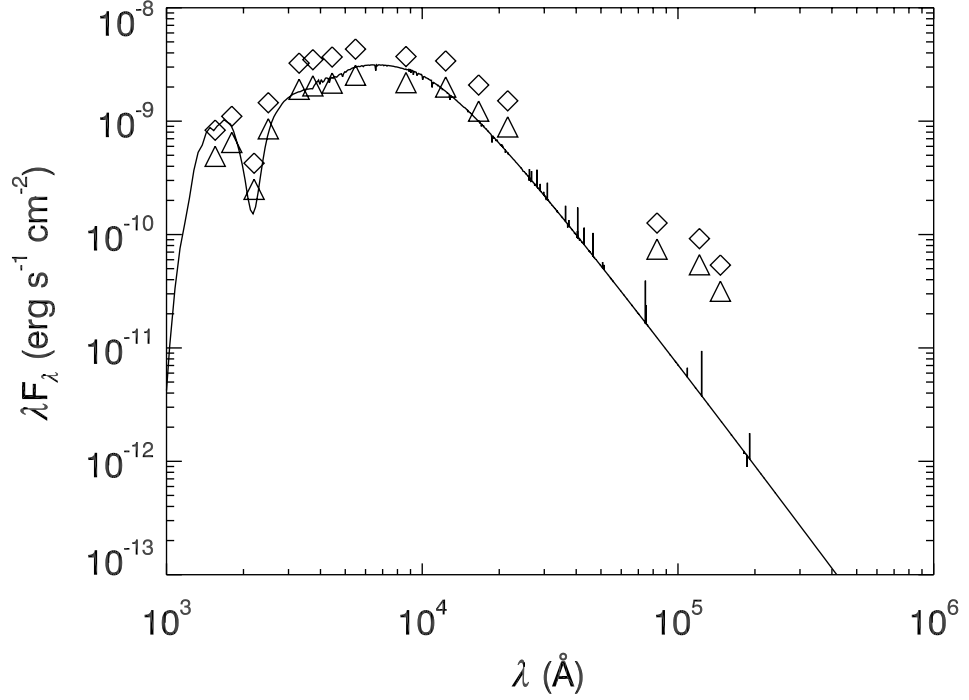


**Figure 3.7:** The TruStar2006 model SED normalized to  $\theta_R = 24.3 \mu\text{as}$  ( $1.13 \times 10^{-10}$  radians) is plotted as a solid line. The diamonds indicate the observed broadband photometric fluxes. The triangles represent the estimated stellar flux assuming  $N = 0.7$ .

for  $T_{\text{eff}} = 30000 \text{ K}$ ,  $\log g = 4.0$ ,  $N = 0.7$ , and  $d = 1.30 \text{ kpc}$ . At blue optical wavelengths, the disk contributes  $\sim 0.7F_{\star}$ . In the mid-infrared, the disk continuum emission is  $\sim 22$  times the flux of the star.

# Chapter 4

## Optical Spectroscopic Studies of LS 5039

### 4.1 Introduction

LS 5039 is a HMXB that consists of a massive, main sequence primary (ON6.5 V((f)) spectral type; McSwain et al. 2004) and a compact companion in a tightly bound, eccentric orbit (Casares et al. 2005). Optical and ultraviolet spectra of the system reveal nitrogen enrichment and carbon depletion at the surface of the O star, a sign of prior mass transfer that inverted the binary mass ratio before the supernova occurred (McSwain et al. 2004). The binary remained bound and was ejected from the Galactic plane within the past 1.1 Myr in an asymmetric supernova explosion that imparted a runaway velocity of about  $150 \text{ km s}^{-1}$  to the system (Ribó et al. 2002; McSwain et al. 2004).

As a HMXB, LS 5039 is quite inconspicuous with a relatively constant, low X-ray flux and hard spectrum; it does not experience dramatic X-ray flares or state changes that are seen in most other HMXBs. However, it is an unusually bright radio source for a HMXB (Ribó et al. 1999). The system distinguished itself when it was first noted as a probable  $\gamma$ -ray source by Paredes et al. (2000) since it is the only simultaneous X-ray and radio emitter inside the 95% confidence contour of the EGRET source 3EG J1824–1514. Its

bright and hard  $\gamma$ -ray spectrum suggested that it might be observable by ground-based atmospheric Čerenkov telescope arrays, and indeed it was detected with energies  $> 0.1$  TeV by the HESS array (Aharonian et al. 2005b). The identification of the  $\gamma$ -ray source with the optical star LS 5039 was strengthened by the  $\gamma$ -ray variability over the 4 day orbital period (Aharonian 2006). The X-ray flux is also modulated with the orbital period (Bosch-Ramon et al. 2005, 2007; Takahashi et al. 2008).

## 4.2 Calculating the Orbital Parameters of LS 5039

Our orbital solution for LS 5039 has been published by Aragona et al. (2009). To determine the orbital parameters of LS 5039, we used the optical spectra obtained with the CTIO 1.5m telescope, described in Chapter 2. The spectra from August 29, 2007 were taken near the time of inferior conjunction, when the compact companion is in front of the O star from our point of view, and thus showed the least variation in  $V_R$ . These six spectra were averaged to produce a reference spectrum, shown in Figure 4.1. We examined five lines in each spectrum:  $H\gamma$ ,  $H\delta$ , He II  $\lambda\lambda 4200, 4542$ , and He I  $\lambda 4471$ . The spectra also recorded the strong He II  $\lambda 4686$  line, but a bad column on the chip interfered with measuring reliable  $V_R$  from this line. We performed a cross correlation between each spectrum and the reference spectrum to obtain its relative  $V_R$ , and then we used the mean  $V_R$  from a parabolic fit of the line cores in the reference spectrum to find its absolute  $V_R$ .

The period of the system was obtained using the discrete Fourier transform and CLEAN deconvolution program of Roberts, Lehár, & Dreher (1987; written in IDL by A. W. Fullerton). The  $V_R$  from our observations was combined with the mean values from all lines measured by McSwain et al. (2001), McSwain et al. (2004), and Casares et al. (2005). The  $V_R$  measurements of Casares et al. (2005) indicate a value for the center of mass velocity,

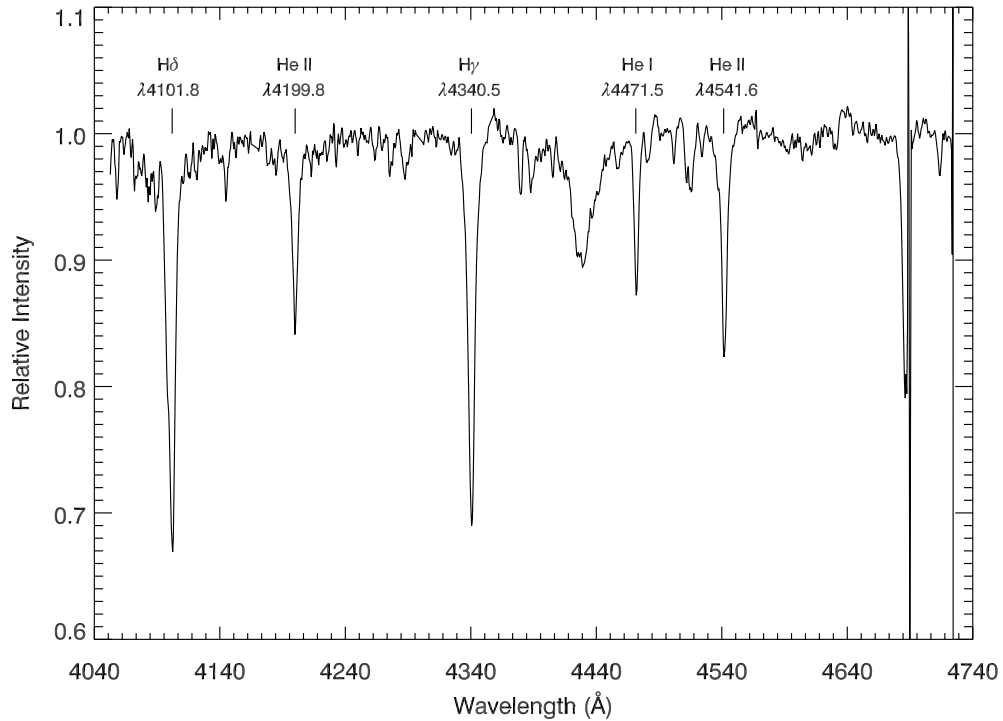


**Figure 4.1:** The mean spectrum of LS 5039 from the night of 2007 August 29, taken near the time of inferior conjunction of the optical star. We used this mean spectrum as a reference to determine the relative  $V_R$  by cross correlation with each spectrum of LS 5039.

$\gamma$ , that is systematically higher than our data sets by  $7.0 \text{ km s}^{-1}$ , so we subtracted this value from their measurements. No significant difference is found between the  $V_R$  data presented here and past measurements obtained by our group. We used all of the available  $V_R$  with the CLEAN algorithm, which found a strong peak at  $P = 3.9060263 \text{ d}$ , nearly identical to the period found by Casares et al. (2005). Note that CLEAN does not determine error bars for this measurement and the value is not certain to the last three decimal places. This value was improved by the later orbital fit to  $P = 3.90608 \pm 0.00010 \text{ d}$ . Our group has previously found  $P = 4.1 \text{ d}$  (McSwain et al. 2001) and  $P = 4.4 \text{ d}$  (McSwain et al. 2004) for LS 5039, due to the very high scatter in its  $V_R$  curve, which has lead to considerable

confusion about the correct orbital period of this system. We note that our period search also resulted in  $P = 3.906$  d when we excluded the data of Casares et al. (2005), so we have added confidence that this is indeed the correct period for LS 5039. We also investigated other weak frequency signals found by CLEAN, but these periods did not produce a realistic  $V_R$  curve.

We determined the remaining orbital elements with the non-linear, least-squares fitting program of Morbey & Brosterhus (1974) to solve for the orbital elements. With each point assigned equal weight, the resulting orbital elements are displayed in Table 4.1.  $T_0$  indicates a time of periastron, a time at which the separation distance between the compact object and the O star is at its smallest. The eccentricity of the orbit,  $e$ , indicates the shape of the ellipse. A perfectly circular orbit would have  $e = 0$ . In the case of LS 5039, an eccentricity of 0.337 is unusually high for the short orbital period, indicating that the supernova which resulted in the compact object probably happened fairly recently and the orbit has not had time to circularize. The longitude of the ascending node of the orbit,  $\omega$ , represents the angle between the ellipse's semi-major axis and the line of sight to the observer.  $K_1$  is the velocity semi-amplitude of the primary star and is half the total amplitude of the  $V_R$  curve.  $\gamma$  represents the velocity of the binary system's center of mass. The mass function, represented by  $f(m)$ , is given by

$$f(m) = \frac{P}{2\pi G} K_1^3 = \frac{M_X^3}{(M_X + M_O)^2} \sin^3 i \quad (4.1)$$

where  $M_X$  is the mass of the compact object,  $M_O$  is the mass of the O star, and  $i$  is the inclination angle of the system. If we knew the inclination angle, we could use this to constrain the mass of the compact object. Similarly, if we assume masses for the compact object and the O star, we can calculate possible inclination angles for the system. The low value of the mass function combined with reasonable assumptions for the mass of the O

star suggest a compact companion of a few solar masses.  $a_1$  is the semi-major axis of the orbit. Since we do not know the inclination angle, we can only determine the semi-major axis as a function of the system inclination:  $a_1 \sin i$ . Finally,  $\sigma$  represents the rms error in our measurements.

Figure 4.2 illustrates the radial velocity curve of LS 5039 using all available  $V_R$  measurements. The  $V_R$  measurements and their deviation from the theoretical  $V_R$  curve are listed in Table 4.2. The spectroscopic orbital solution reveals spurious radial velocity points between orbital phases  $\phi = 0.3 - 0.6$ , shown in Figure 4.2. The orientation of the orbit at these phases is shown in Figure 4.3. We postulate that this blue shifted component may be a focused wind stream directed towards the compact companion, which is why we see the effect near stellar superior conjunction. In order to determine if our suspicions about the structure of the stellar wind are correct, we investigate the wind in the following section.

**Table 4.1:** Orbital Elements for LS 5039

Orbital Element	Value
$P$ (d)	$3.90608 \pm .00010$
$T_0$ (HJD-2,450,000)	$2825.985 \pm .053$
$e$	$.337 \pm .036$
$\omega$ (deg)	$236.0 \pm 5.8$
$K_1$ (km s <sup>-1</sup> )	$19.74 \pm .86$
$\gamma$ (km s <sup>-1</sup> )	$4.01 \pm .31$
$f(m)$ ( $M_\odot$ )	$.00261 \pm .00036$
$a_1 \sin i$ ( $R_\odot$ )	$1.435 \pm 0.066$
$\sigma$ (km s <sup>-1</sup> )	7.14

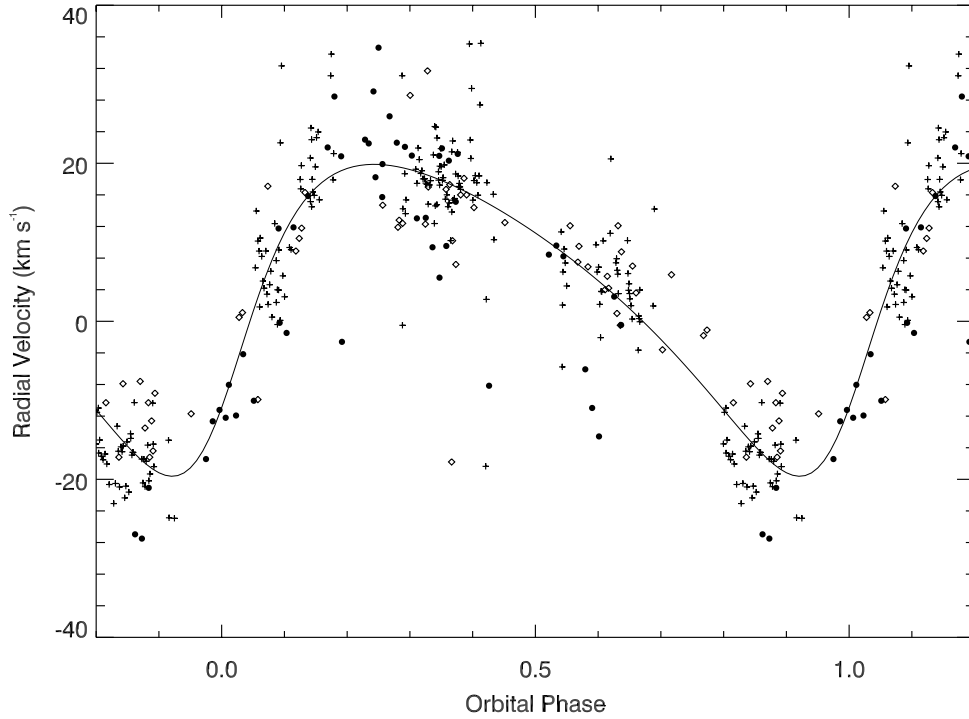


**Figure 4.2:** Radial velocity curve of LS 5039. Periastron corresponds to  $\phi = 0$  in this plot. Points plotted as open diamonds are from McSwain et al. (2001, 2004), crosses are from Casares et al. (2005), and filled circles are from this work.

**Table 4.2:** Radial Velocity Measurements

HJD (-2,450,000)	Orbital Phase	$V_R$ (km s <sup>-1</sup> )	(O-C) (km s <sup>-1</sup> )
4315.5746	0.351	21.9	4.1
4315.6176	0.362	20.3	2.9
4315.6607	0.373	15.1	-1.9
4316.6470	0.626	3.1	-0.3
4316.6900	0.637	-0.5	-3.1
4330.4876	0.169	22.0	3.9
4330.5296	0.180	28.4	9.8

Continued on next page...



Table 4.2 – Continued

HJD (−2,450,000)	Orbital Phase	$V_R$ (km s <sup>−1</sup> )	(O-C) (km s <sup>−1</sup> )
4330.5716	0.190	20.9	1.8
4333.6362	0.975	−17.4	−1.8
4333.6782	0.986	−12.7	1.2
4333.7202	0.997	−11.2	0.5
4334.6263	0.229	23.0	3.2
4334.6788	0.242	29.1	9.2
4334.7103	0.250	34.6	14.8
4338.5552	0.234	22.5	2.7
4338.5973	0.245	18.2	−1.6
4338.6393	0.256	15.7	−4.1
4341.5908	0.011	−8.0	0.2
4341.6354	0.023	−11.9	−6.4
4341.6797	0.034	−4.2	−1.5
4342.5470	0.256	19.9	0.1
4342.5912	0.268	25.9	6.2
4342.6361	0.279	22.6	3.0
4343.5828	0.521	8.4	−1.5
4343.6293	0.533	9.6	0.3
4343.6734	0.545	8.2	−0.4
4346.5929	0.292	22.1	2.7
4346.6358	0.303	21.0	1.8
4346.6673	0.311	13.0	−5.9
4354.5347	0.325	13.1	−5.5
4354.5767	0.336	9.4	−8.9
4354.6187	0.347	20.9	3.0
4355.5278	0.580	−6.1	−12.6
4355.5705	0.590	−11.0	−16.7

Continued on next page...

Table 4.2 – Continued

HJD (−2,450,000)	Orbital Phase	$V_R$ (km s <sup>−1</sup> )	(O-C) (km s <sup>−1</sup> )
4355.6133	0.601	−14.6	−19.6
4357.5744	0.103	−1.5	−13.2
4357.6174	0.114	11.9	−1.4
4357.5314	0.092	−0.2	−10.2
4358.6397	0.376	21.2	4.3
4358.5687	0.358	9.5	−8.0
4358.5263	0.347	5.5	−12.4
4360.5797	0.873	−27.5	−9.9
4360.5373	0.862	−27.0	−10.2
4360.6222	0.884	−21.1	−2.7
4525.8807	0.192	−2.6	−21.7
4536.8753	0.006	−12.2	−2.7
4544.8626	0.051	−10.1	−11.6
4552.8287	0.091	11.8	2.1
4560.8249	0.138	15.8	−0.0
4569.7635	0.426	−8.2	−23.0

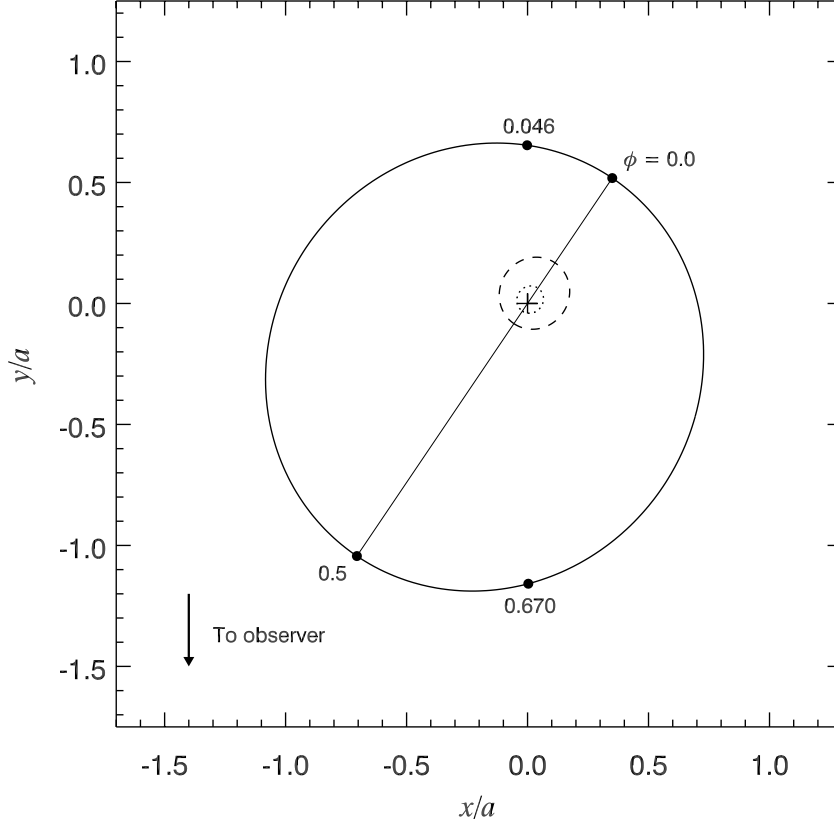


**Figure 4.3:** Orbital geometry of LS 5039, looking down on the orbital plane, showing the relative orbits ( $r/a$ ) of the optical star ( $23 M_{\odot}$ ; Casares et al. 2005) and the compact companion, which is either a  $3.7 M_{\odot}$  black hole (Casares et al. 2005) or a  $1.4 M_{\odot}$  neutron star. The relative orbit of the compact object is shown as a solid line, while the O star’s relative orbit depends on the mass of the companion. The dashed line indicates the O star’s orbit assuming a  $4 M_{\odot}$  black hole, while the dotted line assumes a  $1.4 M_{\odot}$  neutron star. The phases of periastron, apastron, and conjunctions are marked along the orbit of the compact companion. The center of mass is indicated with a cross, and the thin solid line is the orbital major axis.

### 4.3 Probing the Structure of the O Star Wind

We coadded the spectra from SOAR in sets of two to improve the S/N ratio of the data and used the orbital ephemeris of Aragona et al. (2009) to shift the  $H\alpha$  line in each observation

to the rest wavelength. The orientation and orbital phases of the O star at the times of our observations are shown in Figure 4.4. Casares et al. (2005) noted blue-shifted points in their radial velocity data at phase 0.45. As noted in the previous section, the radial velocity curve used to determine the orbital parameters in Aragona et al. (2009) showed additional blue-shifted points between phases 0.4 and 0.6. To investigate the source of these spurious points, we examined  $H\alpha$  for changing line profiles which would indicate the presence of large scale structures in the wind (such as a focused wind stream). A plot of the line profiles is shown in Figure 4.5. The line profile does not show variation above the level of the noise.

We also determined the mass loss rate of the system (Figure 4.6) from the equivalent width of the  $H\alpha$  line,  $W_{H\alpha}$ , using the method of Puls et al. (1996). The equivalent width is the area enclosed by the absorption line divided by the level of the continuum:

$$W = \int \frac{F_C - F_\lambda}{F_C} d\lambda \quad (4.2)$$

where  $F_C$  is the flux of the continuum and  $F_\lambda$  is the flux of the line at a given wavelength. The equivalent width of a line will vary with the column density of the absorbing material above the photosphere. In the case of a star with winds, the situation is slightly more complicated. The winds are flowing radially outward from the star. A section of the wind will be located directly in front of the stellar surface, and it will absorb some of the flux from the star. This absorption feature will be blue shifted since the wind is moving towards us. The section of the stellar wind that is located to either side of the star will contribute emission, since it is a thin gas. The emission and the absorption will be superimposed to create the line profile we actually observe. With a large amount of material in the wind, a P-Cygni line profile will be observed. In the case of LS 5039, the wind is too weak to produce a P-Cygni feature in the optical data, so the absorption line we observe only appears shallower. The resulting changes in the absorption line and the effect on the equivalent width can be

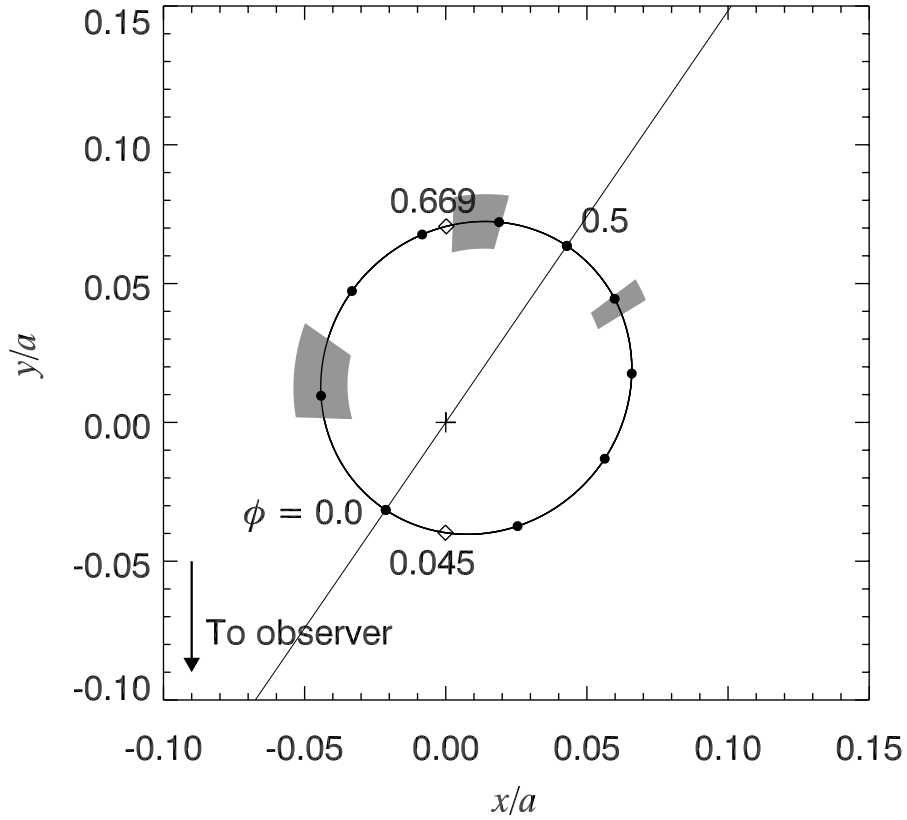


**Figure 4.4:** A close up view of the O star orbit (assuming a  $1.4 M_{\odot}$  companion) to highlight the orientation of the system during our SOAR observations. The gray shaded regions indicate the phases of our observations. The diamonds mark the phases of inferior and superior conjunction.

measured.

Puls et al. (1996) carefully modeled the equivalent width generated by the stellar wind around massive stars to determine a relationship between the equivalent width of the line and the mass loss from the stellar wind. They found an empirical relationship between the equivalent width and a factor  $Q$  related to the mass loss rate as

$$Q = \frac{\dot{M}/(10^{-6} M_{\odot}/yr)}{(R_{\star}/R_{\odot})^{3/2}} \quad (4.3)$$

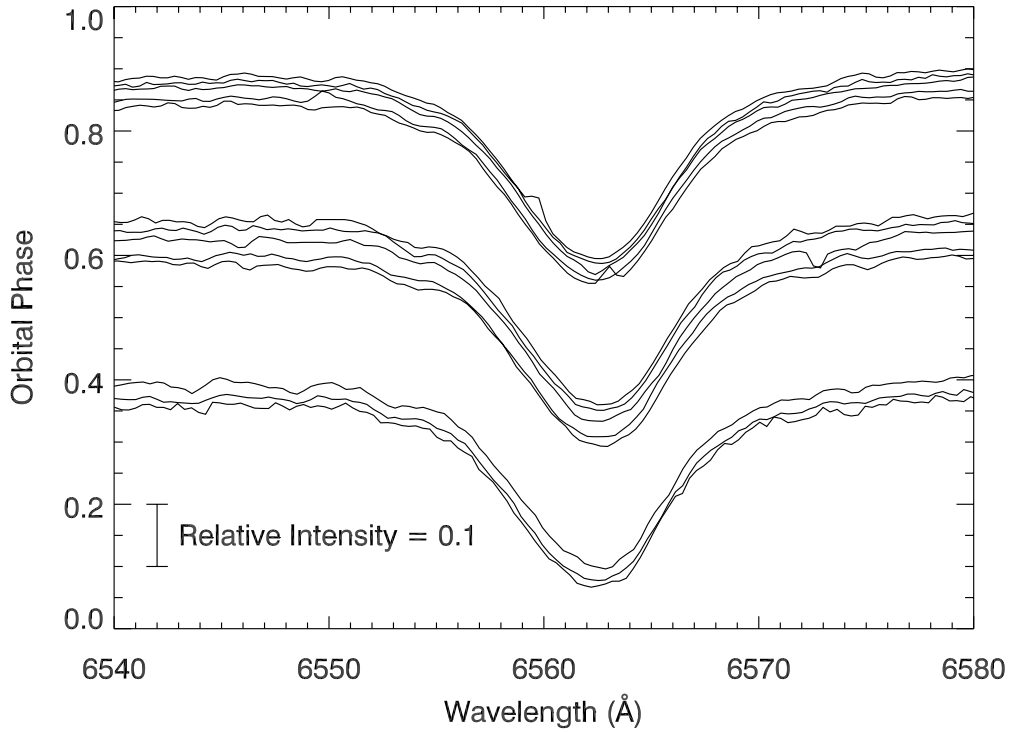


**Figure 4.5:** The  $H\alpha$  line from the SOAR observations. Consecutive pairs of spectra were coadded to reduce the S/N ratio. We shifted each spectrum to the rest wavelength to highlight any variations in the line profile due to structure in the stellar wind.

where  $\dot{M}$  is the mass loss rate in solar masses per year and  $R_*$  is the radius of the star. The mass loss rates we obtained for LS 5039 are plotted as a function of orbital phase in Figure 4.6. Our measurements show considerable scatter but no significant variation correlated with orbital phase. We find an average mass loss rate of  $1.9 \times 10^{-8} M_{\odot} \text{ yr}^{-1}$ .

Spectra from the Goodman spectrograph suffer from fringing near the  $H\alpha$  line. The CCD chip in the instrument is backlit, allowing internal reflection in the light absorbing layer to create an interference pattern at longer wavelengths. As a result, we cannot attribute any fine scale variations in the line profile to real features in the the wind, as they may be the result of fringing. Thus far, there is not a method to correct for this effect.

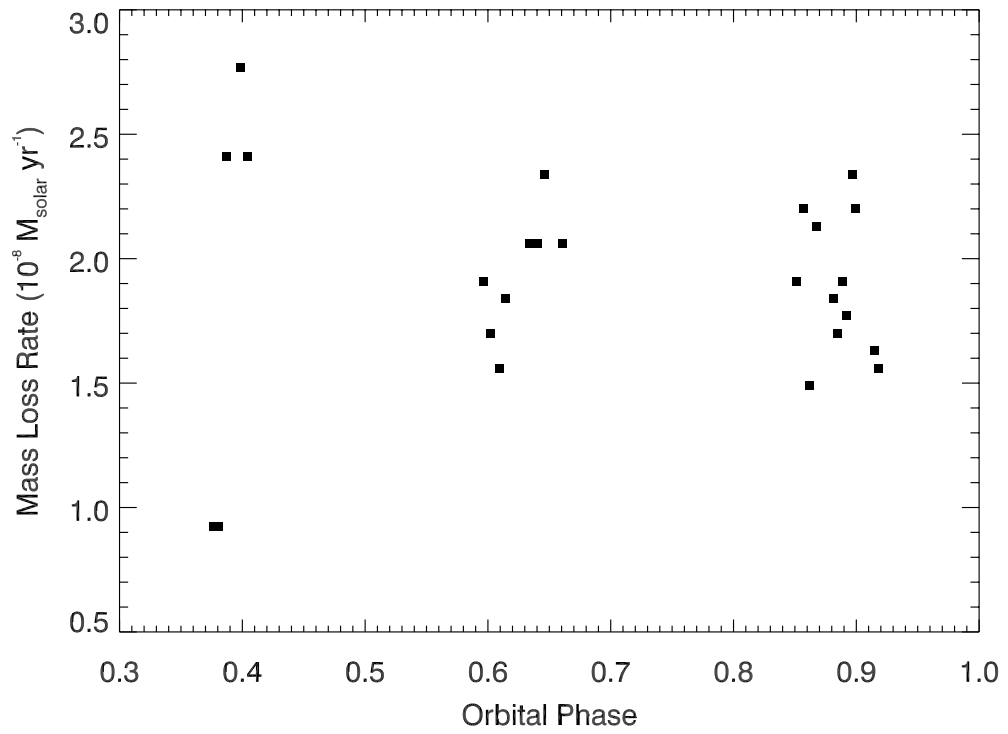


**Figure 4.6:** The mass loss rate of LS 5039 plotted as a function of orbital phase. The variations originate from error in measuring  $W_{H\alpha}$  rather than any real variation in the mass loss rate of the system over the orbital period.

# Chapter 5

## LS 5039 at Radio Wavelengths

### 5.1 Radio Emission from the Stellar Wind of LS 5039

The winds from massive stars have been observed to emit as a blackbody at radio wavelengths (Lamers & Leitherer 1993). Free-free interactions are the main sources of opacity in the winds and constitute a stronger effect at lower wavelengths. The radius at which the stellar winds become transparent to radio waves will be larger than the radius at which they become transparent to optical wavelengths, making the star appear larger in radio frequencies. We can use the mass loss rate obtained in Chapter 4 to determine the contribution of the stellar wind of LS 5039 to the total observed radio flux. At radii where the optical depth of the wind is greater than 1, the stellar wind is opaque to light. Outside of this radius, photons will still be scattered by the material, but not to the extent that no photons will reach the observer. We can estimate the amount of flux emitted by the O star wind at radio wavelengths by calculating the radius where the transmission of photons through the material dominates over scattering effects. Above that radius, the wind of the star is considered to be transparent to radio emission; radio emission from less than that radius is severely attenuated and will not significantly contribute to the observed flux. In order to



estimate the radio emission, we can assume the stellar wind is radiating as a blackbody at this radius and compute the expected flux as a function of wavelength.

Our preliminary optical results justify assuming a spherically symmetric stellar wind when modeling the radio emission. The stellar wind absorbs continuum emission in the radio primarily through free-free interactions between ions. Lamers & Cassinelli (1999) give the free-free opacity in  $\text{cm}^2 \text{g}^{-1}$  as

$$\kappa_\nu^{\text{ff}} = 1.78 \times 10^{-2} Z^2 \nu^{-2} g_\nu T^{-3/2} \frac{n_i n_e}{\rho} \quad (5.1)$$

where  $Z^2$  is the squared root mean square charge of the atoms,  $\nu$  is the frequency in Hz,  $T$  is the temperature of the wind,  $n_e$  and  $n_i$  are the electron and ion number densities, and  $\rho$  is the wind mass density.  $g_\nu$  is the gaunt factor determined by

$$g_\nu = 10.6 + 1.90T - 1.26 \log \nu Z \quad (5.2)$$

We assume the wind is fully ionized, so we can write the ion and electron densities as a function of the wind density:

$$n_e = \gamma_e n_i \quad (5.3)$$

$$n_i = \frac{\rho}{\mu} \quad (5.4)$$

where  $\gamma_e$  is the ratio of free electrons to ions and  $\mu$  is the mean atomic mass of the ions and electrons in the wind. In the case of LS 5039, we assume that the stellar wind is composed purely of ionized hydrogen atoms, so we can set  $\gamma_e$  and  $Z$  equal to 1. The absorption coefficient,  $k_\nu$ , is given by  $k_\nu = \kappa_\nu^{\text{ff}} \rho$ . The wind density at a radius  $r$  from the star is given by

$$\rho = \frac{\dot{M}}{4\pi r^2 v(r)} \quad (5.5)$$

where  $\dot{M}$  is the mass loss rate and  $v(r)$  is the wind speed as a function of radius. We can approximate  $v(r)$  using a  $\beta$ -velocity law

$$v(r) = v_{\infty} \left(1 - \frac{R_{\star}}{r}\right)^{\beta} \quad (5.6)$$

where  $R_{\star}$  is the stellar radius and  $v_{\infty}$  is the terminal wind velocity, and  $\beta = 1$  (Puls et al. 1996). The absorption coefficient can be found by combining Equations 5.1-5.6 and setting  $\beta$  equal to 1 to obtain

$$k_{\nu} = 1.13 \times 10^{-4} \frac{g_{\nu}}{\mu^2} \nu^{-2} T^{-3/2} \left( \frac{\dot{M}}{r^2 v_{\infty} (1 - \frac{R_{\star}}{r})} \right)^2 \quad (5.7)$$

Therefore, the free-free optical depth is

$$\tau_{\nu} = 1.13 \times 10^{-4} \frac{g_{\nu}}{\mu^2} \nu^{-2} T^{-3/2} \left( \frac{\dot{M}}{v_{\infty}} \right)^2 \int_r^{\infty} r^{-2} (r - R_{\star})^{-2} dr \quad (5.8)$$

All values are in cgs units.

We calculated the distance from the star at which  $\tau_{\nu}=1/3$  (following the derivation of Lamers & Cassinelli 1999) and assumed that the wind would emit as a blackbody with an effective temperature of 30,000K (about 2/3 the temperature of the O star) at this radius. We used the Rayleigh-Jeans approximation to estimate the predicted radio flux at 3 cm, 6 cm, 13 cm, and 20 cm. The results are shown in Table 5.1. The calculated radio flux expected from a thermally emitting stellar wind is on the order of  $\mu\text{Jy}^1$  for each wavelength band. By contrast, the mean observed fluxes, listed in Table 5.2, are on the order of 10–40 mJy. The observed 20 cm radio fluxes show severe errors, so we do not include these measurements in our analysis. Clearly the bulk of the radio flux in this system is not due to a thermally emitting stellar wind. These results and the  $\text{H}\alpha$  measurements from Chapter

---

<sup>1</sup>Jansky (Jy) is a standard unit for measuring energy density in radio astronomy. 1 Jy =  $10^{-23}$  ergs  $\text{cm}^{-2}$   $\text{s}^{-1}$   $\text{Hz}^{-1}$

**Table 5.1:** Radio flux expected from a thermally emitting stellar wind compared to our mean observed fluxes.

$\lambda$ (cm)	20	13	6	3
$R(\tau_\nu = 1/3) (R_\odot)$	223.3	167.4	102.3	65.1
$F_{predicted}$ (mJy)	0.00008	0.0002	0.0009	0.0034
$\langle F_{observed} \rangle$ (mJy)	–	29.0	25.0	21.3

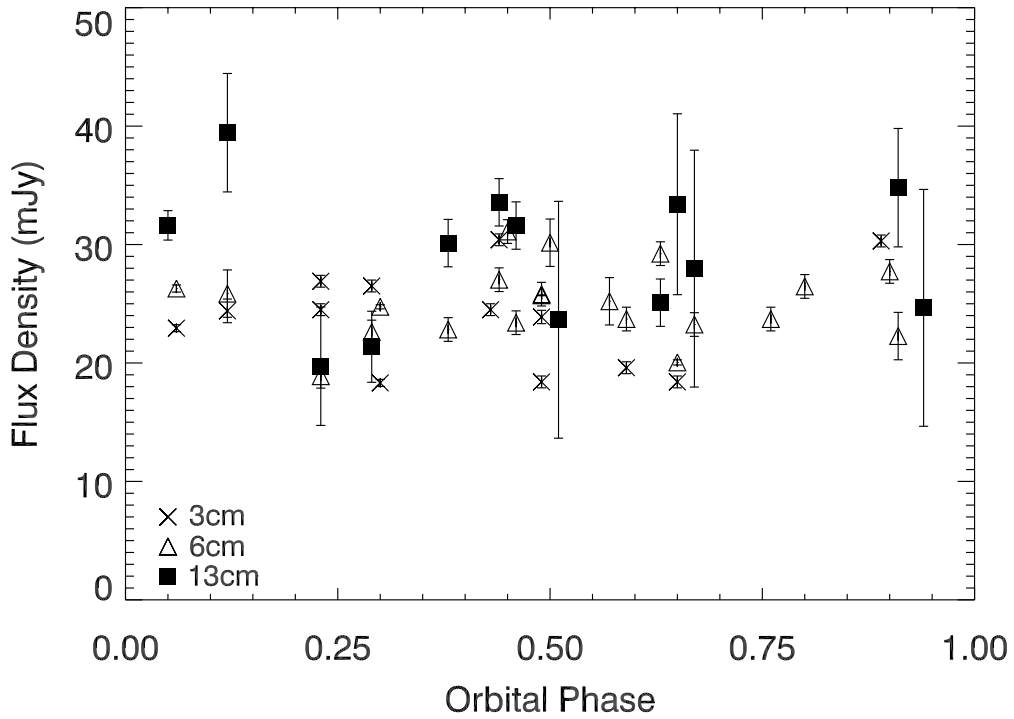


**Figure 5.1:** Radio flux measurements of LS 5039.

4 have been published in the *Bulletin of the Liège Royal Scientific Society* (Aragona et al. 2011).

The error bars on the radio flux data are fairly large, but there appears to be real variation in radio emission, particularly between phase 0.0 and phase 0.25 (Figure 5.1). The observed radio flux variations cannot be explained by pure blackbody radiation produced

**Table 5.2:** Radio Fluxes for LS 5039

HJD (+2450000)	Orbital Phase	Observed Radio Flux (mJy)		
		at 3 cm	at 6 cm	at 13 cm
4511.47	0.50	–	$30.2 \pm 2.0$	$23.6 \pm 10$
4587.34	0.93	–	$25.2 \pm 2.0$	$24.7 \pm 10$
4629.29	0.67	–	$23.3 \pm 1.0$	$27.9 \pm 10$
4740.88	0.23	$26.9 \pm 0.5$	–	–
4754.64	0.76	–	$23.7 \pm 1.0$	–
4759.96	0.12	$24.4 \pm 1.0$	$25.9 \pm 2.0$	$39.4 \pm 5$
4770.79	0.89	$30.3 \pm 0.5$	$27.7 \pm 1.0$	–
4776.83	0.43	$24.5 \pm 0.5$	$27.0 \pm 1.0$	$33.6 \pm 2.0$
4780.75	0.44	$30.4 \pm 0.5$	$31.1 \pm 1.0$	–
4793.87	0.80	–	$26.5 \pm 1.0$	–
4804.75	0.59	$19.6 \pm 0.5$	$23.7 \pm 1.0$	–
4811.75	0.38	–	–	$30.1 \pm 2.0$
4820.54	0.63	–	–	$25.1 \pm 2.0$
4827.70	0.46	–	–	$31.6 \pm 2.0$
4838.50	0.23	$24.5 \pm 0.5$	$18.9 \pm 1.0$	$19.7 \pm 5.0$
4850.46	0.29	$26.5 \pm 0.5$	$22.6 \pm 1.0$	$21.4 \pm 3.0$
4860.68	0.91	–	$22.3 \pm 2.0$	$34.8 \pm 5.0$
4878.60	0.49	$18.4 \pm 0.5$	$25.8 \pm 1.0$	–
4972.35	0.49	$23.9 \pm 0.6$	$25.71 \pm 0.037$	–
4983.31	0.30	$18.3 \pm 0.3$	$24.74 \pm 0.17$	–
4994.09	0.06	$22.9 \pm 0.3$	$26.29 \pm 0.30$	$31.6 \pm 1.2$
5004.21	0.65	$18.4 \pm 0.5$	$20.05 \pm 0.22$	$33.4 \pm 7.6$

in the stellar wind of the primary. This should be constant with respect to orbital phase since we assumed a spherically symmetric wind. The emission is probably generated by the interaction between the stellar wind and the compact object. The correlation of the radio emission with orbital phase suggests a wind-wind interaction region. The variations in radio emission produced by a precessing jet should not depend on orbital phase since the optical depth along the line of sight is probably constant at the large distances from the compact object where the radio emitting regions of a jet would be located. In the colliding

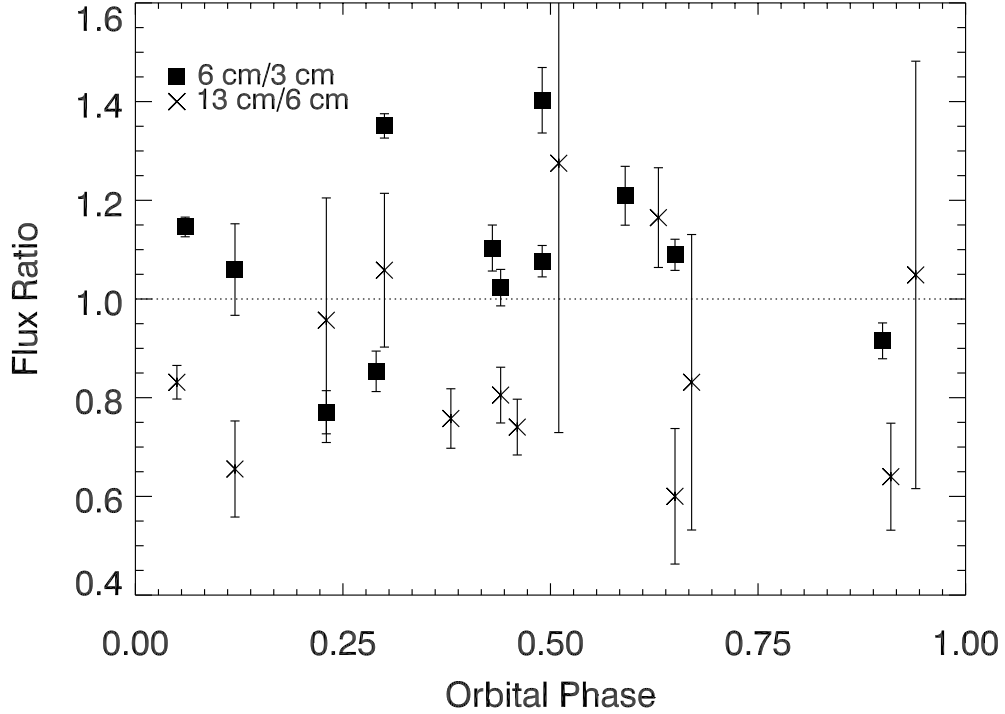


**Figure 5.2:** Ratio of fluxes for 3 cm/6 cm and 6 cm/13 cm plotted with respect to orbital phase.

wind scenario, a non-thermal distribution of particles from the pulsar wind is ejected into the shock region. This material will flow away from the shock region in a comet like tail, with emission dominated by synchrotron losses. The radio emission expected from such a scenario would be modulated with orbital phase (Dubus 2006). Furthermore, a radio map of such a configuration would bear some resemblance to a microquasar jet (Dubus 2006), which is consistent with the observations of Paredes et al. (2002).

The intensity of the radio emission with respect to wavelength can be described using a power law, where  $F_\nu \propto \nu^{-\Gamma}$ . Purely thermal radio emission from the stellar wind should have a spectral index,  $\Gamma = -0.6$  (Lamers & Cassinelli 1999). In order to calculate  $\Gamma$  for any set of two observations, we can start from

$$F_\nu = A\nu^{-\Gamma} \quad (5.9)$$

where  $A$  is a constant. For any pair of frequencies,  $\nu_1$  and  $\nu_2$ ,

$$\left(\frac{F_{\nu_1}}{F_{\nu_2}}\right) = \left(\frac{\nu_1}{\nu_2}\right)^{-\Gamma} \quad (5.10)$$

Taking the log of both sides and solving for  $\Gamma$  yields

$$\Gamma = \frac{\log(F_{\nu_1}/F_{\nu_2})}{\log(\nu_2/\nu_1)} \quad (5.11)$$

We performed a preliminary calculation of the spectral indices using pairs of 3 cm/6 cm and 6 cm/13 cm fluxes from each observation. For the 6 cm/13 cm points, values for  $\Gamma$  lie between 0.5 and -1.0, have error bars larger than the scatter in the points, and show no obvious trends with respect to orbital phase. For the 3 cm/6 cm fluxes, the values are between -0.2 and 0.6. The error bars on  $F_{\nu_1}/F_{\nu_2}$  will be smaller than the error bars on  $\Gamma$ , so we plotted the ratio of the 3 cm/6 cm and 6 cm/13 cm fluxes to search for variation correlated with orbital period (Figure 5.2).

## 5.2 The Colliding Wind Scenario in LS 5039

Our goal is to use the radio observations to constrain the nature of the compact object in LS 5039. To this end, I have begun examining the effect of the colliding wind scenario on radio emission from the system. Figure 5.3 shows the basic geometry of a wind-wind collision region. Let the filled circle at (0,0) represent the pulsar and the filled circle at (0,50) represent the O star. The separation distance between the two objects is labeled  $D$ . The geometry of the shock front can be roughly described by two numbers: the stagnation point ( $R_{stag}$ ) and the opening angle ( $\theta_\infty$ ). Both the wind from the O star and the wind from the pulsar each exert a certain pressure dependent on their densities and speeds. The forward-most point of the shock front, called the stagnation point, will occur where these

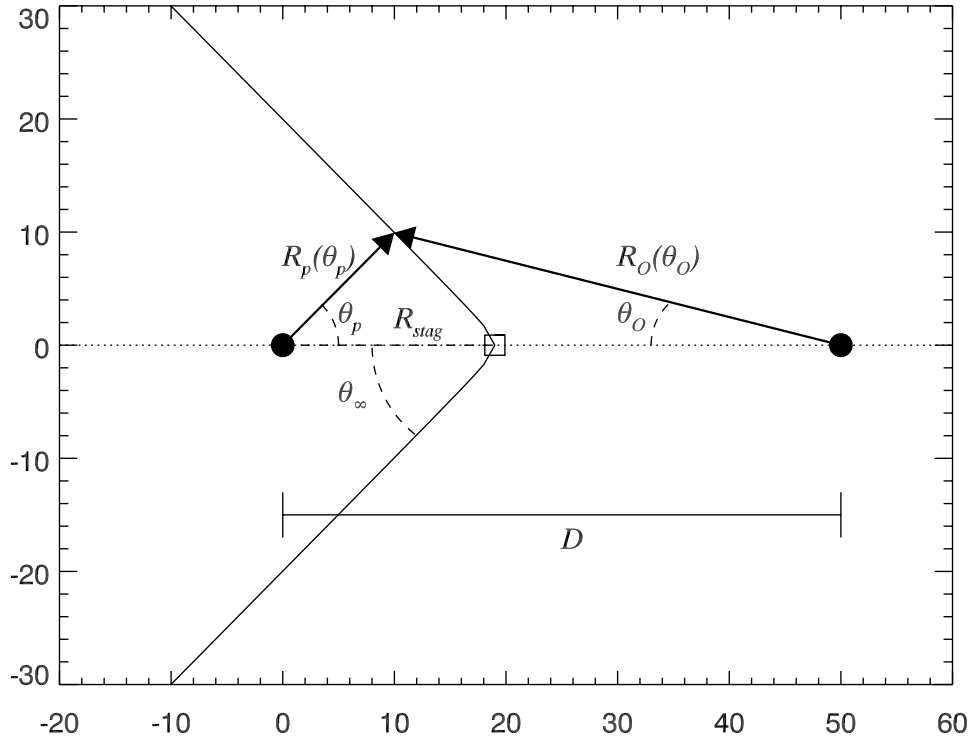


**Figure 5.3:** The basic geometry of a wind-wind collision. The O star and the pulsar are represented by filled circles, where  $D$  is the distance between them. The stagnation point is marked by an open square. The shockfront is the solid hyperbola opening to the left.  $R_p(\theta)$  represents the distance from the pulsar to the shockfront, While  $R_{stag}$  represents the location of the stagnation point with respect to the pulsar.  $\theta_\infty$  is the opening angle of the shock. Units are arbitrary.

two pressures balance. The stagnation point is marked by an open square and its distance from the pulsar is labeled as  $R_{stag}$ . The location of any point along the shock front with respect to the pulsar can be represented by some function,  $R_p(\theta_p)$ . The shock front asymptotically approaches a line at some angle  $\theta_\infty$  to the line between the compact object and the stagnation point.

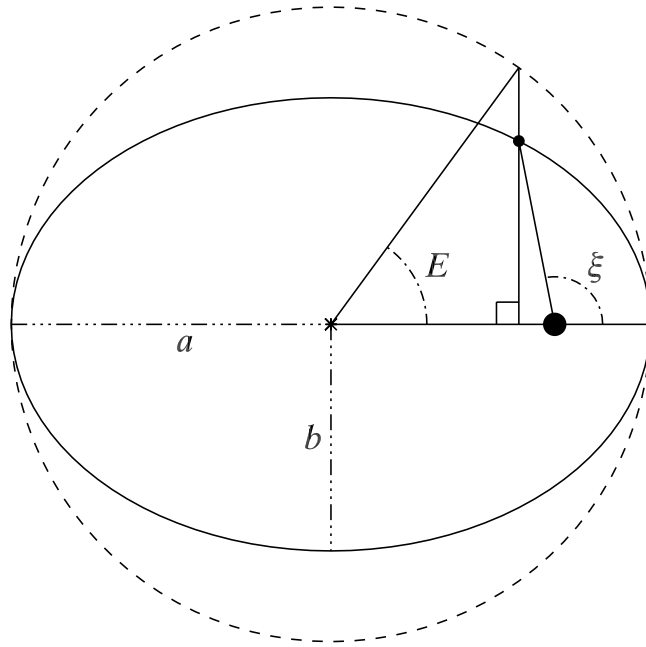


**Figure 5.4:** Diagram of an elliptical orbit. The large dot represents the focus of the ellipse from which the true anomaly,  $\xi$ , is measured. The small dot represents the orbiting object. The eccentric anomaly,  $E$ , is determined by the projection of the location of the object onto a circle with a radius equal to ellipse's semi-major axis,  $a$ . The line marked  $b$  represents the semi-minor axis of the ellipse.

### 5.2.1 Orbital Geometry

The location of the shock front will depend on the relative strengths of the O star and pulsar winds. This will vary with  $D$ , which changes throughout the orbit and can easily be calculated based on the orbital parameters presented in Chapter 4. We can use Kepler's 3rd



Law:

$$P^2 = \frac{4\pi^2}{G(M_O + M_p)} a^3 \quad (5.12)$$

where  $P$  is the orbital period of the system,  $M_O$  is the mass of the O star,  $M_X$  is the mass of the compact object, and  $a$  is the semi-major axis of the orbit. The equation to describe the distance between a point on an ellipse and one of the focii,  $D$ , is

$$D = \frac{a(1 - e^2)}{1 + e \cos \xi} \quad (5.13)$$

where  $e$  is the eccentricity of the ellipse and  $\xi$  is the angle between the semi-major axis and  $D$  (otherwise known as the true anomaly). Combining Equations 5.12 and 5.13 yields

$$D(\xi) = \left( \frac{G(M_O + M_p)P^2}{4\pi^2} \right)^{1/3} \frac{1 - e^2}{1 + e \cos \xi} \quad (5.14)$$

Finally, we need to express this equation in terms of the eccentric anomaly so that we can relate the orbital separation to the orbital phase as seen from earth. The eccentric anomaly,  $E$ , is the projection of the location of the object onto a circle with a radius equal to the ellipse's semi-major axis (see Figure 5.4). The true anomaly,  $\xi$ , and  $E$  are related by

$$\cos \xi = \frac{\cos E - e}{1 - e \cos E} \quad (5.15)$$

Therefore,

$$D(E) = \left( \frac{G(M_O + M_p)P^2}{4\pi^2} \right)^{1/3} (1 - e \cos E) \quad (5.16)$$

Finally, we can relate the eccentric anomaly to time,  $t$  and the orbital phase,  $\phi$ .

$$t = \frac{P}{2\pi} (E - e \sin E) \quad (5.17)$$

and

$$\phi = \frac{t}{P} = \frac{E - e \sin E}{2\pi} \quad (5.18)$$

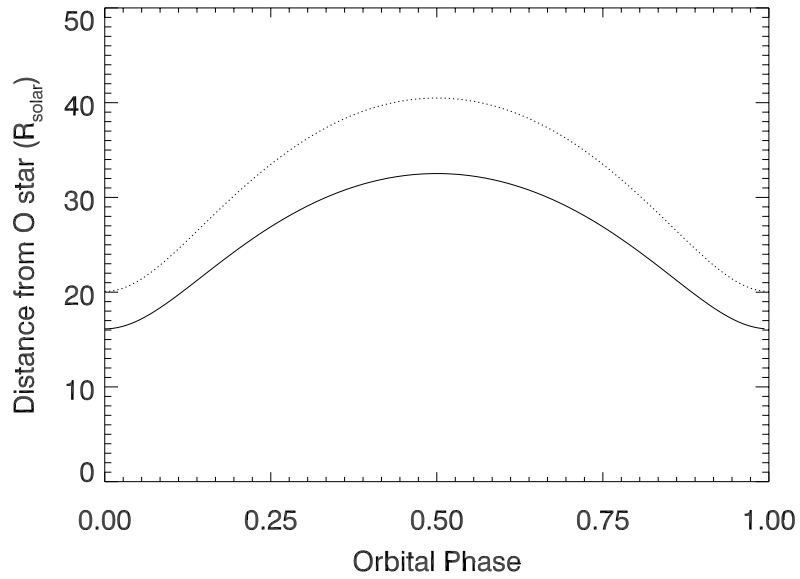


**Figure 5.5:** The distance of the compact object from the O star,  $D$ , is indicated by the dotted line, while the location of the stagnation point,  $R_O$ , is represented by the solid line.

I created a program, `orbsep.pro`, which applies these Equations 5.16 and 5.18 to a grid of true anomalies between 0 and  $2\pi$  and calculates the corresponding orbital phases and separation distances at each value. I assumed an  $M_O = 23 M_\odot$  (Casares et al. 2005),  $M_X = 1.4 M_\odot$ ,  $P = 3.90806$  days, and  $e = 0.337$ . The orbital separation as a function of orbital phase is plotted in Figure 5.5.

## 5.2.2 The Stagnation Point of the Shock Front

In order to determine the nature of the wind-wind collision region, we can start by calculating the location of the stagnation point. The surface of the shock cone will form where the ram pressures of the stellar wind and the pulsar wind are balanced. I am neglecting the effects of orbital velocity in this calculation, so the stagnation point is where the ram pressures balance along the line between the compact object and the O star. Ram pressure

is defined as  $P = \rho v^2$ , where  $\rho$  is the wind density and  $v$  is the wind velocity. Using the density of the stellar wind from Equation 5.5

$$P_O = \frac{\dot{M}_O v_O(r_O)}{4\pi r_O^2} \quad (5.19)$$

where  $\dot{M}_O$  is the mass loss rate,  $v_O$  is the wind velocity, and  $r_O$  is the distance from the O star.

In the case of the relativistic pulsar wind, the pulsar spin down energy,  $\dot{E}_{sp}$ , provides information about the wind's momentum. First, we write the ram pressure in terms of the wind momentum. The pulsar wind density can be rewritten as

$$\rho_p = \frac{p_p}{(4\pi r_p^2 v_p) v_p} \quad (5.20)$$

where  $p_p$  is the momentum of the pulsar wind,  $r_p$  is the distance from the pulsar, and  $v_p$  is the velocity of the pulsar wind. Writing  $p_p$  in terms of  $\dot{E}_{sp}$  gives

$$\dot{p}_p = \frac{\dot{E}_{sp}}{c} \quad (5.21)$$

$$P_p = \frac{\dot{E}_{sp}}{4\pi r_p^2 c} \quad (5.22)$$

where  $c$  is the speed of light. Note that  $\dot{E}_{sp}$  is unknown for LS 5039. A method for obtaining a reasonable estimate to use in these calculations is described in Section 5.2.3.

Substituting  $R_p = D - R_O$  where  $D$  is the separation distance of the binary, assuming  $v_O(R_O) = v_{O,\infty}$ , and setting Equation 5.19 equal to Equation 5.22 yields

$$\left( \frac{D}{R_O} - 1 \right) = \sqrt{\frac{\dot{E}_{sp}}{c \dot{M} v_{O,\infty}}} \quad (5.23)$$

Solving this equation for  $R_O$  yields the location of the stagnation point of the shock front with respect to the O star.

$$R_O = \frac{D}{\eta^{1/2} + 1} \quad (5.24)$$

where  $\eta = \frac{\dot{E}_{sp}}{c\dot{M}v_{O,\infty}}$ .

I assumed a mass loss rate for the stellar wind of  $1.9 \times 10^{-8} M_{\odot} \text{ yr}^{-1}$  (see Section 4.3), a terminal wind velocity for the O star of  $2440 \text{ km s}^{-1}$  (McSwain et al. 2004), and an  $\dot{E}_{sp}$  of  $5.3 \times 10^{35} \text{ ergs s}^{-1}$  (see Section 5.2.3), which gives  $\eta = 0.06$ . The location of the stagnation point with respect to orbital phase is plotted in Figure 5.5.

### 5.2.3 Estimating Spin Down Energy

Assuming the compact object in LS 5039 is a neutron star, no direct measurement of its properties exists. Therefore, we made some reasonable assumptions about the pulsar wind for our model of the shock front location and opening angle. PSR B1259-63 is a well studied  $\gamma$ -ray binary that consists of a neutron star, for which  $\dot{E}_{sp}$  is known, and a Be star (Takata & Taam 2009; Chernyakova et al. 2009; Moldón et al. 2011). The separation distance of PSR B1259-63 at periastron is similar to that of LS 5039 at apastron. At the time of periastron in PSR B1259-63, the X-ray emission from the system is created from the interaction of the pulsar with the polar region of the Be star wind. The massive star in PSR B1259-63 is classified as an O9.5Ve star (Moldón et al. 2011). For the polar winds of these stars, a typical mass loss rate is on the order of  $10^{-8} M_{\odot} \text{ yr}^{-1}$  and typical terminal wind velocities of about  $2000 \text{ km s}^{-1}$  (Takata & Taam 2009). In the discussion at the end of Chapter 4, we found an average mass loss rate for LS 5039 of  $1.9 \times 10^{-8} M_{\odot} \text{ yr}^{-1}$ . The terminal wind velocity of the O star is  $2440 \text{ km s}^{-1}$  (McSwain et al. 2004). Furthermore the two objects are located at similar distances from earth: 2.3 kpc for PSR B1259-63 and 2.5 kpc for LS 5039 (Negueruela et al. 2011; Casares et al. 2005). Since the physical properties of LS 5039 at apastron and PSR B1259-63 at periastron are so similar, we can obtain an order of magnitude estimate of  $\dot{E}_{sp}$  for LS 5039 by comparing the X-ray fluxes of these

two systems. The ratio of X-ray fluxes should be directly proportional to the ratio of  $\dot{E}_{sp}$ . Bosch-Ramon et al. (2007) give an X-ray flux near apastron for LS 5039 of  $1.18 \times 10^{-11}$  erg cm<sup>-2</sup> s<sup>-1</sup> with a spectral index of 1.51 in the 0.3-10 keV range. The X-ray flux near periastron for PSR B1259-63 is about  $1.4 \times 10^{-11}$  erg cm<sup>-2</sup> s<sup>-1</sup> in the 1 – 10 keV range (Chernyakova et al. 2009) and  $\dot{E}_{sp} = 8 \times 10^{35}$  erg s<sup>-1</sup> (Takata & Taam 2009). Correcting the flux of LS 5039 for the 1– 10 keV range of the PSR B1259-63 observations and taking the ratio of the fluxes yields a spin down energy of  $\dot{E}_{sp} = 5.3 \times 10^{35}$  erg s<sup>-1</sup> for LS 5039. Again, this process only provides a rough estimate of the spindown energy, but is sufficient for our initial examination of the shock region.

#### 5.2.4 Opening Angle of the Shock Front

The shock front of the wind collision zone will resemble a hyperboloid asymptotically approaching a line at some angle,  $\theta_\infty$ , to the line between the compact object and the O star. In order to approximate this, we first need to consider a more general formulation that accounts for the entire shock front. The following discussion is adapted from Cantó et al. (1996). Consider a coordinate system with the  $\hat{z}$ -direction pointing from the pulsar to the O star and the  $\hat{r}$ -direction perpendicular to that. At the shock front, angular momentum,  $L$ , and linear momentum,  $p$ , must be conserved. If the wind speed within the shock can be written as  $\vec{v} = v_r \hat{r} + v_z \hat{z}$  in cylindrical coordinates, then we can write the total change in momentum with respect to time ( $\dot{p}_r(\theta_p) \hat{r} + \dot{p}_z(\theta_p) \hat{z}$ ) of the shocked material as

$$\dot{p}_r(\theta_p) \hat{r} + \dot{p}_z(\theta_p) \hat{z} = \dot{M}(\theta_p)(v_r \hat{r} + v_z \hat{z}) \quad (5.25)$$

and the change in angular momentum with respect to time ( $\dot{L}(\theta_p)$ )

$$\dot{L}(\theta_p) = \dot{M}(\theta_p)v_{\theta_p}(\theta_p)R_p(\theta_p) \quad (5.26)$$

along a contour at an angle  $\theta_p$  from the line between the objects where  $R_p(\theta_p)$  is the distance from the compact object to the shock at  $\theta_p$  in terms of the total mass loss rate  $\dot{M}(\theta_p)$ . For material flowing along the shock,

$$v_{\theta_p} = v_r \cos \theta_p - v_z \sin \theta_p \quad (5.27)$$

Therefore, by conservation of momentum,

$$\dot{p}_r(\theta_p)\hat{r} + \dot{p}_z(\theta_p)\hat{z} = [\dot{p}_{r,p}(\theta_p) + \dot{p}_{r,O}(\theta_p)]\hat{r} + [\dot{p}_{z,p}(\theta_p) + \dot{p}_{z,O}(\theta_p)]\hat{z} = \dot{M}(\theta_p)(v_r\hat{r} + v_z\hat{z}) \quad (5.28)$$

$$\dot{L}(\theta_p) = \dot{L}_p + \dot{L}_O \quad (5.29)$$

where  $\dot{p}_{r,p}(\theta_p)\hat{r} + \dot{p}_{z,p}(\theta_p)\hat{z}$  is the change in linear momentum with respect to time of the pulsar wind,  $\dot{p}_{r,O}(\theta_p)\hat{r} + \dot{p}_{z,O}(\theta_p)\hat{z}$  is the change in linear momentum with respect to time of the O star wind,  $\dot{L}_p$  is the change in angular momentum with respect to time of the pulsar wind and  $\dot{L}_O$  is the change in angular momentum with respect to time of the O star wind. By taking the derivative of the basic equations for conservation of momentum, everything can be expressed in terms of mass loss rates and spin down energies (measurable quantities). Solving Equations 5.25 and 5.29 for  $R_p(\theta_p)$  yields

$$R_p(\theta_p) = \frac{\dot{L}_p + \dot{L}_O}{[\dot{p}_{r,p} + \dot{p}_{r,O}] \cos \theta_p - [\dot{p}_{z,p} + \dot{p}_{z,O}] \sin \theta_p} \quad (5.30)$$

Consider a wind from the pulsar. The mass loss rate through a surface described by  $\theta$  is

$$\dot{M}_{\theta_p} = \frac{\dot{M}_p}{2}(1 - \cos \theta_p) \quad (5.31)$$

where  $\dot{M}_p$  is the mass loss rate of the pulsar. For the pulsar, the change in linear momentum through this area can be written as

$$\dot{p}_{r,p}(\theta_p) = \int_0^\infty v \sin \theta_p d\dot{M} = \frac{\dot{M}_p v}{4}(\theta_p - \sin \theta_p \cos \theta_p) = \dot{p}(\theta - \sin \theta \cos \theta_p) \quad (5.32)$$

$$\dot{p}_{z,p}(\theta_p) = \int_0^\infty v \cos \theta d\dot{M} = \frac{\dot{M}_0 v}{4} \sin^2 \theta_p = \dot{p} \sin^2 \theta_p \quad (5.33)$$

In order to simplify the calculations, we assume that the angular momentum,  $L_p$ , is equal to zero. This implies that the pulsar wind is traveling radially outward from the pulsar. Since a pulsar would have highly beamed emission and strong magnetic fields, this assumption is probably inaccurate. As I develop this work, I plan to incorporate a more accurate representation of the pulsar wind. For the pulsar wind, we know the momentum of the wind in terms of the spin-down energy, so  $\dot{p} = \dot{E}_{sp}/c$ .

Next, consider the wind from the O star. If  $R_O(\theta_O)$  is the distance between the O star and the shockfront at some angle  $\theta_O$  from the line between the O star and the pulsar (see Figure 5.3),

$$\dot{M}_{\theta_O} = \frac{\dot{M}_O}{2}(1 - \cos \theta_O) \quad (5.34)$$

$$\dot{p}_{r,O}(\theta_O) = \frac{\dot{M}_O v_O}{4}(\theta_O - \sin \theta_O \cos \theta_O) \quad (5.35)$$

$$\dot{p}_{z,O}(\theta_O) = -\frac{\dot{M}_O v_O}{4} \sin^2 \theta_O \quad (5.36)$$

and

$$\dot{L}_O = \int_0^{R_p} r v_O dM_O = \frac{\dot{M}_O v_O}{4}(\theta_O - \sin \theta_O \cos \theta_O)D \quad (5.37)$$

Plugging these values into Equation 5.30 and again taking  $\eta = \frac{\dot{E}_{sp}}{c\dot{M}_O v_O}$  yields

$$R_p(\theta_p) = \frac{(\theta_O - \sin \theta_O \cos \theta_O)D}{[\eta(\theta_p - \sin \theta_p \cos \theta_p) + (\theta_O - \sin \theta_O \cos \theta_O)] \cos \theta_p - [\eta \sin^2 \theta_p + \sin^2 \theta_O] \sin \theta_p} \quad (5.38)$$

From geometry, we find that  $R_p(\theta_p) = D \sin \theta_O \csc(\theta_p + \theta_O)$ . Solving Equation 5.38 for a relationship between  $\theta_p$  and  $\theta_O$  gives

$$\theta_O \cot \theta_O = 1 + \eta(\theta_p \cot \theta_p - 1) \quad (5.39)$$

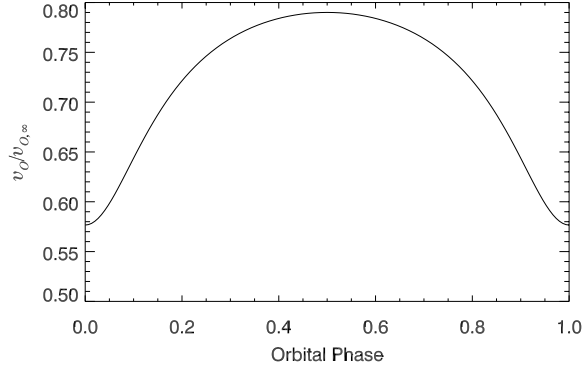


**Figure 5.6:** The ratio of  $v_O$  to  $v_{O,\infty}$  at the location of the compact object in LS 5039, assuming a  $1.4 M_\odot$  neutron star and  $23 M_\odot$  for the O star.

We can find the asymptotic angle of the bow shock,  $\theta_\infty$ , by considering the case where  $R_p(\theta_p)$  goes to infinity. At this limit,  $\theta_p = \pi - \theta_O = \pi - \theta_\infty$ . Therefore,

$$(\pi - \theta_\infty) \cot(\pi - \theta_\infty) = 1 + \eta(\theta \cot \theta - 1) \quad (5.40)$$

and

$$\theta_\infty - \tan \theta_\infty = \frac{\pi}{1 - \eta} \quad (5.41)$$

In order to find the opening angle of the system, I created a program to solve Equation 5.41 recursively with the initial value  $\theta_\infty = \pi$ . For  $\eta = 0.06$ , the opening angle of the shock is  $\theta_\infty = 44.2^\circ$ .

These calculations assume that the stellar wind of the O star has reached its terminal velocity by the time it reaches the shock front. Such an assumption is not true for LS 5039, as the O star wind reaches between 55% and 80% of  $v_\infty$  at the location of the compact object (see Figure 5.6). The problem becomes more difficult to solve if the  $\beta$ -velocity law dependence of the stellar wind is used, and will probably require a numerical solution. For the purposes of this calculation, the assumption of  $v_O = v_{O,\infty}$  should still provides a rough



approximation of the features our radio observations probe. Since we know the speed of the stellar wind at the stagnation point is less than the terminal wind velocity, I also calculated  $\eta$  and  $\theta_\infty$  for  $v = 1200 \text{ km s}^{-1}$  and  $600 \text{ km s}^{-1}$ . This results in  $\eta = 0.12$ ,  $\theta_\infty = 54.1^\circ$  and  $\eta = 0.24$ ,  $\theta_\infty = 65.1^\circ$ , respectively. Since  $\theta_\infty$  is less than  $90^\circ$  in all these cases, the stellar wind of the O star dominates the wind-wind interaction.

### 5.3 Effects of Geometry and Optical Depth

The inclination angle of the system and the opening angle of the shock cone will determine if at any point we are looking down the shock cone, rather than observing the interaction region through the O star wind. We can calculate an estimation of the inclination angle of the system using the value we found for the mass function in Chapter 4 and our estimated masses for the pulsar and the O star. The mass function is given by

$$f(m) = \frac{P}{2\pi G} K_1^3 = \frac{M_p^3}{(M_p + M_O)^2} \sin^3 i \quad (5.42)$$

Solving for the inclination angle yields

$$i = \arcsin \left( \frac{P}{2\pi G} K_1^3 \frac{(M_p + M_O)^2}{M_p^3} \right)^{1/3} \quad (5.43)$$

I used  $K_1 = 19.74 \text{ km s}^{-1}$  (Aragona et al. 2009), an O star mass of  $23 M_\odot$  (Casares et al. 2005) and  $M_p = 1.4, 2.0, \text{ and } 2.5 M_\odot$ . This resulted in inclination angles of  $61.3^\circ$ ,  $38.6^\circ$ , and  $30.4^\circ$ , respectively.

In the case of a  $1.4 M_\odot$  companion, we would expect to be looking into the shock cone near the time of inferior conjunction, which occurs around phase 0.67. This scenario is less likely but still possible for cases with a  $2 M_\odot$  or more massive companion, particularly if the wind speed at the shock is less than half of  $v_\infty$ . Since the properties of the pulsar wind

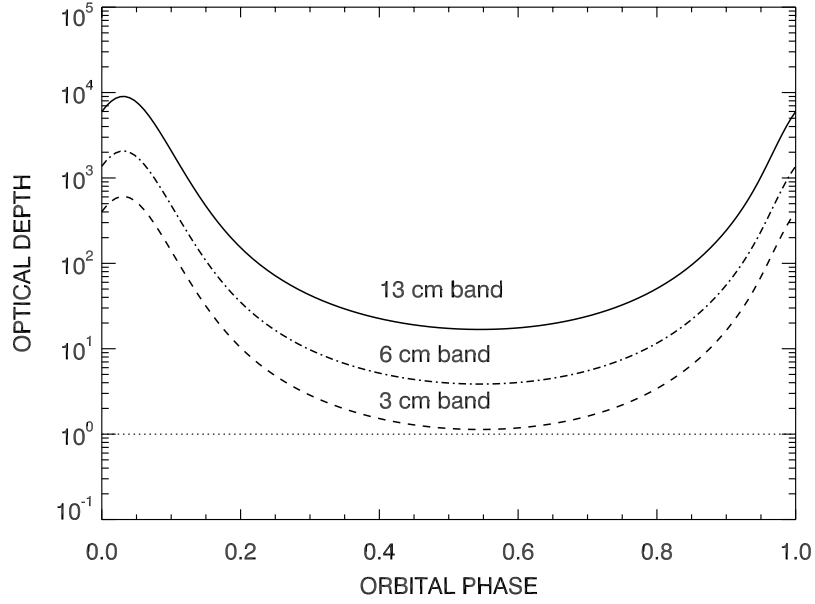


**Figure 5.7:** The optical depth at the location of the stagnation point of the shock for 3 cm, 6 cm, and 13 cm wavelengths. The dotted line indicates  $\tau_\nu = 1$ .

are different from those of the O star, we would expect to see a change in either the radio emission or spectral index at inferior conjunction vs. superior conjunction. Figures 5.1 and 5.2 do not show an obvious change in flux or flux ratios, making such a scenario unlikely.

In reality, the system is slightly more complicated. As the pulsar moves through the O star wind, the expanding shock cone will be stretched into a spiral pattern (for an example using a more widely spaced binary, see Parkin & Pittard 2008). Accurately depicting the emission from this region would require a detailed hydro-dynamical simulation of the wind-wind collision. However, calculating how deeply into the system we can probe with our radio observations is a useful exercise. The optical depth at the location of the stagnation point, as determined in Section 5.2.2, as a function of orbital phase is plotted in Figure 5.7. At no point in the orbit is the optical depth at the stagnation point less than 1. Clearly the

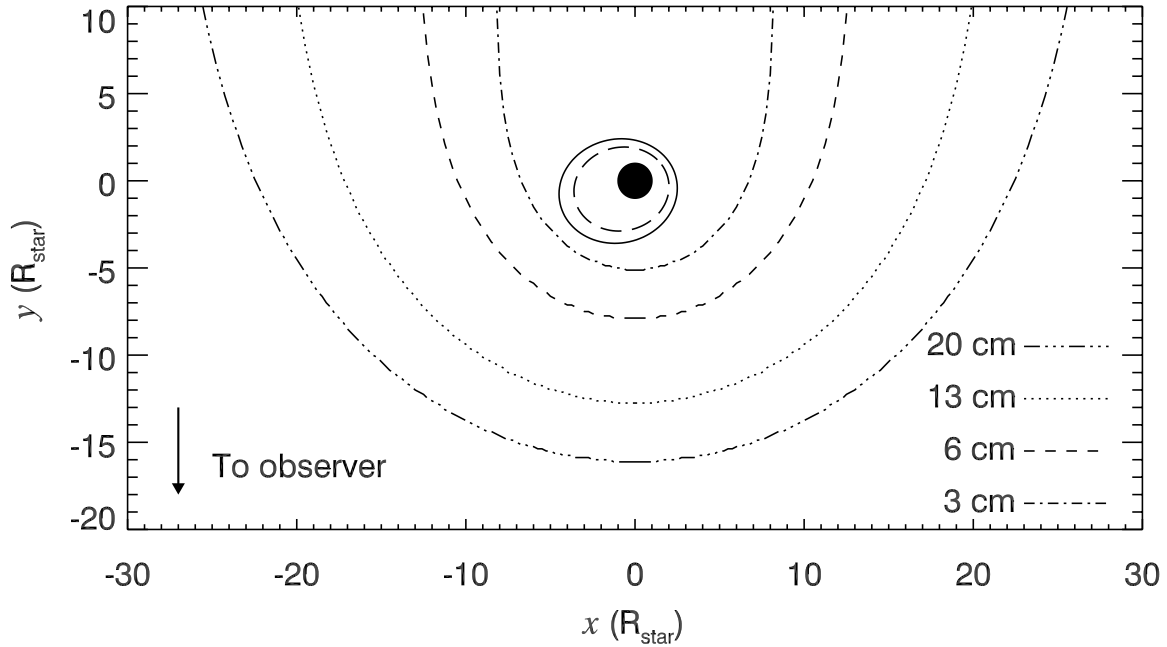


**Figure 5.8:** The optical depth as seen by an observer looking into the O star wind. Each open contour represents the distance from the O star at which the optical depth of the O star wind along the line of sight goes to 1 for radio waves at 20 cm, 13 cm, 6 cm, and 3 cm. The arrow indicates the direction towards the observer. The solid line represents the orbit of the compact object with respect to the O star. The dashed closed contour represents the location of the stagnation point as calculated in Section 5.2.2. The solid circle represents the O star.

stagnation point is deeply embedded in the O star wind at all points in the orbit, and any emission in radio wavelengths must originate from outside this region.

As noted above, we can only observe emission from the system where  $\tau_\nu \leq 1$ . Since the shock region is embedded in the O star wind, we calculated the shape of the surface where  $\tau_\nu = 1$  along the line of sight to the observer to determine the regions in the system where the observed radio emission is produced. In order to accomplish this, I created a program in IDL to calculate the wind density and absorption coefficients (Equations 5.5 and 5.7) over a grid of radial distances from the O star. I used these values to solve numerically for the

optical depth along the line of sight at each grid point using Equation 5.8. The contours where  $\tau_\nu = 1$  for 3 cm, 6 cm, 13 cm, and 20 cm are plotted in Figure 5.8. The optical star is located at coordinates (0,0) and the orbit of the compact object as seen from above is plotted as a solid line. An inclination angle of  $61.3^\circ$  and  $M_X = 1.4 M_\odot$  were assumed for this figure. The stagnation point of the shock front as a function of orbital phase is plotted as a dashed line.

From Figure 5.8, we can see that any emission we are detecting in radio wavelengths must come from beyond the location of the compact object. The 3 cm wavelength band probes deepest into the system, nearing the location of the compact object at apastron. The cooling time of the shocked material will determine where in the system the radio flux is emitted. The gas from the shock will cool as it flows away from the stagnation point. We would, therefore, expect emission at longer wavelengths persist farther out in the system than shorter wavelengths, as less energetic radiation requires less energetic material. We may be able to use the curves of  $\tau_\nu = 1$  to place a lower limit on the cooling time for the system. The lightcurve of the observed radio fluxes is relatively flat, with a possible drop off in flux in the 13 cm band around phase 0.25. This relatively constant flux in the 3 cm and 6 cm wavebands would seem consistent with a spiral shock region cooling to temperatures to generate radio emission farther from the shock region, creating a more uniform emitting surface that has a minimal dependence on orbital period.

The variation in the 13 cm flux is harder to explain, assuming this is a real feature. The compact object and stagnation point are most deeply embedded in the O star wind between phases 0 and 0.25. This feature cannot be easily explained by the system geometry or O star wind optical depth. Changes in the shock front due to periastron passage seems an equally unlikely explanation, as the radio emission we see from the system is not being

generated near the stagnation point. At the surface where  $\tau_\nu = 1$ , I would expect the emitting surface to have a larger area and the emission not strongly correlated with orbital period. A complex hydro-dynamical model of the emission from a colliding wind shock in radio waves will be needed to understand fully the features of the radio light curve. Furthermore, the weakness of any correlations in flux with orbital phases leaves open the possibility of jets from an accreting black hole as producers of the radio emission. Intense modeling of the two scenarios will be necessary to understand this system in detail.

# Chapter 6

## Closing Remarks

In the case of HD 259440, we have found that the optical star has a  $T_{\text{eff}}$  of 27500–30000 K and a  $\log g$  of 3.75–4.0. Using the evolutionary tracks of Schaller et al. (1992), these values result in a mass of 13.2–19.0  $M_{\odot}$  and a radius of 6.0–9.6  $R_{\odot}$ . Fitting archival photometric measurements of HD 259440 to BSTAR2006 and OSTAR2002 model SEDs yields a distance of 1.1–1.7 kpc. We were also able to constrain the orbital period to greater than 100 d due to the lack of detected radial velocity shifts in our collection of spectra for this system.

For LS 5039, we were able to determine orbital parameters, including an orbital period of 3.90608 d and an eccentricity of 0.337. The spectra observed with SOAR indicate an isotropic stellar wind with a mass loss rate of  $\sim 1.9 \times 10^{-8} M_{\odot} \text{ yr}^{-1}$ . The results from our radio data are more ambiguous. The measured fluxes are in the range of 10–40 mJy for the 3 cm, 6 cm, and 13 cm bands and vary with time. The optical depth at radio wavelengths indicates that the fluxes we are observe should be generated from farther out in the system than the orbit of the compact object. The results from our simplified model of a wind shock region in LS 5039 do not explain the observed data. At the same time, the model is still too

general to rule out the wind-wind collision scenario.

Since this work was started, several new results have been published for both HD 259440 and LS 5039. In a recent paper posted to arXiv.org, Bongiorno et al. (2011) report that peaks in the X-ray light curve of HD 259440 show a periodicity of about 320 days, which concurs with our conclusions in Aragona et al. (2010) that the orbital period is  $> 100$  d. They also observed secondary peaks around the midpoint of this cycle. The observations of HD 249550 we obtained using the KPNO Coudé Feed telescope overlap this midpoint in the variability of the X-ray light curve. While we saw no radial velocity shifts in any of our observations, we did observe variation in the  $H\alpha$  line profile. We were able to highlight this feature by averaging the full set of  $H\alpha$  spectra and subtracting this average from each observation. The variation seems to follow a spiral pattern with a possible periodicity of about 60 days (see in Figure 6.1; Aragona et al. 2010). We initially interpreted these observations as evidence of a spiral density wave in the Be star disk, although the new X-ray results leave these observations open to interpretation. Another observing run at the KPNO Coudé Feed is planned for 2011 December, which will coincide with the next strong X-ray peak in the 320 day period.

Sarty et al. (2011) have published a paper addressing the orbital parameters in LS 5039. Their orbital period is consistent with my own (Aragona et al. 2009) and that of Casares et al. (2005), but they find a lower eccentricity of about 0.24, compared to our value of 0.337. They also report variability in the equivalent width of several absorption lines, most notably in the  $H\beta$  and He I  $\lambda$  5775 Å lines. Their observations appear to support the focused wind stream scenario. Meanwhile, the debate on the identity of the compact object and the  $\gamma$ -ray production mechanism continues. Recent X-ray observations by Durant et al. (2011) show a region of extended emission which could be explained either by a pulsar wind nebula or

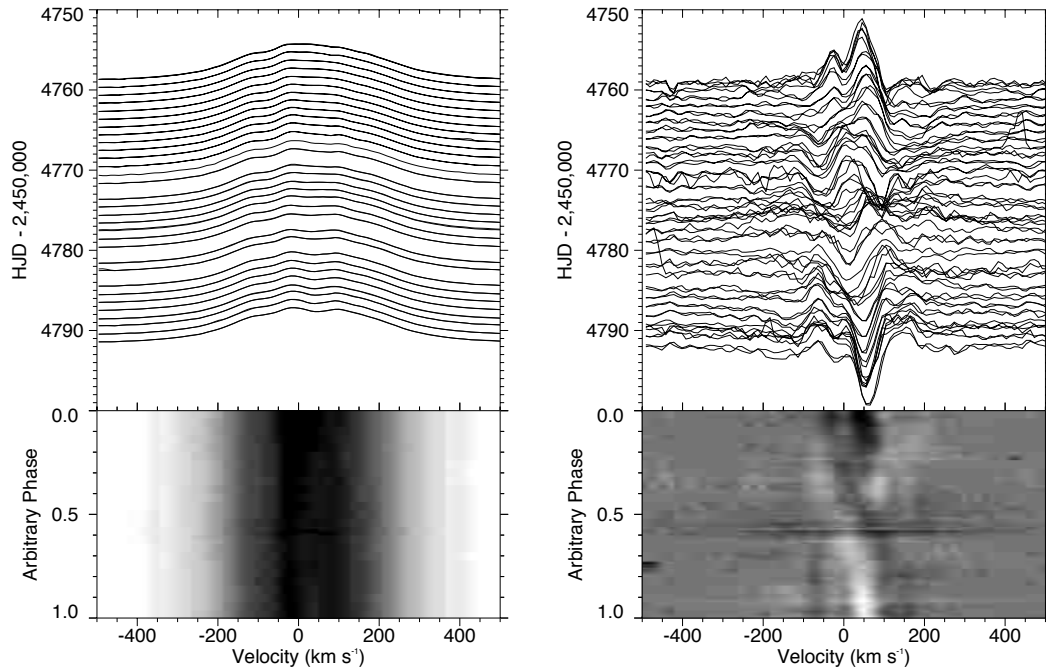


**Figure 6.1:** (Left) The upper portion of the plot shows the  $H\alpha$  line of HD 259440 as observed on 35 consecutive nights with the KPNO CF telescope from 2008 October to November, sorted by HJD. The lower portion of the plot shows a gray scale image produced by a linearly interpolating between the observed spectra. Since no period was known at the time of our publication, the “Arbitrary Phase” goes from 0 at the start of the observing run to 1.0 at the end of the run. The intensity at each velocity in the gray-scale image is assigned one of 16 gray levels based on its value between the minimum (bright) and maximum (dark) observed values. (Right) The upper panel shows the  $H\alpha$  residual spectra of HD 259440, and the bottom panel shows a grayscale plot of the same residuals. The residual spectra were calculated by creating a reference spectrum from the average of all 35 nights of observations and subtracting this average from each individual observation. The residual spectra reveal variations in the  $H\alpha$  line with a  $\sim 60$  d period that we attribute to a spiral density wave in the circumstellar disk.

a dust scattering nebula. Their analysis favors a pulsar wind nebula but is not conclusive. Their results also have implications for the geometry of the observed radio emission from LS 5039, as we would expect this to be produced even farther out in the system.

I plan to revisit the 20 cm data set to see if I can produce more accurate reduced fluxes.



We should be able to draw some conclusions about the production mechanism for the radio emission by comparing the radio SED at different orbital phases with predictions from models of both the pulsar wind scenario and the microquasar model. Detailed hydrodynamical simulations will ultimately be needed to predict the behavior of radio observations in each case. There are research groups that have such models in some stages of development (private communication with Stan Owocki), so exploring opportunities for collaboration will probably be the most useful way to pursue this line of inquiry. Once we can predict the behavior of the radio light curves and SED in each scenario, we can reassess if our radio observations provide sufficient orbital coverage to constrain the nature of the interaction region in LS 5039. If more observations would be useful, the results of detailed modeling could be used to make a compelling case for new observations of the system with improved orbital coverage.

# Appendix A

## Radio Data Reduction for LS5039 using MIRIAD and KARMA

This appendix is a “cookbook” for reducing the LS 5039 radio data taken with the ATCA before June 1, 2009. It does not address how to reduce data taken with the new CABB detectors installed in the spring of 2009. MIRIAD is a standard radio data reduction package for ATCA. The package and documentation are hosted at <http://www.atnf.csiro.au/computing/software/miriad/>. KARMA (Gooch et al. 1996) is an image viewer which handles the format of images output by ATCA. The package and instructions for installation can be found at <http://www.atnf.csiro.au/computing/software/karma/>.

### A.1 Anatomy of an Observation

Each observation consists of a primary calibrator, a secondary calibrator and the target source. The primary calibrator is a well observed, bright radio point source that can be used to determine the instrumental parameters such as gain, polarization, and bandwidth. The secondary calibrator is a bright source located near the target object whose properties are

known, although not as well as the primary calibrator, which is used to adjust for changes in the telescope calibration over the duration of the target observations. In the case of the radio observations of LS 5039, these objects are:

Primary Calibrator: ICRF J193925.0-634245, which is labeled 1934-638 in ATCA's databases

Secondary Calibrator: PMN J1825-1718, which is labeled 1822-173 in ATCA's databases

There are two pointings in this data set, one for the 20 cm and 13 cm wavelengths, the other for the 6 cm and 3 cm wavelengths.

### **Definitions**

Gain – overall way the telescope amplifies flux.

Bandwidth – the range of frequencies within the telescope response.

Polarization – radio telescopes detect light as either some combination of left and right circular polarizations, or two orthogonal linear polarizations.

## **A.2 Calculating Field of View**

The field of view, also called the primary beam size, of a radio telescope or array depends on the diameter of the radio dishes and the frequency at which the observations are taken. We can calculate this value by taking  $1.22\lambda/d$  where  $d$  is the dish diameter, which yields the field of view in radians. For the observations of LS 5039, images taken at the 20 cm wavelength will have the largest field of view and those at the 3 cm wavelength will have the smallest. We also need to determine the synthesized beam size. This is calculated as  $\lambda/D$ , where  $D$  is your longest baseline. These values are used to set the image and cell size when converting the telescope visibilities to an image.

### A.3 KARMA and kvis

Within the KARMA package, **kvis** is an image viewer like DS9 (for X-ray or optical astronomers). It can directly read MIRIAD files, which DS9 cannot do. Open an X11 xterm or similar terminal. First, move to the directory where you would like to store any edits you make in **kvis**, since the program will save everything in the directory where you open it. To enter a c-shell, type

```
> csh
```

next, type

```
> kvis
```

to start **kvis**.

To open images in **kvis**, click on the grey “Files” button in the upper left hand corner of the **kvis** window. Use the screen that pops up to navigate to the directory where your images are stored, then click on the image you wish to display. At this point, the file window will disappear. You can restore it by clicking on the “Files” button again. If you want to force the file window to stay, select the “pin” option at the bottom of this window.

Once you have selected an image to examine, a browse window will appear containing a list of all the images you have loaded into **kvis** and options for manipulating the image. To display an image from the list, place your mouse over the name of the image you wish to view and press “i”. The image that is currently being displayed is marked by the letter “P” to the left of the image name. If you want to adjust the contrast of the image, click on the image name to select it from the list. The image name will be highlighted by a black bar. Click the “Histogram” button to bring up an Intensity Zoom window. The yellow box

indicates the maximum and minimum intensity values displayed in your image. You can toggle the right side of this box by holding down the “command” key and using the mouse. The left side of the box can be shifted by using the “ctrl” key and the mouse. The entire box can be shifted by holding down the “alt” key and clicking with the mouse. You can also manipulate the image or find additional help by selecting the window with the image display and using the following commands:

? lists possible commands (the list does not have everything)  
ctrl + i toggles display between images  
o zoom out  
i zoom in  
s statistics (simply typing ”s” will do this for the entire screen,  
or you can draw a box and click s before releasing  
the mouse to specify an area)

## A.4 MIRIAD

MIRIAD files are actually directories, so removing them requires the following command:

```
> rm -rf filename
```

BE VERY CAREFUL WITH THIS COMMAND. It is a recursive remove, and will take out ALL the files in the named directory and lower.

The data files you will be using are saved with names in the form DATE\_TIME.PROPID#. For example, a raw data file from October 15, 2008 has the file name 2008-10-15\_0219.C1863. MIRIAD will not overwrite the original data, but rather create new files with the modifications made to the data set. These files include the following:

gain – contains information on gain calibrations

leakage – contains information on polarization calibration

bandpass – contains information on bandpass calibration

history – contains information of what you have done up to this point in the reduction process

To start MIRIAD, create an initialization script. Create a file named `mirscript` in a text editor (like `pico`, for example) and enter the commands:

```
source $MIR/MIRRC.sh
export PATH=$MIRBIN:$PATH
miriad
```

Alias the program by adding the following lines to the `.bashrc` file:

```
MIR=/Applications/miriad
export MIR
alias mirstart = 'source /Users/aragona/mirscript'
```

The first line saves the location where MIRIAD is located on your computer to the variable `MIR`. The second line exports the address and tells the computer where to find MIRIAD. The last line assigns a command to `mirstart`, so that when you enter this word into the command line, the computer will find and run the MIRIAD initialization script. To start MIRIAD, simply type `mirstart` on the command line.

For the rest of this guide, italicized words will indicate a variable that you fill in as is appropriate for your purposes. The `#` sign will indicate a place where you can choose a number. In Miriad, you can call commands in several ways. Typing

```
> inp task
```

calls that task and will fill in values for the parameters as available from previously called tasks. For example, if I want to call the **blflag** task, I can type

```
> inp blflag
```

and the computer will output:

```
Task:    blflag
vis      =
line     =
device   =
stokes   =
select   =
axis     =
options  =
```

This confirms the name of the task and lists the parameters. This particular task has no values assigned to the parameters, as evidenced by the blank spaces after each line. The parameter `vis` requires an image file as the input. We can assign this parameter by typing

```
> vis = ls5039_2013.4800
```

If we type

```
> inp
```

again, then MIRIAD will output

```
Task:    blflag
vis      = ls5039_2013.4800
```

```
line      =  
device    =  
stokes    =  
select    =  
axis      =  
options   =
```

As you can see, the parameter `vis` has been assigned a value. Once you have set the parameters, you can run the task by typing

```
> go
```

The function of **blflag** will be described later in this manual.

Typing

```
> tget task
```

calls the task with the same values as the last time you used it. These parameters will be saved in a file called `task.def` in the directory you are working in. For a general description a parameter, type

```
> help parameter
```

For task specific descriptions of that parameter, type

```
> help k parameter
```

Typing

```
> unset parameter
```

will clear the values from that parameter.



The reduction of this radio data will take place in two parts. The first part of the process will deal with data in the *uv* plane, known as visibilities, and set the calibrations for your observing set up. The second part will construct an image of the source from the calibrated visibilities. For our purposes, we should be able to automate the second part of this process, once we have worked out a sequence of commands that yield good results on one data set. For further details on the first part of the reduction process, see Chapter 8 in the MIRIAD manual for a flowchart specifying the appropriate options for several reduction scenarios . For the following instructions, assume that if a parameter is not listed under the task name or in the task description, it is left empty when running the task.

To load data into MIRIAD, use the **atlod** task. For example, the inputs for **atlod** for data taken on the night of October 15, 2008 will look like:

```
Task:   atlod
in      =  2008-10-15_0219.C1863,$
        2008-10-15_0226.C1863,2008-10-15_0343.C1863
out     =  ls5039.atlod
ifsel   =
restfreq =
options =  birdie,reweight,xycorr
nfiles  =
nscans  =
```

The values for `in` are the raw data files, and will be different for each set of observations. The parameter `out` holds the name of the output file. Setting `option = birdie` tells the program to flag RFIs (or radio frequency interference). Next, split the data into files containing the primary calibrator, the secondary calibrator, and the source using **uvsplit**.

```
Task:   uvsplit
vis     = ls5039.atlod
select  =
options =
maxwidth =
```

**uvsplit** will output a set of files with names in the form of *source.frequency*. This will result in 12 new files. Files beginning with 1934-638 will all be associated with the primary calibrator. Files beginning with 1822-173 all contain data on the secondary calibrator, and files starting with ls5039 contain data on the target. The 20 cm observations correspond with files ending in 1384, the 13 cm observations correspond to files ending in .2368, the 6 cm observations correspond to files ending in .4800, and the 3 cm observations are in files ending in .8640. For example, the files for the 20 cm data will be labeled 1934-638.1384, 1822-173.1384 and ls5039\_2013.1384.

Next, flag and calibrate the primary. Flagging an observation means that you will examine each set of visibilities for evidence of noise or interference and indicate that MIRIAD should ignore these data points. Use the task **blflag**.

```
Task:   blflag
vis     =
line    =
device  =
stokes  =
select  =
axis    =
options =
```

Set the parameter

```
> device = /xs
```

Set `vis` as one of the primary calibrators

```
> vis = 1934-638
```

You also need to set the axes for graphing your data. In this case, we will choose amplitude for the y-axis and time for the x-axis by entering

```
axis = time,amp
```

For this step, just look at the polarizations `stokes = xx` and `stokes = yy`. A basic set of inputs to **blflag** might look like

```
Task:   blflag
vis     = 1934-638.1384
line    =
device  = /xs
stokes  = xx
select  =
axis    = time,amp
options = nobase
```

`options = nobase` means that all the baselines will be displayed on the same plot. To remove this setting and examine the baselines individually, type

```
> unset options
```

**blflag** provides several options for choosing points to reject. You can click on points individually, in which case they will turn red to indicate the flagging. For a cluster of bad visibilities, you can draw a box around the unwanted points. Type “p”, click the mouse to define the vertices, and then type “x”. A green box will appear around the rejected points. Typing “q” will let you quit **blflag** without saving your flags, while typing “c” will allow you to clear the screen of flagging and start over. The calibrators are not polarized, so Stokes parameters for polarized fluxes (Q, U, and V) should be grouped around zero, while the I stokes parameter (total flux) should match that of the calibrator. Short baselines will display the most flux as they are able to detect more diffuse emission. The bandwidth of each observation is split into 13 frequency channels. To flag individual channels, use

```
> line = channels,1,#,1,1
```

where # is a number between 1 and 13. If you need to unflag anything, you can use **uvflag**.

Next, calibrate for gain, bandpass, and polarization. **mfc** and **gpc** create the gains, leakages, and bandpass files, which are stored inside the image directory. You should use the recommended options from Figure 12.3 in the manual. The interval and tolerance can be adjusted, although we used the default for tolerance and an interval of 1 when working with the 20 cm data. You want the leakage values to be less than 0.1 here, as the primary source is effectively unpolarized.

```
Task:    mfc
```

```
vis      = 1934-638.frequency
```

```
line     =
```

```
stokes   =
```

```
edge     =
```

```
select   =
```

```
flux      =  
refant    = #  
minants  =  
interval = 1  
options  =  
tol      =
```

`refant` specifies the reference antenna. Ideally, this should be an antenna near the center of the array that is functioning throughout the observation without severe interference. ATCA has 6 antennas, so I usually try to use antenna 3 or 4 for `refant`.

```
Task:    gpcal  
  
vis      = 1934-638.frequency  
select   =  
line     =  
flux     =  
refant   = #  
minants  =  
interval = 1  
tol      =  
xyphase  =  
options  = xyvary
```

After calibrating, check that the solution is reasonable using **uvplt** and **gpplt**. **gpplt** will let you look at the bandpass, gain, and leakage files. You want to check amplitude vs.

frequency, gain vs. time, bandpass vs. frequency (**gpplt**), and plot the polarizations on the imaginary vs. real axis (**uvplt**):

Task: gpplt

vis = 1934\_638.frequency

device = /xs

log =

yaxis =

options = bandpass

nxy =

select =

yrange =

Task: uvplt

vis = 1934\_638.frequency

line =

select =

stokes = i,q,u,v

axis = real,imag

xrange =

yrange =

average =

hann =

inc =

```
options = nobase,equal
subtitle =
device = /xs
nxy =
size =
log =
comment =
```

You can set the `options` parameter in **uvplt** to some combination of `nobase` (show all baselines on one plot) and `equal` (sets equal scales for both axes). The goal for the calibration should be that gain and bandpass vary smoothly and are close to 1. If you are not satisfied with your calibrations, you can delete the bandpass, leakage, and gain files and start again.

Copy the calibration information over to the secondary calibrator using **gpcopy**.

```
Task: gpcopy
```

```
vis = 1934-638.frequency
```

```
out = 1822-173.frequency
```

```
mode =
```

```
options =
```

Use **blflag** again to flag the secondary calibrator by calling

```
> tget blflag
```

```
> vis = 1822-173.frequency
```

This time, examine polarizations v, q, u, and i by calling

```
> stokes = v
```

etc. There should be no significant v polarization since most astronomical sources are not strongly polarized.

After flagging, perform the calibrations on the secondary calibrator. When you run the calibrations for the secondary, it will use the calibrations from the primary calibrator as an initial guess. If **gpcal** gives NAN (not a number) you will need to delete the calibration files and try again. Diffuse emission around the secondary calibrator will be detected at very short baselines, so we want to exclude these for the 20 cm and 13 cm observations. The **select** parameter allows you to choose which baselines to include in your calibration. When you call **gpcal**, choose your baselines by setting

```
> select = uvrange(2,30)
```

for the 20 cm observation and

```
select = uvrange(2,60)
```

for the 13 cm observation. The values in the **uvrange** variable are in units of thousands of wavelengths. So setting **uvrange(2,30)** places an inner limit on the baseline length of 2,000 times the wavelength of your observations and an outer limit on the baseline length of 30,000 times the wavelength of your observations. This will exclude the innermost 1 km of baselines in the array.

**Task:** `gpcal`



```

vis      = 1822-173.frequency
select  = uvrange(##)

line    =

flux    =

refant  = #

minants =

interval = 1

tol     =

xyphase =

options = xyvary,qusolve,nopol

```

Of the commands for `options`, `qusolve` could potentially have a problem since we do not have good parallactic angle coverage. Make sure the solution is reasonable. `gpca1` will output a %Q and %U: check that these are reasonable percentages for the polarization. Again, examine results using **gpplt** and **uvplt**. If everything looks ok, finish the calibrations by performing

```

Task:    gpboot

vis      = 1822-173.frequency
cal      = 1934-638.frequency
select  =

```

Check the inputs for `vis` and `cal`. Be very careful that they are correct, or you will ruin your calibrations.

Copy calibration files from the secondary calibrator to the target using **gpcopy**. Now, flag the source using **blflag**. Check the range of polarizations (v,q,u,i), channels, etc. as you did for the secondary calibrator. Apply the calibrations to the source using **uvaver** with the parameters set as follows:

```
Task:   uvaver

vis     = ls5039_wavelength.frequency
select  =
line    =
ref     =
stokes  =
interval =
options =
out     = ls5039_wavelength.uvaver
```

Now, we begin the second part of the calibrations. For the sake of simplicity in the notation, I will outline the reduction process for the 20 cm case. To use this procedure for other wavelengths, simply change the name of the files accordingly. For example, ls5039\_20.uvaver would become ls5039\_13.uvaver for the 13 cm case. Use **invert** on the observed visibilities to create a dirty map and a beam model. After calling the task, set

```
> select = ant(6)
```

to use only baselines with antenna 6. For the 20 cm case, the input parameters for **invert** might look like

```

Task:    invert
vis = ls5039_20.uvaver
map = ls5039_20.imap
beam = ls5039_20.b
imsize  = 3535
cell    = 1.5
offset  =
fwhm    =
sup     =
robust  =
line    =
ref     =
select  = ant(6)
stokes  =
options = mfs,systemp,double
mode    =
slop    =

```

You will also need to choose a weighting scheme. This is determined by the `fwhm`, `sup`, and `robust` options. The options will allow you to choose a weighting somewhere between the extremes of natural and uniform weighting. Natural weighting is more sensitive to point sources, but results in worse sidelobes. Uniform weighting offers the best side lobe suppression. I have used a weighting of `robust = -0.5`. `invert` uses a fast fourier

transform, so avoid setting the `imsize` to a factor of two, as this could result in weird artifacts in your image. Choose the cell size using the synthesized beam. You generally want to have 3 to 5 pixels across the synthesized beam measuring from somewhere between the edge of the first min of the beam and the FWHM of the central peak. Cell size is entered in arcseconds. You want the image size to span the entire primary beam, so use your cell size to calculate a good value for this. `mfs` stands for multi-frequency synthesis, which you will need to use for this set of observations. The **clean** program will aim for the theoretical noise level listed in the output of **invert**.

After you run **invert**, clean your image to model the beam. The `gain` parameter will allow you to determine how large of a step the **clean** program takes between iterations. Generally, you want this to be between 0.05 up to 1.2 or 1.5. For the 20 cm case, input parameters for `clean` will look like

```
Task:    clean
map      =  ls5039_20.imap
beam     =  ls5039_20.b
model    =  ls5039_20.icln
out      =
gain     =
options  =  positive
cutoff   =
niters   =  10,000
region   =  20cm.reg
phat     =
minpatch =
```

```
speed    =  
mode     =  
clip     =
```

The input for the `map` parameter is the `.imap` file created by `invert`. **clean** will create model of the point source and store it under the file name specified by the `out` parameter. Setting `options = positive` prevents **clean** from using negative values for the flux. `niters` specifies the number of iterations for **clean** to use, and `region` sets the region file.

Next, restore the image. To do this, **restor** will convolve your model (`ls5039_20.icln` in this example) with the beam (`ls5039_20.b`) and subtract the result from the dirty map. The residual will be added to the model (`ls5039_20.icln`) to make sure all the point sources were taken into account. The new model that results will be convolved with the nominal beam (a gaussian based on the actual beam) to create the cleaned image (`ls5039_20.iimg`).

```
Task:    restor  
model    =  ls5039_20.icln  
beam     =  ls5039_20.b  
map      =  ls5039_20.imap  
mode     =  
fwhm    =  
pa       =  
out      =  ls5039_20.iimg
```

You can redefine regions using the **cg curs** function:

```
Task:    cg curs
```

```
in      = ls5039_20.iimg
type    =
region  =
xybin   =
chan    =
slev    =
levs    =
range   =
device  = /xs
nxy     =
labtyp  =
options =
3format =
csize   =
```

Set

```
> options = region
```

so that you can select the region using the mouse The program will create a file called `cg curs.region`. Concatenate this with the `20cm.reg` file by using the **cat** command.

```
> cat cg curs.region 20cm.reg > new.reg
```

Then copy to the `20cm.reg` file by using

```
>mv new.reg 20cm.reg
```

You can use **imfit** to determine the center of the gaussian fit to your solution and make sure that it agrees with the actual coordinates of your source and other nearby objects.

```
Task:  imfit
in     =  ls5039_20.iimg

region = boxes(x1,y2,x2,y2)

clip   =

object = g

spar   =

fix    =

out    =

options =
```

Pick a region to zoom in around LS 5039 so that you can tell **imfit** where the source is. Use **kvis** to open `ls5039_20.iimg` and zoom in on the source. Set your cursor in the lower right hand corner of the image and record the x and y coordinates. We will call these  $x1$  and  $y1$ . Move the cursor to the upper left hand corner of the image and record the coordinates again; these are  $x2$  and  $y2$ . Then set `> region = boxes(x1,y1,x2,y2)` Setting `object = g` tells **imfit** to fit the source with a gaussian. Set `object = p` to fit the source with a point source. You can also fit with combinations of functions, such as a gaussian and a flat background: `object = g,l`. However, for this you need to set `spar` equal to initial guesses for each parameter. For details, open the **imfit** task and type

```
> help -k spar
```

Always try `object = g` or `p` first and use the results from this to estimate values for `spar`. **imfit** will give you the central coordinates for your gaussian, so you can check to see if the point source is located at the correct right ascension and declination. You can also look at the `.icl` file to see how the **clean** program is distributing the flux in your model field (you want it to be simulating a point source). If the location of your region looks appropriate, you can then tighten the region to improve the model. Each time you make a new region file, you need to save the output to a new `.icl` file. Delete the old one using `rm -rf` and rerun **clean**.

Continue to **clean** and **restor**, adjusting your regions, until you are satisfied. At this point, you can run your first self calibration. You want to start by self calibrating for PHASE ONLY.

```
Task:    selfcal
vis      = ls5039_20.uvaver
select  = ant(6)
model    = ls5039_20.icl
clip     =
interval = 2
options  = mfs
minants  =
refant   = 6
flux     =
offset   =
line     =
```

Rerun **invert**, incrementing the label for the dirty map to `.imap2`. The beam files are very



large, so at this point, you can delete the .b (beam) file. You should save the .imap file so you can see if your model is actually improving. Also, if your latest iteration makes things worse, you can always revert back to using the previous model.

After inverting your image, run **clean** again. This time, you can use your old model as a starting point for the clean iterations: `model = ls5039\_20.ic1n`. Continue the cycle of **invert**, **clean**, **restor**, and **selfcal** until you are satisfied with your fit. Before you take your measurement, or if you want to check that the fluxes you are measuring seem reasonable at any point during the process, you must use **linmos** to gain correct the image for the size of the beam.

```
Task:   linmos
in      =  ls5039_20.iimg
out     =  ls5039_20.gcimg
rms     =
options =
```

In order to determine your error, create a residual map as your output when running **imfit**. Look at the area around your point source. There should be no weird residuals, such as leftover flux from the point source. The background should have a total flux close to zero, and you should not see the flux within any box you draw in this region increasing with the size of the box. To estimate your error, open the final, fully reduced .gcimg file in kvis. Hold down the left click button and move your mouse to create a box and press 's' before releasing the mouse. The statistics for the flux within that box should be displayed in the xterm window where you opened kvis. By drawing boxes of various sizes around the

target and noting the variations in flux, you can estimate the error in your measurements.

You want this to be about 1 to 3 mJy.

## Appendix B

# Programs Used in Analyzing the Radio Observations of LS 5039

The following chapter includes programs I have written to examine the orbital features of LS 5039, the optical depth of the system, and the relationship to the radio observations. All programs can be run using IDL.

### B.1 Wind Speed

The following program calculates the windspeed at the location of the compact object as a function of orbital phase.

```
pro windspeed,vinf,P,ecc,m1,m2,rspeed

; Calculates wind speed as fraction of terminal
; wind velocity at location of compact object
;
; rsep    = separation distance of sources in meters
```

```

; rspeed = windspeed at rsep in km/s
; vinf   = terminal wind velocity
; Rstar  = stellar radius in solar radii

beta = 1.
Rstar = 8.5
vinf = 2440.

P = 3.90608
ecc = 0.337
m1 = 23.
m2 = 1.4

;Calculate the orbital separation using orbsep.pro, see below
orbsep,P,ecc,m1,m2,eta,phi,time,phase,rsep

rsep2 = rsep/(6.95508e8) ;rsep in solar radii

;Create plot of windspeed as a function of Orbital Phase
set_plot,'ps'
device,/landscape,filename='windspeed.ps'
device,/inches,xsize=7.,ysize=5.
;window,xsize=400,ysize=400
!x.thick=3

```

```

!y.thick=3
!p.thick=3
!p.font=1
!p.charsize=2
!x.style=1
!y.style=1
!x.range=[0.,1.]
!y.range=[0.5,0.8]
!x.title='Orbital Phase'
!y.title='!8v!Dw!N/v!Dw,inf!N!3'
!x.margin=2.
!y.margin=2.

rspeed = vinf*(1.-(Rstar/rsep2))^beta

plot,phase,rspeed/vinf

device,/close
set_plot,'x'
cleanplot,/silent

return
end

```

@/Users/Shared/Programs/Radio/orbsep

## B.2 Orbital Separation

This program calculates the orbital separation between two objects as a function of orbital phase.

```
pro orbsep,P,ecc,m1,m2,eta,phi,time,phase,rsep

;Calculates orbital separation between LS 5039
;and the compact object
;
; Input:
;   P    = orbital period in days
;   ecc  = eccentricity
;   m1   = mass of star in solar masses
;   m2   = mass of compact object in solar masses
; Output:
;   eta  = eccentric anomaly
;   phi  = true anomaly
;   time = time since periastron in days
;   rsep = separation distance in meters

;Constants
```

```

Msolar = 1.9891e30 ; kilograms
G = 6.673e-11 ; Newtons m^2/kg^2
dsec = 86400. ; length of a day in seconds
eta = findgen(101)*2.*!pi/101. ;eccentric anomaly
phi = acos((cos(eta)-ecc)/(1-ecc*cos(eta))) ;true anomaly

;Calculates time since periastron for each value of eta

tgrid = n_elements(eta)
time = dblarr(tgrid)

for i=0,tgrid-1 do begin
time(i) = P*(eta(i)-ecc*sin(eta(i)))/(2.*!pi)
endfor

;Phase at each value of eta
phase = time/P

;Separation distance for each value of eta
rsep = ((G*(m1+m2)*Msolar*(P*dsec)^2.\$
/(4.*!pi^2.))^(1./3.))* (1.-ecc*cos(eta))

;plots orbital separation as a function of orbital phase
plot,phase,rsep

```

```
return
end
```

### B.3 Shock Geometry

This program calculates the location of the shock front and the opening angle.

```
pro shockgeom,enom,phi,time,phase,rsep,R0,RO,oa

; Calculates shock geometry around orbit
; Inputs:
;   MdotO = massloss rate of O star
;   vinfO = terminal velocity of O star wind
;   Edot  = spindown energy of Pulsar;
; Outputs:
;   R0 = distance of stagnation point from neutron star
;   RO = distance of stagnation point from O star
;   oa = opening angle

; General Constants
c      = 2.9979246e8 ; speed of light in m/s
Rsun   = 6.95508e8   ; Solar radius in m
Msun   = 1.9891e30   ; Solar mass in kg
secperyear = 3.15576e7 ;Number of seconds in a Julian year
```



```

;Orbital and Stellar Parameters
P = 3.90608      ;Period of Orbit
; - Aragona et al. 2009
ecc = 0.337      ;eccentricity of orbit
; - Aragona et al. 2009
m1 = 23.         ;Mass of O star in solar masses
; - Casares et al. 2005
m2 = 1.4         ;Mass of compact object in
; solar masses - assume NS
ROstar = 8.5     ;Radius of O star in solar radii
; - McSwain et al. 2004

MdotO = 1.9e-8   ;Mass loss rate of O star in
; solar masses - SOAR Halpha eqws
vinfo = 2440.    ;Terminal wind velocity of
; O star - McSwain et al. 2004
Edot = 5.26e35   ;erg s-1 - Estimated comparing
; X-ray flux of PSR B1259-63 with LS 5039

; run orbsep to get orbital parameters
orbsep,P,ecc,m1,m2,enom,phi,time,phase,rsep

; Convert separation distance to solar radii

```

```

rsep2 = rsep/Rsun

nstep = n_elements(rsep2)

R0 = dblarr(nstep)      ;stagnation point
R0 = dblarr(nstep)      ;distance of stagnation point
; from 0 star in solar radii
beta2 = dblarr(nstep)  ;ratio of of momenta for
; stellar/pulsar winds

eta = (Msun/Edot*1.e7)*(Mdot0/secperyear)*vinf0*1000.*c
print,eta
print,'eta = ',1./eta

for i = 0,nstep-1 do begin
R0(i) = rsep2(i)/(1+eta^(-0.5))
R0(i) = rsep2(i)-R0(i)
endfor

;Calculate opening angle
oa = dblarr(101)
oa(0) = !pi;/4.
for l = 0,99 do begin
oa(l+1) = atan(-!pi/(1.-eta) + oa(l))

```

```

endfor

print,'opening angle (deg) = ', oa*180/!pi

;Plots the location of the stagnation point as
;a function of orbital phase
set_plot,'ps'
device,/landscape,filename='StagPoint.ps'
!x.thick=3
!y.thick=3
!p.thick=3
!p.font=1
!p.charsize=3.
!x.style=1
!x.ticks=4
!x.minor=9
!x.range=[0.0,1.0]
;!x.tickv=[5045.,4045.,4046.]
!y.style=1
!y.range=[0,50]
;!p.charsize=2.0

!x.title='Orbital Phase'
!y.title='Distance from O star (R!Dsolar!N)'
```

```

;!p.title='Spectral Index vs Time'
!x.margin=[2.75,0.5]
!y.margin=[1.50,0.5]

plot,phase,rsep2,linestyle=1 ; location of compact object
oplot,phase,RO ; location of stagnation point

device,/close
set_plot,'x'
cleanplot,/silent

return
end

@/Users/Shared/Programs/Radio/orbsep

```

## B.4 Optical Depth

The following program calculates the location in the O star wind where the optical depth is equal to 1 along the line of sight and produces a plot.

```

pro optdepth1

; For calculations, all units must be converted to cgs
; Constants and stellar parameters

```

```

c = 2.9979e10 ; speed of light in cm/s
lambda = [20.,13.,6.,3.] ; wavelength in cm
nu = c/lambda ; frequency in Hz

Rsun = 6.9598e10 ; cm
Rstar = 8.5 * Rsun ; cm

temp = 37500. * 0.67 ; wind temperature

Mdot = 1.906e-8 ; in Msolar/year from SOAR
Msun = 1.989e33 ; solar mass in grams
Mdot2 = Mdot * Msun / 31557600. ; grams/s

mH = 1.673532499e-24 ; grams
mp = 1.672621637e-24
me = 9.10938215e-28
mu = (mp + me)/(mH*2.) ; mean atomic mass in mH

Z=1

gammae = 1

gnu = dblarr(4)
gnu1 = dblarr(4)

```

```

for m = 0,3 do begin
gnu(m) = 10.6+1.9*alog10(temp)-1.26*alog10(nu(m)*Z)
endfor

xgrid = findgen(201)*50*Rstar/200.
ygrid = (findgen(401)-200.)*Rstar*50./400.
rgrid = dblarr(201,401)

temp = 37500. * 0.67 ; wind temperature in K

;Calculate wind speed at each point in the wind

vinf = 2440. ; km/s

steps = n_elements(lambda)

vrgrid = dblarr(201,401)
density = dblarr(201,401)
kgrid = dblarr(201,401,steps)
taugrid = dblarr(201,401,steps)
tau1 = dblarr(201,steps)

for x = 0,200 do begin
for y = 0,400 do begin

```

```

rwind = sqrt(xgrid(x)^2.+(ygrid(y))^2.)
rgrid(x,y) = rwind
vwind = vinf*(1.-(Rstar/rwind))
vrgrid(x,y) = vwind
density(x,y) = Mdot2/(4.*!pi*rwind*vwind*100000.)/rwind
for lam = 0,steps-1 do begin
; calculate free-free absorption for each gridpoint
kgrid(x,y,lam) = (1.78e-2*Z^2.*gnu(lam)*density(x,y)*$
gammae/(nu(lam)^2.*temp^(3./2.))*$
mu^2.*mH)*density(x,y)/mH
endfor
endfor
endfor

; calculate optical depth for each gridpoint
for i = 0,200 do begin
for j = 0,400 do begin
for lam = 0,steps-1 do begin
good = where(ygrid(*) ge ygrid(j))
ytemp = ygrid(good)
ktemp = kgrid(i,good,lam)
if n_elements(ytemp) gt 1. then begin
taugrid(i,j,lam) = int_tabulated(ytemp,ktemp,/double)
; print,taugrid(i,j,lam)

```

```

endif
endfor
endfor
endfor

; Find where taugrid equals 1
ygrid1 = dblarr(201,steps)

for xcol = 0,200 do begin
for lam = 0,steps-1 do begin
tautemp1 = taugrid(xcol,*,lam)
; print,tautemp1(200)
good2 = where(tautemp1 ge 1.)
gmin = min(good2)
if gmin gt -1 then begin
tau2 = taugrid(xcol,good2,lam)
xylam = where(tautemp1 eq min(tau2))
tau1(xcol,lam) = xylam
ygrid1(xcol,lam) = ygrid(xylam)
endif else begin
ygrid1(xcol,lam) = -1.
endelse
endfor
endfor
endfor

```



```

goody0 = where(ygrid1(*,0) ne -1)
goody1 = where(ygrid1(*,1) ne -1)
goody2 = where(ygrid1(*,2) ne -1)
goody3 = where(ygrid1(*,3) ne -1)

;Find location of stagnation point
P = 3.90608
ecc = 0.337
M1 = 23.
M2 = 1.4
shockgeom,enom,phi,time,phase,rsep,R0,RO,oa

;calculates inclination angle
mf = 0.00261      ; mass function
G = 6.673e-11    ; Newtons m^2/kg^2
Msolar = 1.9891e30 ; kilograms
dsec = 86400.    ; length of a day in seconds
Psec = P*dsec   ; Period in seconds
K = 19.74       ; radial velocity in km s^-1

inc = asin(K*1000.*((m1+m2)^2.*Psec/$
(2.*!pi*G*Msolar*m2^3.))^1./3.))
print,'inclination angle (deg) = ',inc*180./!pi

```

```

set_plot,'ps'
device,/landscape,filename='optdepth1.ps'
device,/inches,xsize=8.25,ysize=5.
>window,xsize=400,ysize=400
!x.thick=3
!y.thick=3
!p.thick=3
!p.font=1
!p.charsize=2
!x.style=1
!y.style=1
!x.range=[-30.,30.]
!y.range=[-20.,10.]
!x.title='!8x!3 (R!Dstar!N)'
!y.title='!8y!3 (R!Dstar!N)'
!x.margin=2.
!y.margin=2.

plot,xgrid(goody0)/Rstar,-ygrid1(goody0,0)/Rstar,$
linestyle=4
oplot,-1.*xgrid(goody0)/Rstar,-ygrid1(goody0,0)/Rstar,$
linestyle=4
oplot,xgrid(goody1)/Rstar,-ygrid1(goody1,1)/Rstar,$

```

```

linestyle = 1
oplot,-1.*xgrid(goody1)/Rstar,-ygrid1(goody1,1)/Rstar,$
linestyle = 1
oplot,xgrid(goody2)/Rstar,-ygrid1(goody2,2)/Rstar,$
linestyle = 2
oplot,-1.*xgrid(goody2)/Rstar,-ygrid1(goody2,2)/Rstar,$
linestyle = 2
oplot,xgrid(goody3)/Rstar,-ygrid1(goody3,3)/Rstar,$
linestyle = 3
oplot,-1.*xgrid(goody3)/Rstar,-ygrid1(goody3,3)/Rstar,$
linestyle = 3

oplot,[23.,28.],[-9.5,-9.5],linestyle = 4
xyouts,17.25,-10.,'20cm'
oplot,[23.,28.],[-12.5,-12.5],linestyle = 1
xyouts,17.25,-13.,'13cm'
oplot,[23.,28.],[-15.5,-15.5],linestyle = 2
xyouts,18.25,-16.,'6cm'
oplot,[23.,28.],[-18.5,-18.5],linestyle = 3
xyouts,18.25,-19.,'3cm'

;Overplot orbit of compact object in LS 5039
rsep2 = rsep*100./Rstar
RO2 = RO*Rsun/Rstar

```

```

;Incorporate angle of
omega = 236.
phi2 = phi+omega*!pi/180.

bin = n_elements(rsep2)

rx=dblarr(bin)
ry=dblarr(bin)
ROx=rx
ROy=ry

for i = 0,bin-1 do begin
rx(i) = rsep2(i)*sin(phi2(i))
ry(i) = rsep2(i)*cos(phi2(i))
ROx(i) = RO2(i)*sin(phi2(i))
ROy(i) = RO2(i)*cos(phi2(i))
endfor

oplot,-rx,-ry*sin(inc)
oplot,-ROx,-ROy*sin(inc),linestyle=5

print,max(RO2)

```

```
plot,cos(enom),sin(enom)
polyfill,cos(enom),sin(enom)

;plot arrow pointing towards observer
arrow,-27,-13,-27,-18,/data,/solid,hsize=-.15,thick=4
xyouts,-25,-17,'To observer'

device,/close
set_plot,'x'
cleanplot,/silent

return
end

@/Users/Shared/Programs/Radio/orbsep
@/Users/Shared/Programs/Radio/shockgeom
```

# Bibliography

Abdo, A. A., et al. 2009, *Science*, 326, 1512

Abdo, A. A., et al. 2010, *Astrophysical Journal Supplement Series*, 188, 405

Abt, H. A., 1987, *Physics of Be Stars*, ed. Slettebak, A., & Snow, T. P., (Cambridge: Cambridge Univ. Press), 470

Acciari, V. A., et al. 2009, *Astrophysical Journal*, 698, 94

Aharonian, F., et al. 2005, *Science*, 309, 746

Aharonian, F., et al. 2005, *Astronomy & Astrophysics*, 442, 1

Aharonian, F., et al. 2006, *Astronomy & Astrophysics*, 460, 743

Aharonian, F. A., et al. 2007, *Astronomy & Astrophysics*, 469, L1

Albert, J., et al. 2006, *Science*, 312, 1771

Albert, J., et al. 2007, *Astrophysical Journal*, 665, L51

Aragona, C., McSwain, M. V., Grundstrom, E. D., Marsh, A. N., Roettenbacher, R. M., Hessler, K. M., Boyajian, T. S., & Ray, P. S. 2009, *Astrophysical Journal*, 698, 514

Aragona, C., McSwain, M. V., & DeBecker, M. 2010, *Astrophysical Journal*, 724, 306

- Aragona, C., McSwain, M. V., & Roberts, M. S. E. 2011, *Bulletin of the Liège Royal Scientific Society*, 80, 115
- Bessell, M. S., Castelli, F., & Plez, B. 1998, *Astronomy & Astrophysics*, 333, 321
- Bonatto, C., & Bica, E. 2009, *Monthly Notices of the Royal Astronomical Society*, 394, 2127
- Bongiorno, S. D., Falcone, A. D., Stroh, M., Holder, J., Skilton, J. L., Hinton, J. A., Gehrels, N., & Grube, J. 2011, *Astrophysical Journal*, 737, 11
- Bosch-Ramon, V., Paredes, J. M., Ribó, M., Miller, J. M., Reig, P., & Martí, J. 2005, *Astrophysical Journal*, 628, 388
- Bosch-Ramon, V., et al. 2007, *Astronomy & Astrophysics*, 473, 545
- Cantó, J., Raga, A. C., & Wilkin, F. P. 1996, *Astrophysical Journal*, 496, 723
- Carroll, B. W., & Ostlie, D. A. 2007, *An Introduction to Modern Astrophysics* (San Francisco, CA: Pearson Education, Inc.)
- Casares, J., Ribó, M., Ribas, I., Paredes, J. M., Martí, J., & Herrero, A. 2005, *Monthly Notices of the Royal Astronomical Society*, 364, 899
- Chernyakova, M., Neronov, A., Aharonian, F., Uchiyama, Y., & Takahashi, T. 2009, *Monthly Notices of the Royal Astronomical Society*, 397, 2123
- Coe, M. J. 2000, in ASP Conf. Ser. Vol. 214, *The Be Phenomenon in Early-Type Stars*, ed. Smith, M. A. & Henrichs, H. F., (San Francisco, CA: ASP), 656
- Cohen, M., Wheaton, Wm. A., & Megeath, S. T. 2003, *Astronomical Journal*, 126, 1090

- Cominsky, L., Roberts, M., & Johnston, S. 1994, *Astrophysical Journal*, 427, 978
- Crampton, D. 1968, *Astronomical Journal*, 73, 338
- Droege, T. F., Richmond, M. W., & Sallman, M. 2007, *Publications of the Astronomical Society of the Pacific*, 119, 1083
- Dubus, G. 2006, *Astronomy & Astrophysics*, 456, 801
- Durant, M., Kargalstev, O., Pavlov, G. G., Chang, C., & Garmire, G. P. 2011, *Astrophysical Journal*, 735, 58
- Egan, M. P., et al. 2003, *The Midcourse Space Experiment Point Source Catalog Version 2.3*
- Ekström, S., Meynet, G., Maeder, A., & Barblan, F. 2008, *Astronomy & Astrophysics*, 478, 467
- Falcone, A. D., Grube, J., Hinton, J., Holder, J., Maier, G., Mukherjee, R., Skilton, J., & Stroh, M. 2010, *Astrophysical Journal*, 708, L52
- Fitzpatrick, E. 1999, *Publications of the Astronomical Society of the Pacific*, 111, 63
- Friedemann C. 1992, *CDS Inf. Bull.*, 40, 31
- Garmany, C. D., Conti, P. S., & Massey, P. 1980, *Astrophysical Journal*, 242, 1063
- Gooch, R.E. 1996, *Astronomical Data Analysis Software and Systems V*, ASP Conf. Series Vol. 101, ed. Jacoby, G. H. J., & Barnes, J., 80
- Gray, D. F. 2005, *The Observation and Analysis of Stellar Photospheres* (New York, Cambridge University Press)



- Grundstrom, E. D., & Gies, D. R., 2006, *Astrophysical Journal*, 651, L53
- Gutiérrez-Soto, J., Fabregat, J., Suso, J., Lanzara, M., Garrido, R., Hubert, A.-M., & Floquet, M. 2007, *Astronomy & Astrophysics*, 476, 927
- Hinton, J. A., et al. 2009, *Astrophysical Journal Letters*, 690, L101
- Krelowski, J. & Papaj, J. 1993, *Publications of the Astronomical Society of the Pacific*, 105, 1209
- Lamers, H. J. G. L. M., & Cassinelli, J. P. 1999, *Introduction to Stellar Winds* (New York, NY: Cambridge University Press)
- Lamers, H. J. G. L. M., & Leitherer, C. 1993, *Astrophysical Journal*, 412, 771
- Lanz, T., & Hubeny, I. 2003, *Astrophysical Journal Supplement Series*, 146, 417
- Lanz, T., & Hubeny, I. 2007, *Astrophysical Journal Supplement Series*, 169, 83
- Liu, Q. Z., van Paradijs, J., & van den Heuvel, E. P. J., 2006, *Astronomy & Astrophysics*, 455, 1165
- McSwain, M. V., Gies, D. R., Riddle, R. L., Wang, Z., & Wingert, D. W. 2001, *Astrophysical Journal Letters*, 558, L43
- McSwain, M. V., Gies, D. R., Huang, W., Wiita, P. J., Wingert, D. W., & Kaper, L. 2004, *Astrophysical Journal*, 600, 927
- McSwain, M. V., & Gies, D. R., 2005, *Astrophysical Journal Supplement Series*, 161, 118
- McSwain, M. V., Huang, W., Gies, D. R., Grundstrom, E. D., & Townsend, R. H. D. 2008, *ApJ*, 672, 590

- McSwain, M. V., Ray, P. S., Ransom, S. M., Roberts, M. S. E., Dougherty, S. M., & Pooley, G. G. 2011, *Astrophysical Journal*, in press (arXiv/1106.5550)
- Melia, F. 2009, *High-Energy Astrophysics* (Princeton, NJ: Princeton University Press)
- Moldón, J. Johnston, S., Ribó, M., Paredes, J. M., & Deller, A. T. 2011, *Astrophysical Journal*, 732, L10
- Morbey, C. L., & Brosterhus, E. B. 1974, *Publications of the Astronomical Society of the Pacific*, 86, 455
- Morgan, W. W., Code, A. D., & Whitford, A. E. 1955, *Astrophysical Journal Supplement Series*, 2, 41
- Neckel, T., & Chini, R. 1980, *Astronomy & Astrophysics Supplement*, 39, 411
- Negueruela, I., Ribó, M., Herrero, A., Lorenzo, J., Khangulyan, D., & Aharonian, F. A. 2011, *Astrophysical Journal*, 732, L11
- Ogura, K., & Ishida, K. 1981, *Publications of the Astronomical Society of Japan*, 33, 149
- Paredes, J. M., Martí, J., Ribó, M., & Massi, M. 2000, *Science*, 288, 2340
- Paredes, J. M., Ribó, M., Ros, E., Martí, J., & Massi, M. 2002, *A&A*, 393, L99
- Park, B., & Sung, H. 2002, *Astronomical Journal*, 123, 892
- Parkin, E. R., & Pittard, J. M. 2008, *Monthly Notices of the Royal Astronomical Society*, 388, 1047
- Pérez, M. R., Thé, P. S., & Westerlund, B. E. 1987, *Publications of the Astronomical Society of the Pacific*, 99, 1050

- Porter, J. M., & Rivinius, T. 2003, *Publications of the Astronomical Society of the Pacific*, 115, 1153
- Puls, J., et al. 1996, *Astronomy & Astrophysics*, 305, 171
- Ribó, M., Paredes, J. M., & Martí, J. 1999, *New Astronomy Reviews*, 43, 545
- Ribó, M., Paredes, J. M., Romero, G. E., Benaglia, P., Martí, J., Fors, O., & García-Sánchez, J. 2002, *Astronomy & Astrophysics*, 384, 954
- Roberts, D. H., Lehár, J., & Dreher, J. W. 1987, *Astronomical Journal*, 93, 968
- Rosswog, S., & Brüggen, M. 2007, *Introduction to High Energy Astrophysics* (Cambridge, UK: Cambridge University Press)
- Sarty, G. E., et al. 2011, *Monthly Notices of the Royal Astronomical Society*, 411, 1293
- Schaller, G., Schaerer, D., Meynet, G., & Maeder, A. 1992, *Astronomy & Astrophysics Supplement*, 96, 269
- Skilton, J. L., et al. 2009, *Monthly Notices of the Royal Astronomical Society*, 399, 317
- Skrutskie, M. F., et al. 2006, *Astronomical Journal*, 131, 1163
- Takahashi, T., et al. 2009, *Astrophysical Journal*, 697, 592
- Takata, J., & Taam, R. E. 2009, *Astrophysical Journal*, 702, 100
- Townsend, R. H. D., Owocki, S. P., & Howarth, I. D. 2004, *Monthly Notices of the Royal Astronomical Society*, 350, 189
- Turner, D. G. 1976, *Astrophysical Journal*, 210, 65

- Voroshilov, V. I., Guseva, N. G., Kalandadze, N. B., Kolesnik, L. N., Kuznetsov, V. I., Metreveli, M. D., & Shapovalov, A. N. 1985, Catalogue of BV magnitudes and spectral classes for 6000 stars (Kiev, Ukraine: Ukrainian Acad. Nauk)
- Walecka, J. D. 2007, *Introduction to General Relativity* (Singapore: World Scientific Publishing Co. Pte. Ltd.)
- Wesselius, P. R., van Duinen, R. J., de Jonge, A. R. W., Aalders, J. W. G., Luinge, W., & Wildeman, K. J. 1982, *Astronomy & Astrophysics Supplement*, 49, 427

# Vita

Christina Aragona was born on July 12, 1983 to David and Antonetta Aragona and is the oldest of two children. She studied at Drew University from September 2001 to May 2005 and graduated summa cum laude with a B.A. in physics and music. She began studying at Lehigh University in August 2006 and earned an M.S. in physics in May 2008. During her first two years at Lehigh, Christina was supported by a Lehigh University Deans Fellowship and a GAANN Fellowship. She started working with Dr. M. Virginia McSwain in the fall of 2007. After spending four years studying  $\gamma$ -ray binaries and Be stars under Dr. McSwain's direction, Christina received her Ph.D. in Physics in September 2011.

## REFEREED PUBLICATIONS

- Aragona, C., McSwain, M. V., Roberts, M. S. E., *The Stellar Wind of LS 5039*, Bulletin of the Liège Royal Scientific Society, 2011, 80, 115-119
- Aragona, C., McSwain, M. V., DeBecker, M., *HD 259440: The Proposed Optical Counterpart of the  $\gamma$ -ray Binary HESS J0632+057*, ApJ, 2010, 725, 306-312
- Aragona, C., McSwain, M. V., Grundstrom, E. D., Marsh, A. N., Roettenbacher, R. M., Hessler, K. M., Boyajian, T. S., Ray, P. S., *The Orbits of the  $\gamma$ -ray Binaries LS I +61 303 and LS 5039*, ApJ, 2009, 698, 514-518